Investigation of Interface, Defects, and Growth of GaSb/Si Heteroepitaxial Films using Aberration-Corrected Scanning Transmission Electron Microscopy

By

Shahrzad Hosseini Vajargah, M. A. Sc.

A Thesis

Submitted to the School of Graduate Studies

in Partial Fulfillment of the Requirements

for the Degree of

Doctor of Philosophy

McMaster University

Doctor of Philosophy (2013) McMaster University
(Department of Materials Science and Engineering) Hamilton, Ontario

TITLE:	Investigation of Interface, Defects, and Growth of GaSb/Si Heteroepitaxial Films using Aberration-corrected Scanning Transmission Electron Microscopy
AUTHOR:	Shahrzad Hosseini Vajargah, M. A. Sc. (Sharif University of Technology)
SUPERVISOR:	Professor Gianluigi A. Botton
NUMBER OF PAGES:	xxvi, 152

TO THREE ADMIRABLE INSPIRATIONS OF MY LIFE:

MAMAN,

BABA, AND

MOHAMMAD REZA

Abstract

Heteroepitaxial films of group III-antimonide-based semiconductor compounds on Si are amongst the most appealing candidates for solar applications because of the well-established Si platform and also for offering band-gap energies beyond the silicon road map. Nonetheless, high lattice mismatch between GaSb and Si as well as ambiguous nucleation of GaSb on Si are major drawbacks in manufacturing of heteroepitaxial GaSb/Si films because they can generate various defects in films. Atomic-level detection of these defects and delving into their origin, orientation, distribution, propagation, and interaction with each other will therefore provide an insight into inhibiting their formation or reducing their severity. State-of-the-art aberration-corrected transmission electron microscopes have marked a new era in the investigation of interfaces and defects. With sub-angstrom electron probes in scanning transmission electron microscopes, it is possible to pinpoint the individual atomic columns at interfaces and defects.

In this thesis, GaSb epilayers grown with molecular beam epitaxy on Si substrates were studied through aberration-corrected scanning transmission electron microscopy. The strain-relief mechanism of the epitaxial GaSb through formation of interfacial misfit dislocations was investigated and the strain distribution in the vicinity of dislocation cores as well as epitaxial layer was analyzed. The specific atomic-number dependent contrast mechanism of the high-angle annular dark-field technique enabled the unprecedented direct observation of anti-phase boundaries, the extended defects of highest interest in polar-on-nonpolar growths. This observation unraveled the ambiguity of nucleation of GaSb at interface regardless of preferential deposition of atomic species during growth procedure. The growth of GaSb at the initial stage of deposition was

further investigated to understand the role of an AlSb buffer layer and growth mechanism of GaSb precisely. This investigation showed that AlSb and GaSb epilayers occur by Volmer-Weber growth mode and AlSb islands provide energetically favorable nucleation sites for GaSb film. Furthermore, taking advantage of atomic-resolution detection capability of high-angle annular dark-field in scanning transmission electron microscopy a novel mechanism of strain relief through multiple twining resulting in a lattice-registered growth of GaSb on Si(211) was elucidated. This contribution demonstrates that aberration-corrected scanning transmission electron microscopy provides profound insight into the polar-on-nonpolar growth which can be exploited to suppress the formation of structural defects.

Acknowledgment

I would like to thank several individuals who contribute to this episode of my life in many ways.

I would like to express my sincere gratitude to my supervisor Dr. Gianluigi A. Botton from whom I learned not just doing good research but being a considerate mentor. I am very grateful for his insightful advice, invaluable time and patience throughout my PhD period. I am also appreciative to my supervisory committee members, Dr. John S. Preston and Dr. Jeffery J. Hoyt for their thoughtful comments and valuable feedbacks.

During the course of PhD, I was honored to work with one of world's leading microscope in Canadian Centre of Electron Microscopy but I barely can forget my first mentor, Mr. Fred Pearson, from whom I learned the alphabets of electron microscopy on an old and fairly elementary machine. I am deeply thankful to Mr. Andy Duft for bearing my complaints on various tools in sample preparation lab and helping me in any kind of instrumental problems. I am genuinely grateful to Dr. Martin Couillard for showing practical tips on sample preparation and Dr. Sorin Lazar for teaching me operational tips on alignment of microscope. Thanks to Dr. Yang Shao and Kai Cui for helping me with simulation and strain analysis problems. I am also thankful to administrative staff of department of Materials Science and Engineering, Diana Maltese, Elvira Evangelista, Nancy Cole and Jane Mah for providing the friendly environment in the department.

I have been fortunate enough to meet quite a diverse and talented group of knowledgeable minds in McMaster University. I would like to thank Dr. Rafel N. Kleiman for his innovative ideas and Dr. Brad Robinson and Dr. Shahram

Ghanad-Tavakoli for providing me with valuable semiconductor samples. Thanks to Steffi Woo for helping me with my crystallography questions.

Special thanks go to my group members for their encouragements through difficult moments of PhD. I owe thanks to my gracious and compassionate friends, Shirin Kaboli, Nooshin Tajik, and Shahrzad Hadian for supporting through difficult moments of life. Faranak Aghdasi for being the closest thing I have to a sister, for just always understanding.

My sincere gratitude goes to my father, Ali Hosseini, and my mother Gohar Fatehpour, for their everlasting love and support throughout my life and for being who I am. Thanks to my brothers, Nima and Pouya who have always been there for me at all the important periods of my life. I am also deeply grateful to my grandmother, Maman-Bozorg, who despite of not having the opportunity to get educated was always encouraging me to pursue my education to the highest level. Dear Maman-Bozorg, I still miss you and I wish you rest in peace.

I owe earnest thanks to my love of life and my husband, Mohammad Reza Moazezi whose presence has made my life more meaningful and joyful. His heartfelt love and support have been always with me during tears and laughter. Dear Mohammad Reza, your invaluable unselfish love means a lot to me and I am grateful to you.

During these years of being far from home, Skype and Yahoo Messenger have shortened the distance between me and my lovely family and friends and I wish to thank them.

And eventually I am grateful to God for giving me the chance to flourish my talents in a world where not everybody has this chance, for placing these people in my life and for giving the honor to experience the love.

List of Publications

This thesis is based on following publications:

Chapter 4

- **S. Hosseini Vajargah**, M. Couillard, K. Cui, S. Ghanad-Tavakoli, B. Robinson, R. N. Kleiman, J. S. Preston, and G. A. Botton, *"Strain relief and AlSb buffer layer morphology in GaSb heteroepitaxial films grown on Si as revealed by high-angle annular dark-field scanning transmission electron microscopy"*, Appl. Phys. Lett. **98**, 082113 (2011), doi: 10.1063/1.3551626.

Chapter 5

- **S. Hosseini Vajargah**, S. Y. Woo, S. Ghanad-Tavakoli, R. N. Kleiman, J. S. Preston, and G. A. Botton, *"Atomic-resolution study of polarity reversal by scanning transmission electron microscopy in GaSb grown on Si"*, J. Appl. Phys. **112**, 093101 (2012), doi: 10.1063/1.4759160.

- S. Y. Woo, **S. Hosseini Vajargah**, S. Ghanad-Tavakoli, R. N. Kleiman, J. S. Preston, and G. A. Botton, *"Direct observation of anti-phase boundaries in heteroepitaxy of GaSb thin films grown on Si(001) by transmission electron microscopy"*, J. Appl. Phys. **112** (2012), doi: 10.1063/1.4756957.

Chapter 6

- **S. Hosseini Vajargah**, M. Couillard, K. Cui, S. Ghanad-Tavakoli, B. Robinson, R. N. Kleiman, J. S. Preston, and G. A. Botton, *"Strain relief and AlSb buffer layer morphology in GaSb heteroepitaxial films grown on Si as revealed by high-angle annular dark-field scanning transmission electron microscopy"*, Appl. Phys. Lett. **98**, 082113 (2011), doi:10.1063/1.3551626.

Contents

List of Figures

List of Tables

List of Abbreviation

2DXRD	Two-Dimensional X-ray Diffraction
ABF	Annular Bright-field
ADF	Annular Dark Field
AFM	Atomic Force Microscopy
APB	Anti-phase Boundary
APD	Anti-phase Domains
BF	Bright Field
CBED	Convergent-beam Electron Diffraction
C_C	Chromatic aberration Coefficient
CCEM	Canadian Centre for Electron Microscopy
C_S	Spherical Aberration Coefficient
DF	Dark Field
DFT	Density Functional Theory
DI	Di-ionized
DCXRD	Double Crystal X-ray Diffarction
EDXS	Energy Dispersive X-ray Spectrometry
EELS	Electron Energy-loss Spectrometry
FFT	Fast Fourier Transform
FOLZ	First Order Laue Zone

FT	Fourier transform
FWHM	Full Width at Half Maximum
GPA	Geometric Phase Analysis
HAADF	High-angle Annular Dark-field
HRTEM	High Resolution Transmission Electron Microscopy
IMF	Interfacial Misfit
LAADF	Low-angle Annular Dark-field
MBE	Molecular Beam Epitaxy
ML	Monolayer
QD	Quantum Dot
QW	Quantum Well
RHEED	Reflection High-energy Electron Diffraction
SAED	Selected Area Electron Diffraction
SLS	Strained-layer Superlattice
SK	Stranski-Krastanov
STEM	Scanning Transmission Electron Microscopy
TDS	Thermal Diffuse Scattering
TEM	Transmission Electron Microscopy
TPV	Thermophotovoltaic
VW	Volmer-Weber
WL	Wetting Layer

XFEG	high brightness Field-emission Gun

Chapter One

Introduction

Increasing world consumption of energy, shortage of fossil fuel resources, and global warming have drawn world-wide attention to finding better alternatives for sustainable development. Hence, renewable energy sources have received a great deal of attention in recent years. Solar radiation, as one of the everlasting energy sources, has played a pivotal role in this movement. In order for solar energy to become an economically viable energy resource, solar energy convertors need to have high efficiencies to be able to generate more electricity from incident sunlight. First generation and commercially available solar cells are based on single junction silicon with efficiencies between 31% and 41%. Photons with energies below the band-gap of Si and excess energy of photons with energies above the Si band-gap are lost in these solar cells (Figure 1.1). Second generations of solar cells which are based on the thin film designs suffer from non-radiative losses due to low quality of films. Multi-junction cells, the third generation solar cells, are thin film stacks of band-gap tuned compounds on an appropriate substrate. Efficiencies as high as 40% are achieved in these solar cells

as the solar spectrum is absorbed by a semiconductor with a specific band-gap based on the wavelength. In other words, high energy photons are absorbed by higher band-gap junction while lower band-gap junction absorbs the lower energy photons. For instance, AlInGaP (1.9 eV) / GaAs (1.4 eV) / Ge (0.66 eV) triple junction can reach efficiency of 41.1% under AM1.5G[1], 1 sun by separating the absorption of solar spectrum [1].

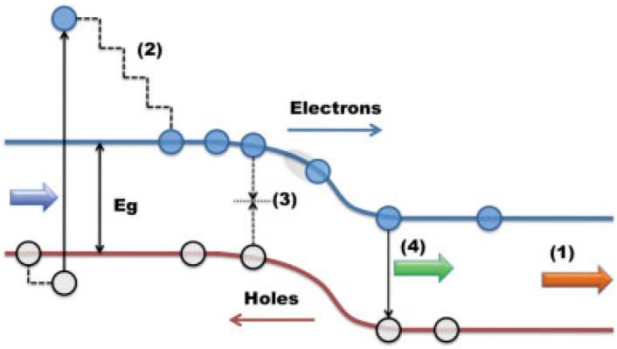

Figure 00.1: Origin of most efficiency losses (1) photons with energy below bandgap (Red loss) (2) photons with energy above the bandgap (Blue loss) (3) non-radiative recombination due to defects (4) radiative recombination, the generated photon can be reabsorbed [2].

The plot in Figure 1.2 displays the lattice constant of various elemental and compound semiconductors as a function of their band-gap energies. As it is seen, III-V compounds semiconductors, in particular, have a wide range of bandgap energies which allows them to emit and absorb a broad spectrum of photon energies. This makes them suitable for various applications beyond the Si-roadmap from light-emitting diodes and microwave circuits to high power transistors and solar cells. The growth of such materials on Si substrates opens new possibilities for low-cost photovoltaic applications where the absorption

[1] The standard spectrum at earth's surface which equals to 1kW/m^2. Air mass is the path length of light through atmosphere normalized to the shortest possible path.

spectrum can be tuned by engineering new compounds with specific band gap energies. This would make it possible to create new generations of multi-junction cells where a much greater portion of the solar spectrum can be harvested while the manufacturing costs can be significantly reduced. Moreover, using Si as a substrate has the advantages of the capability to produce large area Si substrates with low cost and less complexity and also large scale integration of compound semiconductors in the electronics industry. There are, however, significant challenges related to the hetero-epitaxial growth of these compounds that need to be addressed in order to develop such devices.

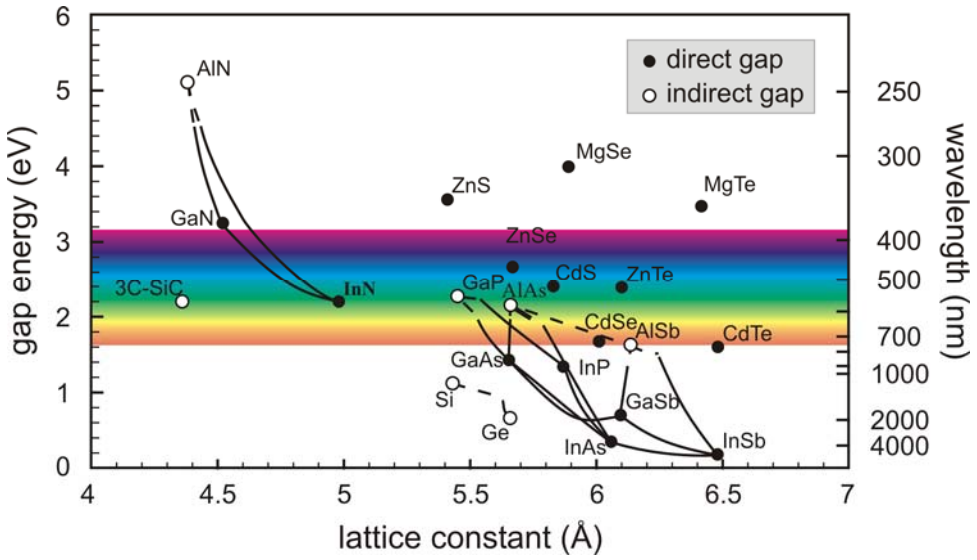

Figure 0.2: The plot of lattice constant of elemental and compound semiconductors vs. their band-gap energies [3].

Recently, group III-Sb-based semiconductor compounds have attracted significant attention for a variety of applications such as laser diodes, high-speed electronic devices, high electron mobility transistors, and photovoltaics [4]. Their band-gap energy covers a broad range of energies from a narrow 0.17 eV for

InSb, and 0.726 for GaSb, to 1.58 eV for AlSb. Therefore, they are recognized as a superior choice for new-emerging thermo-photovoltaic application [5]. The III-Sb based compound family is also one of the highly lattice-mismatched binary III-Vs with Si. This huge mismatch results in formation of strain relief defects such as misfit dislocations and deformation twins. All III-Sb based compounds do crystallize in the zinc-blende (also known as sphalerite) structure. The symmetry difference between zinc-blende and diamond structure of Si gives rise to a class of electronically active extended defects known as anti-phase boundaries (APBs). As a result, the quality of the device is highly dependent on type and density of these defects.

Indeed, characterization of the strain-induced and growth defects and understanding of their origins plays a vital role in development of III-Sb based/Si heterostructures. Transmission electron microscopy techniques are amongst the common characterization tools which have the advantage of direct visualization of defects. The presence of the misfit dislocations at the interface of GaSb and Si as well as APBs has previously been explored by conventional and high resolution transmission electron microscopy (HRTEM) images based on phase contrast techniques. [6-8]. This approach is very sensitive to local variation of the sample orientation, thickness, and the defocus condition, so that qualitative interpretation and the determination of the local lattice parameter from such images are not straightforward even in aberration-corrected transmission electron microscopy (TEM) images [9]. However, direct interpretation of image contrast and spectroscopic analysis capabilities in high-angle annular dark-field scanning transmission electron microscopy (HAADF-STEM) [10] along with novel progresses in correcting the lens aberrations have shown a new potential in investigating the atomic structures at interfaces and defects. The contrast mechanism exploited in HAADF-STEM strongly depends on the atomic number

of the scattering atoms [11]. Hence, HAADF imaging can unambiguously elucidate the precise configuration of defects and their origins much better than conventional phase contrast imaging.

Scanning transmission electron microscopes (STEMs) equipped with spherical aberration correctors have played a prominent role in pinpointing the atomic configuration of interfaces and defects. The use of atomic resolution HAADF-STEM [12] in a spherical aberration-corrected electron microscope capable of forming sub Angstrom electron probes offers important advantages in characterizing such lattice mismatched III-V semiconductor heterostructures. The contrast observed in the images can be intuitively interpreted based on the incoherent scattering of electrons at high-angle, even across interfaces since the image contrast depends on neither defocus of the objective lens nor the thickness of the foil. The interface location can therefore be clearly identified because there is a strong contrast associated with the atomic number of the atomic columns from the Si substrate and the GaSb film following a $Z^{1.7}$ dependence of the scattered intensity on the HAADF detector [11].

Although the HAADF images provide the necessary strong contrast, such images have not been previously used to extract quantitative information on the local atomic displacements across interfaces using the geometric phase analysis (GPA) method. The GPA method [13-16] and its variants [17] are well established for strain mapping of semiconductor thin films, and earlier work has taken advantage of the highly reproducible and nearly distortion-free HRTEM micrographs following correction through deconvolution. In these conditions, reliable GPA results are based on precise measurement of the location of the atomic columns within the films. However, in a dedicated environment that is sufficiently stable with respect to mechanical vibration, electromagnetic fields, and thermal fluctuations, the GPA can be applied, in principle, to HAADF-STEM

images. Because deconvolution is not necessary, HAADF-STEM images accompanied by strain measurements with GPA [18] can provide a profound and elegant understanding of interface properties of semiconductors.

Accordingly, the objective of this research is a detailed investigation and understanding of the atomic configuration of interfaces and defects, the origin, distribution and propagation of the extended defects, all this using aberration-corrected transmission electron microscopy techniques. In order to eliminate any possible ambiguities regarding the structure of the defects and interfaces in HAADF-STEM, corresponding simulations based on multislice approach were carried out. Additionally, lattice displacements and strain distribution in HAADF-STEM image of defects and interfaces were studied by GPA.

This thesis comprises of eight chapters. Chapter Two provides a literature review, consisting of an introduction to group III-V semiconductors and the Si substrate crystal structure, strain and growth defects followed by growth modes, the use of AlSb buffer layer, transmission electron microscopy techniques used for identifying the defects as well as suggested solutions to minimize their occurrence. Chapter Three provides the experimental and simulation procedures, including sample preparation methods, transmission electron microscopy technique and simulation approaches. Chapter Four describes the structure and quality of GaSb films grown on nominal Si(001) substrate. Chapter Five includes the identification of the most electrically deleterious defect of APBs and strain distribution in their proximity. Chapter Six provides the growth mechanism of APB-free GaSb on Si(211) as a solution to overcome sub-lattice reversal issue. Chapter Seven presents an experimental study on the growth mode of GaSb films and the effect of AlSb buffer on the morphology of GaSb films. Chapter Eight presents a summary of concluding remarks of the research and suggestions for future works.

Chapter Two

Literature Review

Heteroepitaxial III-V compound semiconductor layers grown on silicon have the potential to provide a range of new optoelectronic properties that make distinct applications beyond the Si-roadmap possible. Moreover, using Si as a substrate has the advantages of not only lower cost and less complexity but also large scale integration of compound semiconductors in the electronics industry. The lattice mismatch between Si and the heteroepitaxial layers as well as the formation of anti-phase domains are two major obstacles that have to be overcome in order to grow device quality films. The III-Sb based compound family is one of the highly lattice-mismatched binary III-Vs with Si. Indeed a major determinant of film quality is expected to be the detailed strain relief mechanisms especially the type and Burgers vector of the preferred interfacial misfit (IMF) dislocations and their effectiveness in accommodating strain. Additionally, anti-phase domains (APDs), i.e. domains separated by anti-phase boundaries (APBs), are an inherent hindrance to the growth of a polar film on a non-polar substrate. The characterization of APBs is therefore not only important

to understanding the origins of the defect formation but is also relevant since APBs are electrically active defects. In the present chapter, a literature review including the crystal structure of GaSb and Si as a substrate, strain and growth defects, characterization methods used for studying these defects as well as growth modes of III-Sb based films are summarized.

2.1 Group III-Antimonide-based Semiconductors

III-Sb based compound semiconductors cover a wide range of band-gap energies with different types from narrow band of 0.165 eV (direct) for InSb and 0.762 eV (direct) for GaSb to the wide band-gap of 1.58 eV (indirect) for AlSb. Having the lattice parameter ranging from 6.095Å for GaSb, 6.135 Å for AlSb, to 6.479 Å for InSb, they are amongst the highly-lattice mismatched binary III-Vs with Si (a=5.431Å). Group III-Sb compounds do crystallize in the zinc-blende structure which is very similar to the diamond structure of the elemental semiconductors Si and Ge. Both diamond and zinc-blende structures are made up of two interpenetrating face-centred (fcc) sublattices. One sublattice is positioned at 0,0,0 lattice sites and the other is displaced by a quarter of the body diagonal. In the diamond structure, both sublattices are occupied by same atoms (Figure 2.1(a)) while in zinc-blende (also known as spharelite) structure they are occupied by exclusively group III or V elements (Figure 2.1(b)). The zinc-blende structure therefore is non-centrosymmetric (lack of inversion centre) i.e. neither [x,y,z] and [-x,-y,-z] directions nor (x,y,z) and (-x,-y,-z) planes are equivalent. Hence, the bonds are polar.

There is a significant attention to Sb-based semiconductor compounds due to their wide range of band-gap energy, band-gap offsets and electronic barriers along with extremely high electron mobility which make them a good choice for

low-power consumption and high-speed electronic devices. Therefore, recent research has been focused on developing binary antimonide-based semiconductor compounds AlSb, GaSb and InSb and their mixed alloys for various applications including high-speed analog and digital systems used for data processing, communications, imaging, and sensing in portable devices and satellites. Sb-based compound semiconductors have the advantage over other III-V compounds due to narrow band-gap properties and high carrier mobility, which has made them attractive for high performance optical devices.

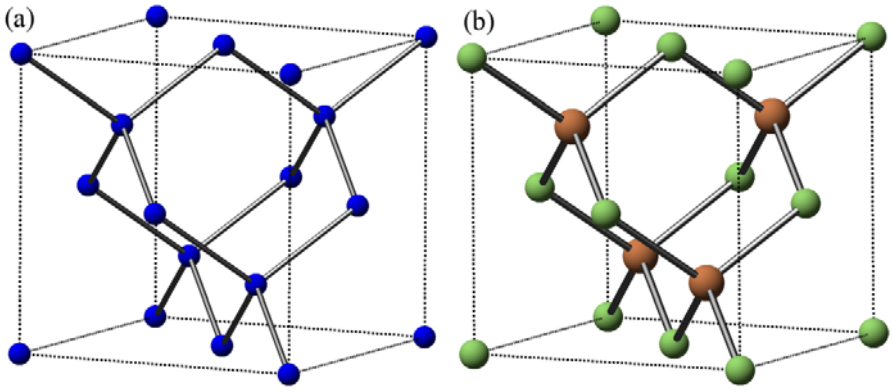

Figure 00.1: Unit cell of (a) diamond structure Si, and (b) zinc-blende structure III-V compound semiconductor.

The small band-gap energy of GaSb prevents it from being an ideal single-junction solar cell [5]. Therefore, using GaSb for solar cell application was postponed until first attempt to increase the efficiencies using multi-junction cells. GaSb plays a key role in the development of high performance devices, since the lattice parameter of GaSb matches the one of different ternary and quaternary III-V compound materials with band-gap range between 0.17 of InSb to 1.58 of AlSb and therefore it can be used as a substrate. Various applications of GaSb based structures include laser diodes with low threshold voltage, photodetectors with

high quantum efficiency, high frequency devices, superlattice with tailored optical and transport characteristics, and booster cells in tandem solar cell arrangement for improved efficiency of photovoltaic cells. GaSb also exhibits a direct band-gap and therefore is also a good candidate for high efficiency thermophotovoltaic (TPV) applications. This material can convert infrared radiation to electricity and is proposed as the best substrate for ternary and quaternary compounds [5, 6, 19-22].

2.2 Si Substrate

Using Si substrates for growing compound semiconductors has significant advantages, such as the low cost, high quality of the wafer supply and the numerous benefits of using a well-established manufacturing platform. Besides, studying the epitaxial growth of Sb-based compounds on Si enhances the knowledge about the fundamental of polar-on-nonpolar growth.

The Si (001) surface is one of the commonly used Si substrates for heteroepitaxy of III-V compounds. Atomic-high surface steps are inherent characteristic of Si (001) surface. Surface steps can be odd or even number of atomic layer height or simply single or double steps. They are also classified based on the direction of the step edge with respect to direction of dimerization of dangling bonds. Figure 2.2 displays four different Si (001) surfaces in which surface terraces are separated by step edges: single step with step edge perpendicular (S_A) and parallel (S_B) to the dimerization direction, and double step with step edge perpendicular (D_A) and parallel (D_B) to the dimerization direction. S_A is one of the most common types of the steps on Si (001) surface due to the lower formation energy [23] and no extra dangling bonds and strain associated to its rebonding at step edges [24]. On a flat Si (001), steps alternately raise or lower

the terrace height; while in a vicinal Si (001) S_A and S_B alternate each other [24]. Based on theoretical calculation D_B is more energetically favorable compared to S_A and S_B [23] and it is experimentally shown that upon proper heat treatment processes the step doubling happens due to the surface reconstruction [25].

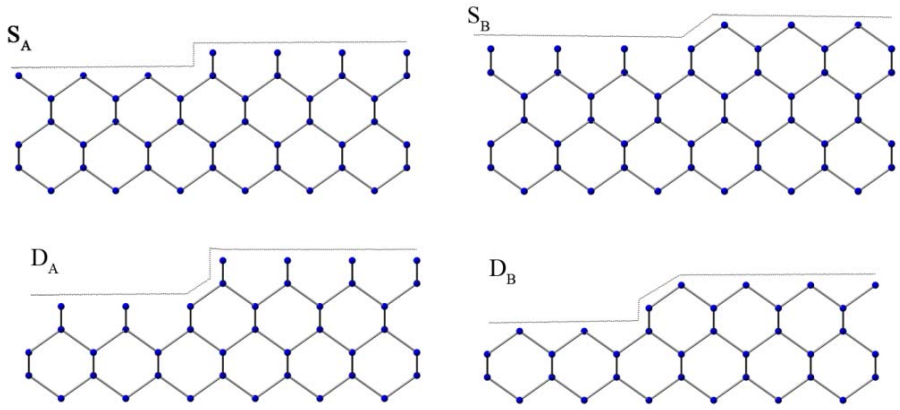

Figure 0.2: The four different step configuration of Si (001) substrates in side view.

Other surface orientations of Si substrates such as Si (211), even though less studied, are important for epitaxy of III-V compounds. Si (211) is an inherently stepped surface with (111)-oriented step terraces and (001)-oriented step edges (Figure 2.3(a)). The bulk-truncated Si (211) surface shown in Figure 2.3(b) indicates that Si atoms have two dangling bonds for each step edge; however, there is only one dangling bond for each Si terrace atom. This distinguishing characteristic of the surface atoms provides two distinct bonding sites for overlying atomic species. Moreover, the planes parallel to the interface contain equal number of cation and anion atoms which assures a charge-free interface (Figure 2.3(c)). Although Si (211) is not a common substrate for the growth of compound semiconductor systems, it has been of particular interest for

studying the surface reconstruction [26, 27], electronic structure [28] and surface energy [29]. Taking advantage of the periodic array of steps, Si (211) has been used as a template for self-assembly of Ga [30, 31], Al [31], and In [32] nanowires. In addition, surface reconstruction of Si (211) by Sb [33], As [34, 35], and Te [35] deposition has been investigated in order to understand their roles in surface modification of Si for later epitaxial growth.

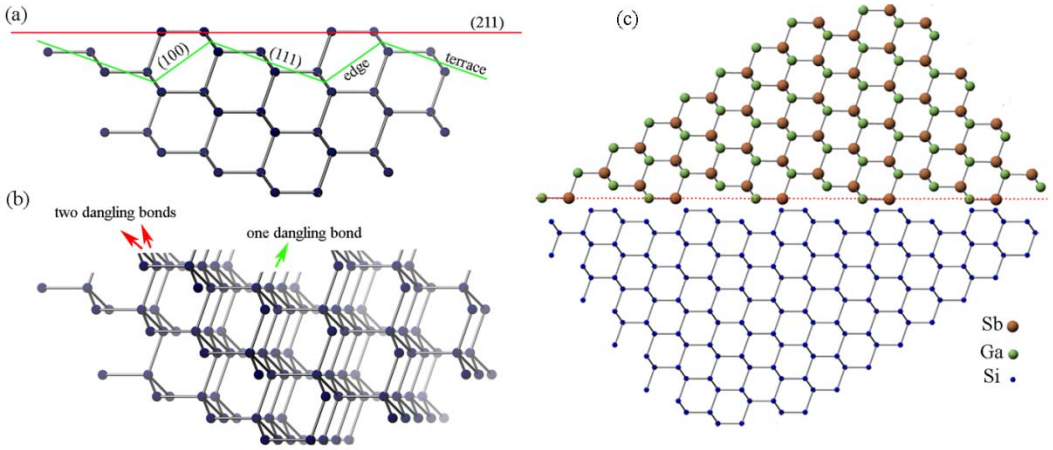

Figure 0.3: (a) The ball and stick model of Si (211) surface (red line) with step terrace and edges (green line), (b) the terrace and edge Si atoms with one and two dangling bonds, respectively, and (c) plane parallel to the interface of GaSb/Si(211) highlighted by red dotted line contains equal numbers of Ga and Sb atoms.

2.3 Structural Defects in Epitaxial III-V Compounds

The lattice mismatch between Si and the heteroepitaxial layers as well as the formation of anti-phase domains are two major challenges in growing the polar III-V compound epilayers on non-polar Si. The mismatch between the thermal expansion coefficients of GaSb ($\alpha = 7.75\times10^{-6}$ K^{-1}) and Si ($\alpha = 2.59\times10^{-6}$

K^{-1}) is a significant contributing factor at high growth temperatures. The lattice mismatch of 12.2% classifies the GaSb/Si growth as a high lattice mismatch heteroepitaxy. These two obstacles give rise to various types of defects including strain relief and growth defects. The high mismatch of lattice parameters and thermal expansion coefficients induce a huge amount of strain that needs to be relieved. Interfacial misfit dislocations, threading dislocations, deformation twins are the main strain relief defects. Even in absence of strain, anti-phase boundaries and growth twins can still form.

2.3.1 Interfacial Misfit Dislocations and Threading Dislocations

Frank and van der Merwe [36-38] modeled the substrate and film in order to investigate the strain relief mechanism in epitaxial films. They showed that below the critical thickness the misfit between film and substrate is accommodated by elastic deformation, while above the critical thickness it becomes energetically favorable in the film to relax the strain by forming interfacial misfit dislocations. Therefore, misfit dislocations are essential for the growth of lattice-mismatch films. The misfit accommodated by a dislocation depends on projection of its Burgers vector to the interface plane. There are mainly two types of misfit dislocations type I and II. Type I dislocations have their Burgers vector lying parallel to the interface and are therefore the most efficient types of interfacial misfit dislocations. There are two sets of extra {111} half planes associated with these pure edge dislocations. Type I dislocations are also called Lomer dislocations, perfect dislocations, or complete edge dislocation. Type II dislocations are characterized by only one additional half plane. The Burgers vector of type II dislocations are at an angle of 60° to the dislocation line and lie at an angle of 45° with the interface. Consequently, they are not so effective in releasing the strain [24, 39, 40]. Two 60° partial dislocations with

complementary Burgers vector (parallel with opposite signs) can react with each other and from a complete edge dislocation [41].

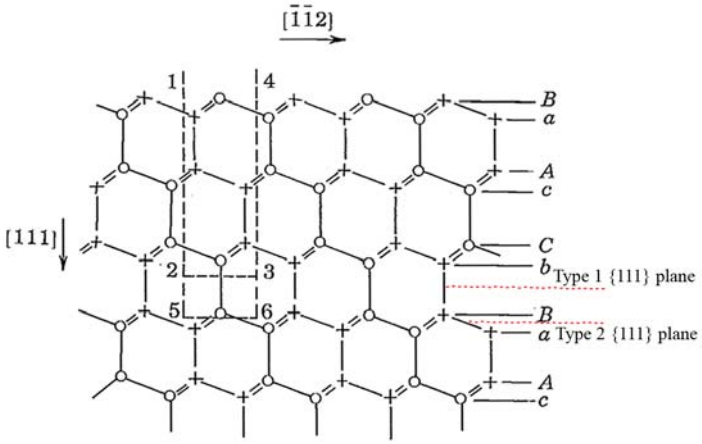

Figure 00.4: The (1-10) projection of diamond structure. The symbols o and + represent the atoms in and below the plane of diagram, respectively. Dislocation resulting from removing the 1-5-6-4 slab is glide type, and the removal of 1-2-3-4 slab leads to shuffle type dislocation [43].

Hornstra [42] originally proposed the core structure model for symmetrical Lomer dislocations. Depending on which set of atomic planes is omitted (Figure 2.4) [43], Lomer dislocations can have either glide-type or shuffle-type core structure. The core of glide-type dislocations (Figure 2.5 (a)) consists of an eight-atomic ring with an inner atom and a dangling bond and the shuffle-type (Figure 2.5 (b)) can be derived from the first by omitting the inner atom and connecting the remaining free bonds. Since zinc-blende structure is non-centrosymmteric, dislocation can have two opposite polarity. If in III-V compounds the extra half plane ends either in row of group III or V atoms, group III or V atom will be located at the most distorted core positions and consequently the so-called A-dislocation or B-dislocation will be formed, respectively [43, 44].

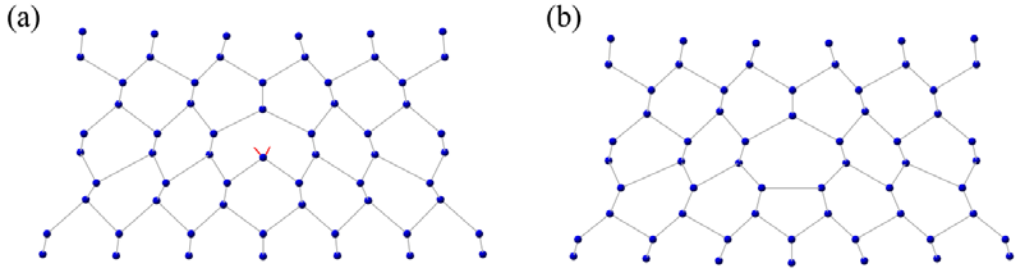

Figure 00.5: (a) Glide-type and (b) shuffle-type models of a Lomer dislocation core.

As the Burgers vector of 60° dislocations lies on the {111} easy slip planes, they can readily propagate into the film and form the so-called threading dislocations. The formation of threading dislocations deteriorates the electrical properties and degrades the film. It has been shown that using the vicinal Si (001) can reduce the probability of the formation of type II dislocations and, as a result, threading dislocations. It is also suggested that an additional strain field, induced by a strained-layer superlattice (SLS) [24, 41], can prevent the propagation of threading dislocations by bending them toward the substrate or forcing them to annihilate each other. SLSs, initially proposed by Esaki and Tsu [45], are a succession of thin layer of alternating composition with a larger lattice constant which produces a compressive force called the Peach-Koehler force [24, 46]. The Peach-Koehler force depends on the strain and the layer thickness. The layer thickness needs to be less than the critical thickness to avoid formation of additional misfit dislocations. Blakeslee and Mathew [47] have proposed a model to predict the critical thickness from the forces on dislocation lines.

2.3.2 Stacking Fault and Twins

The fcc structure is produced by a proper stacking of layers of closed packed {111} planes denoted at ABCABC packing sequence. Alteration in this staking sequence results in formation of stacking faults. Dissociation of a perfect dislocation with Burgers vector of $\frac{1}{2}\, a < 110 >$ into two Shockley partial dislocations with Burgers vector of $\frac{1}{6}\, a < 112 >$ forms an intermediate stacking fault bounded with these two partials which is shown in Figure 2.6. As it is seen, the Burgers vector of these partial dislocations is such that the atoms sheared into different type site, e.g. B to C or vice-versa. However, the stacking sequence is unaltered by the passage of complete dislocation (B to B site). A stacking fault can also be formed by removing or inserting one double atom {111} plane described as intrinsic or extrinsic stacking faults, respectively. These types of stacking faults are bounded by Frank partial dislocations [44, 48]. The width of the stacking fault depends on stacking fault formation energy i.e. the cost of misplaced crystal plane from its expected stacking sequence [44].

The other common planar defects in III-V compound semiconductors are twins. Twins are formed when the stacking sequence of {111} planes are reversed (transition from ABC to CBA stacking sequence) by a shift of each consecutive layer after initially formed stacking fault [49]. The formation of stacking faults and twins were initially attributed to coherency (lattice mismatch) and thermal stresses (mismatch in thermal expansion coefficient) and called deformation stacking faults and twins. However, later it was shown [50, 51] that major stacking fault and twining occur during the initial stages of nucleation and growth and result from growth processes, in contrast to deformation processes associated with stress-relief mechanisms. The stacking fault formation energy is in order of

thermal energy of atoms. Deposition or stacking errors and hence twins are therefore expected to occur frequently [51].

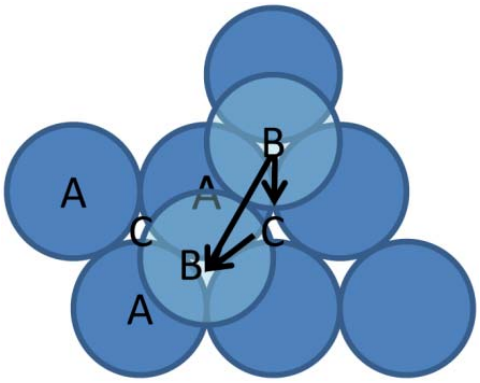

Figure 00.6: Slip on a {111} plane of a diamond- (or zinc-blende-) type crystal crystal for a glide-set dislocation. A perfect ½ <110> dislocation can split into two Shockley partial 1/6< 112> dislocations.

Twin boundaries are known to act as scattering centres and therefore to be less detrimental defects compared to the defects that produce dangling bonds [44, 52]. However, in zinc-blende structure bonding characteristics across the twinned and epitaxial regions influence the physical properties of the twins [53]. As it is seen in schematic ball and stick model of Figure 2.7(a), paratwins (also known as reflection twins) comprise anti-site (III-III or V-V) bonds across the boundary and hence, are more deleterious than orthotwins (also known as rotation twins) (Figure 2.7 (b)) for electrical properties of semiconductors [54]. Moreover, intersection of twins with different habit planes or formation of higher-order twins results in incoherent interfaces comprising dangling bonds and trapped charges [55].

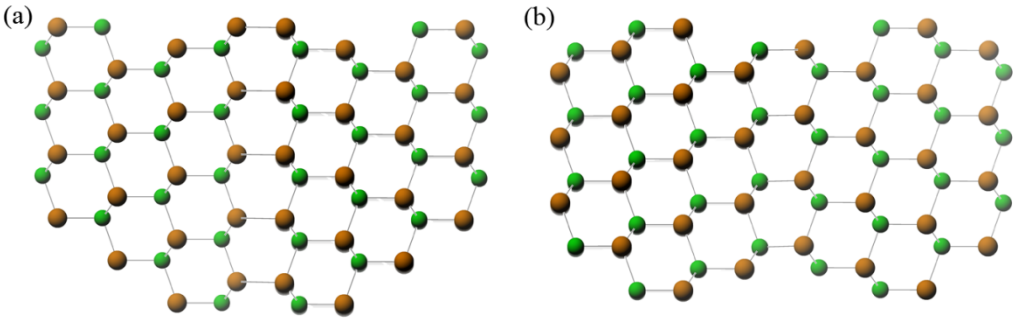

Figure 00.7: Ball and stick model of (a) paratwin and (b) orthotwin boundaries in zinc-blende structure.

2.3.3 Anti-phase Boundaries

The other planar defects of particular interest in III-V semiconductors grown on Si are anti-phase boundaries (APBs). There are two nonequivalent orientations of III-V compounds associated with interchange of group III and V sublattices with respect to two equivalent sublattices of Si. As a result, nucleation reversal is likely in growth of polar III-V epilayes on non-polar Si substrates. Between domains in an anti-phase relation, group III and V constituents interchange occupation from one fcc sublattice to the other and hence crystal polarity and bonding directionality are reversed (Figure 2.8 (a)). Anti-phase domains, i.e. domains separated by anti-phase boundaries (APBs), are therefore an inherent hindrance to the growth of a polar film on a non-polar substrate. However, it is expected that the preferential initiation of the growth with one of the species in the epitaxial growth with molecular beam epitaxy (MBE) prevents the sublattice reversal during the nucleation of III-V compounds on Si. As a consequence, the intrinsic single atomic steps of a/4 <001> height on the Si substrate surface [56] have been postulated as the main source for the APB

formation (Figure 2.8 (b)). APBs are characterized by anti-site (wrong) bonds, i.e. cation-cation and anion-anion bonds.

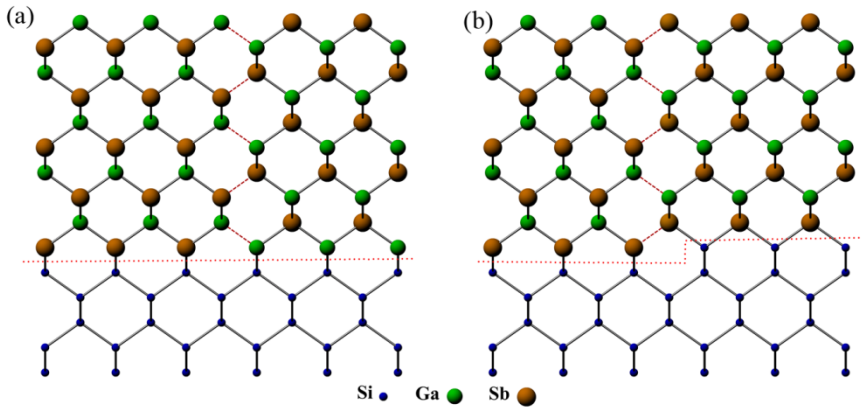

Figure 0.8: APB in GaSb film grown on Si due to (a) mixed nucleation and (b) single step at Si surface.

2.3.3.1 Crystallographic Orientation of APBs

APBs can be divided in three types: a) boundaries with equal number of anti-site bonds of both elements (stoichiometric APBs), b) boundaries with solely the wrong bonds of either III-III or V-V, and c) a mixture of an unequal number of them (where the latter two types are non-stoichiometric APBs). The stoichiometric APBs occur on {110} and {211} planes; however, APBs on {100} and {111} planes are comprised of exclusively the same anti-site bonds (i.e. all III-III or V-V bonds) while APBs on {113} planes contain an unequal mixture of both type of wrong bonds (both III-III and V-V bonds) [56-59]. Calculations of the formation energy of APBs from the simple wrong-bond counting method [60] to more sophisticated approaches based on first principles [61] and density functional theory (DFT) [62, 63] suggest that the {110} APBs have the lowest formation energy. Moreover, formation energy studies theoretically propose some

models for self-annihilation of initially {110}-oriented boundaries based on occasional kinks [61] and faceting to other low energy planes such as {112} and {113} [61, 62]. The faceting of APBs has been observed in GaP/Si and GaAs/Si and has been suggested as a possible mechanism of self-annihilation [7, 56, 64-68]. Molina *et al*. have also suggested that APBs do bend due to interaction with dislocations and consequently are annihilated [69]. It has experimentally been observed that a regular array of steps, induced by the slight misorientation of the substrate surface towards specific directions, promotes the APB's self-annihilation in GaAs on group IV substrates [67, 68, 70-77]. Furthermore, high temperature annealing of offcut substrates leads to the formation of the double-atomic height steps and APB suppression [25, 78-80].

2.3.3.2 Detecting APBs with TEM

APBs are similar to grain boundaries in this aspect that both perturb the periodicity of the lattice and have therefore similar effect on electrical and optical properties. The lattices of domains across the APB negatively coincide [44], i. e. atoms are switched to wrong sites; however, there is no mismatch across APBs. The characterization of APBs is therefore not only important to understanding the origins of the defect formation but is also relevant since APBs are electrically active defects. In fact, APBs act as non-radiative recombination centers [44, 64, 81] and, as a result, are the most deleterious planar defect [44] for many applications. APBs have been studied through a variety of transmission electron microscopy (TEM) techniques including convergent beam electron diffraction (CBED) developed by Taftø and Spence [7, 44, 58, 82-84], dark-field imaging with two opposite ±200 superlattice reflections [56, 65, 85, 86], and two-beam condition dark-field imaging using the 200-type superlattice reflections [69, 87].

In the CBED technique {002} reflections with two high order odd indexed reflections in first order Laue zone (FOLZ) are coupled. The alternatively constructive and destructive interactions results in contrast reversal of Kikuchi lines in (200) and (-200) reflections. Imaging methods with superlattice reflections are based on the sensitivity of these reflections to atomic number of occupants of sublattices due to changes in structure factors. Therefore, the superlattice reflections can be used for detecting the interruptions in sublattice occupancies.

The APBs observed using the above techniques have been characterized using two distinct types of contrast: stacking fault-like fringes due to the inclination of the boundary with respect to the imaging surface and edge-on lines for APBs parallel to electron beam [56, 69, 84, 86, 88]. These TEM techniques can be used for the investigation of the phase contrast produced by the rigid body translation of the wrong bonds [58, 89, 90]. Moreover, the interactions of the APBs with dislocations, grain boundaries [57, 84], and twins [9, 91-94] have been detected using conventional TEM. However, the identification of the polarity reversal in specimens with constituent atoms of large difference in atomic scattering factor such as GaSb using the CBED technique is challenging. In addition, investigations of the atomic arrangement at the interface between the film and the substrate using high resolution transmission electron microscopy (HRTEM) is also challenging due to the strong dependency of images on specimen thickness and defocus conditions [9, 92]. Therefore, misidentification of APBs with other planar defects, e.g. microtwins, can lead to imprecise and even incorrect conclusions on the effectiveness of the substrate type and growth conditions [8].

2.4 Antimonide-based Heteroepitaxy on Si (001)

Malik *et al.* [95] have reported the very first growth of GaSb on Si substrates. Prior to their work, majority of the Sb-based films and quantum well (QW) structures had been grown on GaAs as a substrate [96-98]. They used AlSb buffer layer to grow multilayers of GaSb/AlSb by MBE on Si since it had previously been demonstrated [96-98] that AlSb buffer layers can significantly affect the quality of GaSb growths on GaAs substrate. The TEM and Normarski interference microscopy characterization demonstrated that films contain high density of threading dislocations and anti-phase disorder. However, this work was a considerable building block upon which subsequent research was initiated.

2.4.1 Growth Mechanism of Sb-based compounds on Si

High lattice mismatch of Sb-based compounds presents fundamental growth problems and hence, understanding the growth mechanisms of GaSb and AlSb films is essential for growing high-quality films on Si. Therefore, epilayers of AlSb and GaSb were grown on Si and GaAs substrates, while the film nucleation was investigated using in-situ reflection high-energy electron diffraction (RHEED) during deposition. The evolution of deposited layers at various thicknesses has also been studied by atomic force microscopy (AFM). These studies demonstrate that in GaSb epitaxy on either Si or GaAs, growth initiates by formation three dimension (3D) GaSb islands with large vacant area in between [6, 99-101] the islands and approximate density of 1.25×10^{8} cm^{-2} at thickness of 5 nm (Figure 2.9) [100].

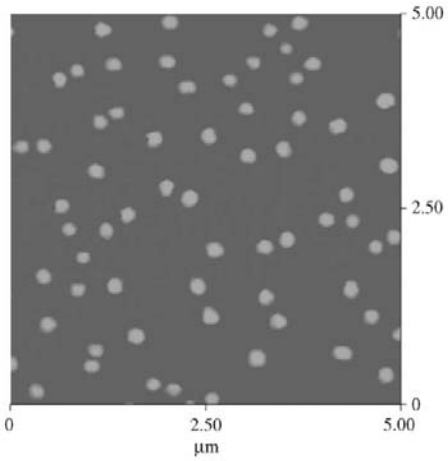

Figure 0.9: AFM image of GaSb islands on Si substrate with deposition thickness of 5 nm [100].

These observations were attributed to higher surface energy of GaSb compared to Si [Ref. 100]. Continuation of deposition results in an increase of GaSb islands size forming elongated islands with an average size of 200 nm in diameter and 100 nm in height [6, 100] due to high surface diffusion of Ga under Sb flux [100]. Kim et al. have shown that some of these large islands are not coalesced, even in thicknesses greater than 250 nm. Eventually, planar growth occurs just after coalescence of all islands, leading to the formation of a rough interface between GaSb and Si [Ref. 101]. It is also observed that GaSb islands grown on GaAs coalesce in considerably smaller thickness than GaSb/Si heteroepitaxy [99]. TEM studies of GaSb epilayers grown on the Si substrate indicates that they consist of large amounts of planar defects and severe multiple twining (Figure 2.10). It is postulated that these twins form in order to tilt the growth direction and reduce the lattice mismatch [101, 102]. High defect densities inside GaSb islands are attributed to its high lattice mismatch with Si and weak atomic bonding between Ga and Sb [103].

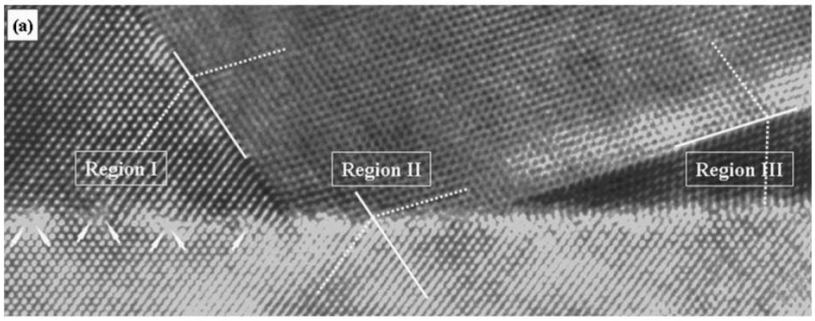

Figure 0.10: Cross sectional high resolution TEM image of GaSb and Si interface [Ref. 101].

The growth of AlSb on Si and GaAs, similar to GaSb, initiates with the nucleation of 3D AlSb islands with {111} facets and truncated on top with (100) plane [103-106]. However, AlSb are less defective than GaSb islands. The enhanced quality of AlSb compared to GaSb islands is related to stronger bonding between Al and Sb atoms [103]. Moreover, the AlSb islands are formed with higher density than GaSb on a Si surface; even at a very low thickness of 3 monolayers (ML), the AlSb islands or QD density is 10^{11}QDs/cm^2. The AlSb islands are also clearly smaller than GaSb islands [100]. These islands continue to grow and coalesce after 54 ML of AlSb deposition and eventually from planar film [104, 107]. Figure 2.11 displays the AFM images and RHEED patterns of AlSb islands on Si surface after various monolayers of AlSb deposition [106].

Noh *et al.* have divided the formation of AlSb islands into three steps: formation of a 2D AlSb wetting layer (WL), formation AlSb islands on the WL and growth of islands in order to relieve the strain. They have speculated that the thickness of this WL is around 0.3 ML and is independent of growth rate [108, 109]. It seems that, for a thickness of 0.3 ML, the AlSb WL has not covered the

entire surface of Si substrate. Therefore, using the term wetting layer may not be appropriate.

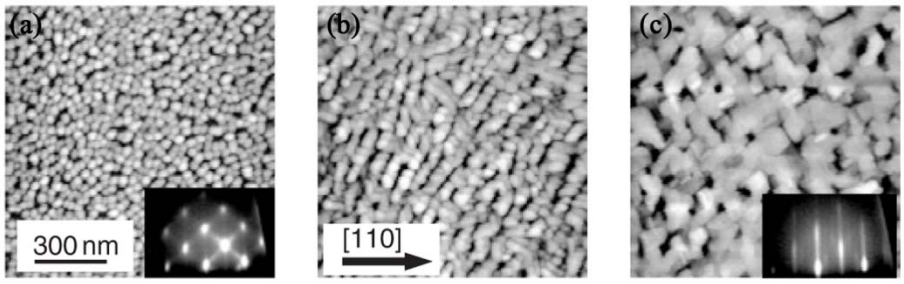

Figure 0.11: AFM images showing surface structure after various MLs of AlSb (a) 3 MLs, (b) 18 MLs, and (c) 54 MLs [106].

Rapilda et al. [105] have reported that AlSb growth on GaAs starts with 3-D islands growth on a pseudomorphic wetting layer. During the first 0.76 ML of deposition AlSb grows pseudomorphically and, after 0.8 ML, the strain is relieved by plastic relaxation and roughening i.e. by forming metamorphic QDs. Their accumulated strain monitoring shows that after 10 ML deposition, the AlSb islands coalescence is still incomplete and the growth front is not planar. Later, islands are constrained during growth and coalescence. Their studies show that at least 40 ML of AlSb is required to ensure their coalescence.

2.4.2 AlSb Buffer Layer

The growth of AlSb on Si as buffer was first explored in the mid 1980s by Malik *et al* [95]. Van der Ziel et al. [110] have reported the first device-quality GaSb films grown on Si using an AlSb buffer and a superlattice for strain relief. It was suggested that the growth mode of AlSb on Si is dictated not only by large lattice mismatch but also strong inter-atomic bonds. The large lattice mismatch of

AlSb is relieved by forming AlSb islands. The strong inter-atomic bonds in AlSb prevent the defect formation in AlSb islands and facilitate the island coalescence within thickness of <100nm. Therefore arrays of almost unifrom AlSb quantum dots (QDs) can be used as nucleation layer or buffer layer for the growth of subsequent AlSb and GaSb films [103]. AFM images of AlSb buffer layers of different thickness (Figure 2.12) show that AlSb islands are clearly smaller than GaSb islands (Figure 2.9) even though they elongate at higher deposition thicknesses. These results demonstrate that the surface energy of AlSb is also higher than Si. However, the diffusion length of Al is shorter than the one of Ga atoms and therefore the AlSb are significantly smaller than GaSb islands. The subsequent GaSb growth is drastically affected by presence of these AlSb islands as the excessive long distance diffusion of Ga atoms is interrupted at AlSb islands edges and the area between them (Figure 2.13). Hence, they enable the plateau-like growth of GaSb among AlSb islands [100]. It was reported that the nucleation of GaSb islands and their lateral growth rate are enhanced by the AlSb buffer [6].

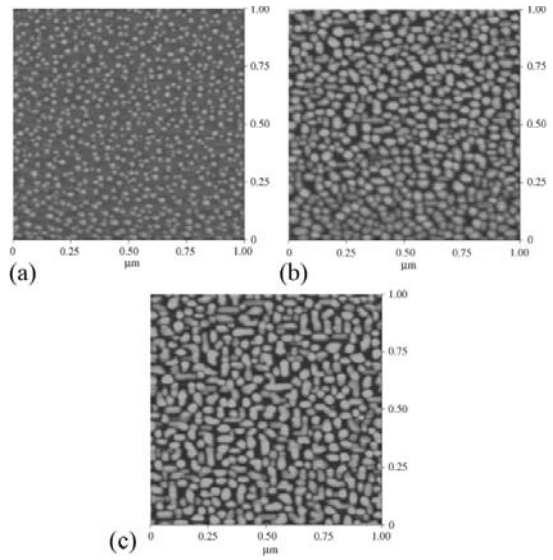

Figure 0.12: AFM images of AlSb grown on Si with thickness (a) 0.3 nm (b) 3 nm, and (c) 5 nm [100].

Akahane et al. [111] have investigated the effect of AlSb buffer layer thickness and substrate temperature on XRD rocking curves width of GaSb (004) reflection in order to verify the optimum growth conditions. They found that the AlSb buffer layer plays a key role in the growth of GaSb films of device quality. They have observed a clouded i.e. milky (not shinny) appearance of GaSb film indicating its low quality when it was grown without AlSb buffer. They have reported that the optimum substrate temperature of 500°C with a 5 nm thick AlSb buffer (Figure 2.14) offers the smallest full width at half maximum (FWHM). Monitoring the growth with RHEED confirmed that AlSb forms islands at this thickness. They also found that, at higher temperatures, Sb desorbs from the Si surface and leads to degradation of GaSb film's quality. On the other hand, at lower temperatures the Ga and Sb atoms' surface migrations are restrained. They reported that the previously observed cloudy surface of GaSb samples changes to mirror like surface by introducing the AlSb buffer with thicknesses as low as of 1 ML. They therefore postulated that AlSb acts as a surfactant. However, in reality, AlSb is not a real surfactant that exists on growth front during the growth [112]. Their observations showed that AlSb plays not only a surfactant role in improving the GaSb quality but also a buffer role in suppressing the dislocations from propagation [111, 112].

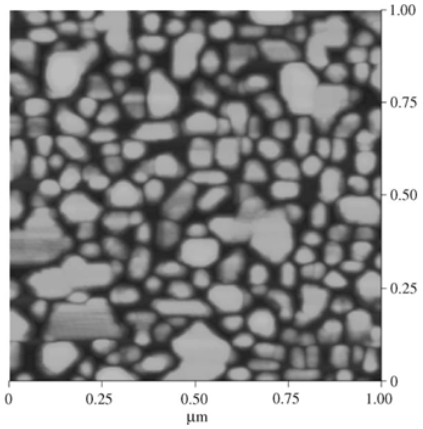

Figure 0.13: AFM image of 5 nm thick GaSb grown on AlSb buffer with thickness of 5 nm [100].

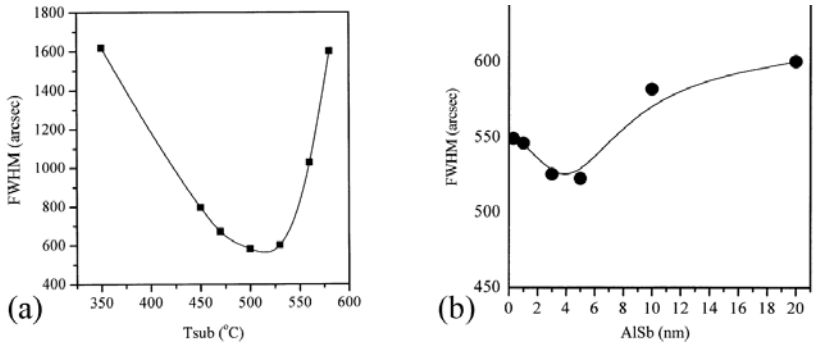

Figure 0.14: Dependence of FWHM of XRD rocking curve on (a) growth temperature and (b) AlSb buffer thickness [111].

It was also shown that the misfit strain between AlSb islands and Si is relieved almost entirely by formation of 90° misfit dislocations [104, 107] which are localized at interface and enhances the quality of subsequent GaSb or InSb films [107, 113]. The closer thermal expansion coefficient AlSb (2.55×10^{-6} /K) to Si (2.59×10^{-6} /K) compared to GaAs (6.93×10^{-6} /K) makes it a favorable buffer for

the growth of not only GaSb film [105] but also for InSb [114, 115] and $GaAs_{1-x}Sb_x$ [116].

2.5 Characterization of Sb-based compounds with TEM

Transmission electron microscopy (TEM) techniques have played a pivotal role in detecting and investigating the structure of defects and identifying their origins in GaSb epilayers grown on Si substrate. TEM techniques provide direct information on the effect of AlSb buffer on growth mechanism of GaSb. Kim *et al*. [6] have used conventional TEM imaging to see GaSb islands (Figure 2.15(a)) and their coalescence (Figure 2.15(b)) after using AlSb initiation layer. They have also studied the orientation relationships of GaSb film grown directly on Si substrate using high resolution transmission electron microscopy (HRTEM) and selected area electron diffraction (SAED) [101].

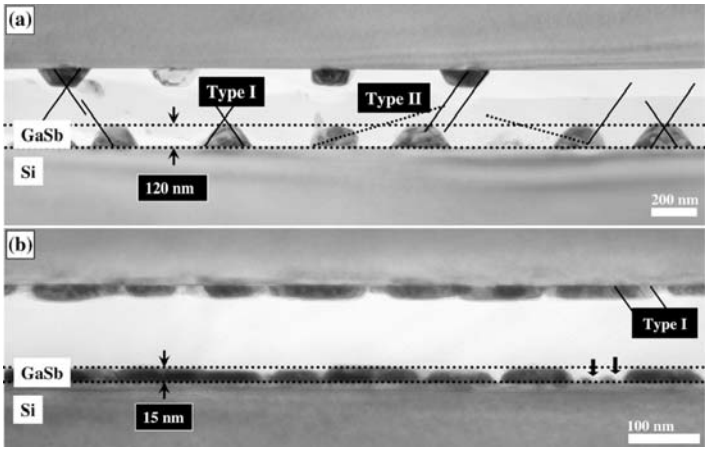

Figure 0.15: Cross-sectional bright-filed (BF) TEM image of GaSb epilayre (a) without AlSb buffer (b) with 8ML of AlSb buffer [6].

Interfacial misfit dislocations are an important mechanism of accommodating the misfit strain and they have a vital role in the quality of epi-interface and subsequent defects density of film. HRTEM images have offered a significant opportunity to investigate the Burgers vector and type of misfit dislocations at the interface of AlSb [107, 117] or GaSb film [6] and substrate. The HRTEM observations have shown that the lattice-mismatch between AlSb and Si [107] is almost completely accommodated by formation of an array of 90° misfit dislocations (Figure 2.16) while misfit strain of GaSb film on Si [6] is partially released by 30° misfit dislocations and hence leads to formation of twin boundaries that change the orientation relationships of film and substrate (Figure 2.17). Introducing the AlSb nucleation layer improves the quality of interface of GaSb and Si by forming 60° and 90° misfit dislocations (Figure 2.18) [6, 109]. However, both 30°and 60° misfit dislocations are not as effective as 90° misfit dislocations in relieving the strain.

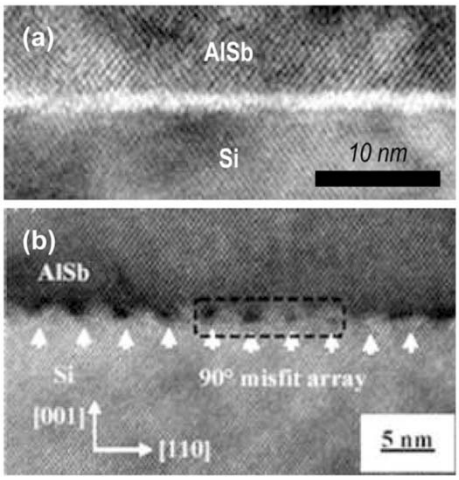

Figure 0.16: Array of 90° interfacial misfit dislocations at the interface of AlSb and Si [117].

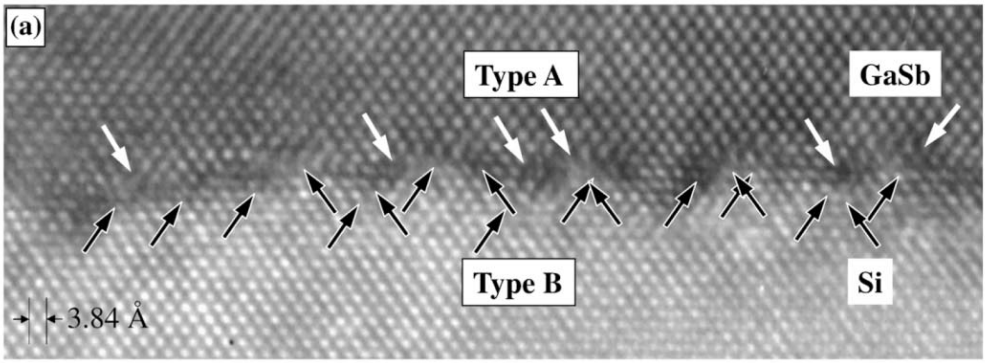

Figure 0.17: Interface of GaSb film grown directly on Si with arrows pointing partial misfit dislocations [6].

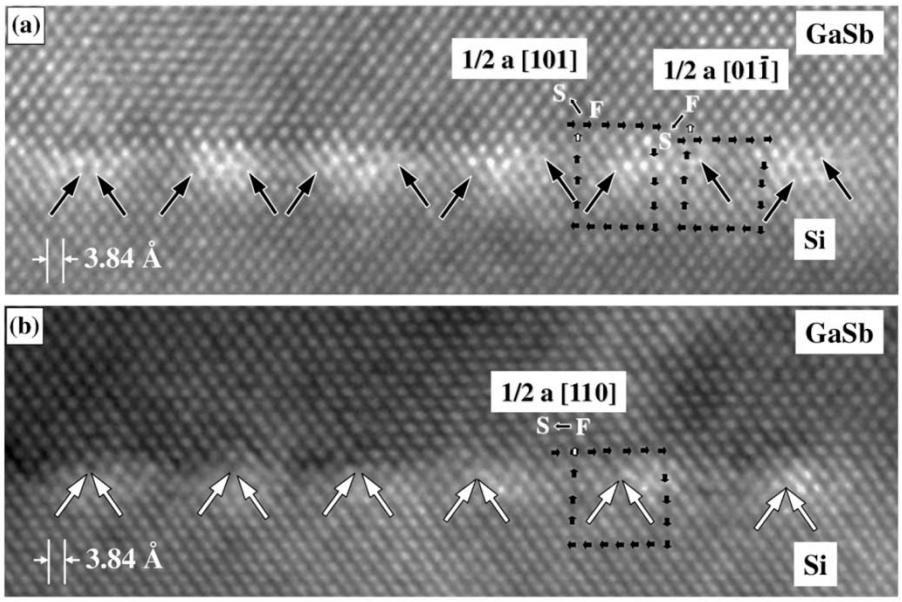

Figure 0.18: HRTEM image of the interface of GaSb/Si with AlSb buffer showing (a) 60° misfit dislocations and (b) 90° misfit dislocations [6].

Using offcut Si substrate with a regular array of steps on the surface, Huang *et al*. [8] have achieved AlSb films with an array of 90° interfacial misfit dislocations (Figure 2.19). They have also reported that with choosing a proper offcut angle, the formation of APBs is suppressed. The defects identified by this group as seen in Figure 2.20(b) are {111}-oriented APBs. However, due to lack of details on polarity reversal, these defects are likely to be microtwins, misidentified as APBs. Using HRTEM, it has also been shown that the introduction of a thin layer of low temperature AlSb [118, 119] or GaSb [118] will significantly improve the quality of GaSb film grown on GaAs substrate by formation of an array of 90° misfit dislocations at the interface.

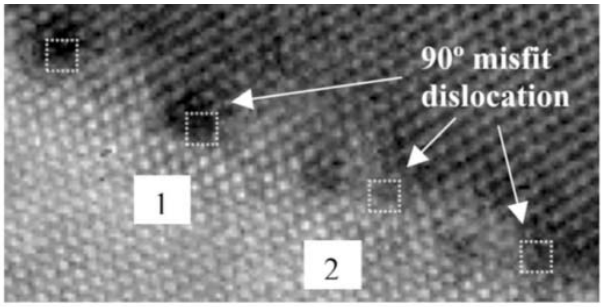

Figure 0.19: Array of 90° misfit dislocations at the interface of AlSb grown on 5° offcut Si substrate [8].

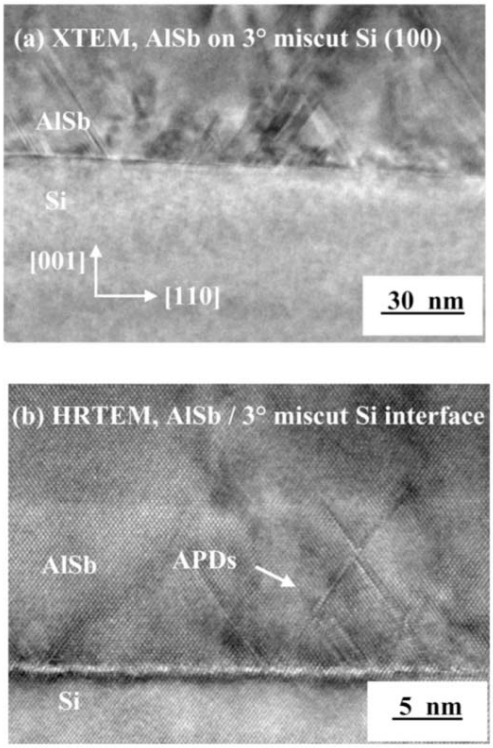

Figure 2.20: Cross-sectional TEM images of APDs in AlSb film grown on Si with an offcut angle of 3° at (a) low-resolution and (b) high-resolution condition [8].

The effect of growth conditions such as one-step vs. two-step growth [19], temperature and V/III flux ratio [20] have been investigated with various TEM techniques.

2.6 Summary and Research Objective

The band-gap properties of III-Sb based semiconductors provide a unique opportunity for a variety of applications. Using Si substrates for growing compound semiconductors has significant advantages, such as the low cost, high quality of the wafer supply and the numerous benefits of using a well-established manufacturing platform. Study of misfit strain relief mechanism and interfacial misfit dislocations as well as growth mechanism of GaSb film and AlSb buffer are of particular interest in order to improve the quality of GaSb epilayers grown on Si substrates. The initial stage of GaSb epilayer growth and the effect of AlSb buffer in improving the GaSb structure on Si have not been fully perceived. Accordingly, studying the growth of GaSb and investigating the strain relief mechanisms as major determinant of film quality can pave the path toward growth of highly lattice-mismatched heteroepitaxy.

The nucleation ambiguity inherent to polar-on-nonpolar growth of GaSb on Si is the cause of APBs, the extending defects of particular importance, at the interface. In spite of the significant impact of the conventional TEM techniques in studying of APBs, the direct observation of these defects has still remained as a challenge. Therefore, understanding the crystallographic structure and atomic configuration of APBs can present the profound insight about the polar-on-nonpolar growth. Consequently, misidentification of defects and overestimation about the effectiveness of growth conditions can be prevented.

Given the above summary, the ultimate goals of this research were therefore to study the interfacial misfit dislocations and strain distribution in GaSb films, to investigate the origin, atomic configuration, and crystallographic orientation of APBs, to understand the effect of substrate orientation in formation of APBs, and to explore the growth mechanism of the GaSb epilayer on the Si substrate using the atomic-resolution HAADF-STEM.

Chapter Three

Experimental Methods

This chapter details the method used for growing the GaSb hetero-layer on Si, TEM specimen preparation technique of the grown samples. It also includes TEM characterization techniques used in this study as well as the image simulation approach. There are various methods for growing the epitaxial films such as liquid phase epitaxy (LPE), metal organic vapour deposition, and molecular beam epitaxy (MBE). The capability of growing epitaxial layers with atomic dimensional precision down to a few angstroms and abrupt interfaces [120] are significant aspects of MBE which makes it a favorite choice for research-based growths. TEM samples of uniform thickness with least possible amorphous layers are of great importance for high resolution TEM studies. Wedge samples prepared by low-angle tripod polishing method have shown great advantage over conventional polishing methods for imaging the single atomic columns and individual dopant atoms [121]. As a result we prepared the TEM samples with low-angle tripod polishing and maintain a consistent procedure along the research to avoid the sample preparation artifacts.

3.1. Molecular Beam Epitaxy Growth

Group III-Sb based compound semiconductor epilayers (GaSb, AlSb) were deposited on nominal (001)-oriented (±0.5°), vicinal (001)-oriented (offcut 4.7° [±0.25°] towards [110] tilt direction), and nominal (211)-oriented Si substrates by a SVT Associate, Inc. molecular beam epitaxy (MBE) system. The Sb_2 flux was provided through a solid source valved-cracker effusion cell. As-received Si wafer dip-cleaned for 1 min in HF diluted to 4% in de-ionized water (DI), followed by rinsing in DI water for 30 sec, and inserted into the MBE vacuum chamber immediately thereafter. Prior to depositing the film, the Si substrate was degassed at 350°C for 15 min in a preparation chamber. Subsequent heat treatment was conducted in the main chamber by increasing the temperature to 800°C for 5 min to facilitate the surface reconstruction by removing the hydrogen terminated Si surface. It is expected that the Si surface is mainly single domain terraces [122-125] with a small number of single steps on vicinal substrates and a higher number on nominal substrates because of the larger terrace length. In order to be able to compare different GaSb film grown on Si with each other the growth conditions were rigorously maintained. Therefore, the substrate temperature was cooled down to 600°C and growth started by depositing a 5 nm thick AlSb buffer layer at a rate of 0.1 ML/s and V/III flux ratio of 2. Subsequently, the GaSb epilayer was grown at a rate of 1.0 μm/h to a thickness of 500 nm while the V/III flux ratio was kept slightly higher than 1. The insertion of thin AlSb buffer layer was carried out based on the works by Akahane *et al*. [Ref. 111]. Preliminary studies were carried out to find the optimal growth temperatures and V/III ratio resulting in lowest rocking curves full-with at half maximum for (004) reflection using double crystal X-ray diffraction (DCXRD) and overall good quality films through conventional TEM. In order to reduce the threading dislocation density for polarity studies a strained-layer superlattice (SLS)

consisting of 25 alternating AlSb and GaSb epilayers of 10 nm thickness was grown in some of the growths. The SLS was finally covered with a 1 μm GaSb layer. The deposition rate of the GaSb and AlSb layers in the SLS was 1.0 μm/hr and 0.6 μm/hr, respectively. The GaSb capping layer was grown at the same rate as in the SLS. The as-grown specimens were kept in a sealed vacuum desiccator to avoid the weathering effects.

3.2. Transmission Electron Microscopy Characterization

Epitaxial GaSb films were characterized with phase contrast-based techniques using conventional TEM for overall quality of the grown samples. Detail studies of the type of defects, their orientations and formation mechanism were carried out with Z-contrast based technique using HAADF-STEM. In order to have thorough understanding of the epitaxial layers, two orthogonal cross-sections with respect to the primary and secondary flats of Si wafer, namely two cross-sections with ⟨110⟩ zone axis for the offcut and flat (001)-oriented Si and a ⟨110⟩ and a ⟨111⟩ for the (211)-oriented specimens. Following sections detail the TEM sample preparation recipe and characterization techniques.

3.2.1. TEM Sample Preparation

The cross-sectional TEM specimens were polished mechanically using Allied High Tech MultiPrep™ System (Figure 3.1) in order to assure the uniform thickness with considerably thinner amorphous layer. The general outline of the procedure is as follows: first, two bars of approximately 2×10 mm were cleaved from the main samples using a diamond scriber and glued with film sides facing together with a standard quick setting EPO-TEK® 353ND epoxy (so called 110 epoxy) to make a sandwich. A dummy Si piece may be added to obtain a

thickness of about 1 mm. Reference to the absolute orientations was tracked precisely. The glue layer between the sample pieces should be as thin as possible about <100 nm thick. The sandwich was cut in pieces of 1.5×2 mm perpendicular to glue line using a wire saw. The sample was then glued to cross-sectioning paddle with wax. Then the thickness of sample was measured using a digital micrometer. Afterwards, the first side of the sample was polished down to a thickness of approximately 400 μm via diamond lapping films with grit size of 30 μm, 9 μm, 3 μm, 1 μm, 0.5 μm and 0.1 μm. In general the "rule of three" defines the polishing recipe. As a damaged layer forms during mechanical polishing with a layer thickness approximately three times the size of the grit used to do the polishing, each subsequent film must remove the damage that has been created. The load of 200 grams at 30 rpm and water as lubricant were used with the exception of the lapping films with 0.5 and 0.1 μm grit size where the Allied GreenLube™ was applied. As GaSb film and Si substrate showed significantly different polishing rates, the colloidal silica polish was not applied in order to maintain the length of GaSb film approximately at the same level as Si substrate. Subsequently, the sample was removed from cross-sectioning paddle using Acetone and glued to TEM wedge thinning paddle using Loctite® 460 instant adhesive by Henkel with first side facing to the top surface of the paddle. After thinning the sample to the thickness of 150 μm with the 30 μm lapping film, the polishing angle of 2° was applied. It is found that a 2° wedge decreases the chance of the sample curling and provides samples robust enough to be handled safely. Then the sample was polished with 3 μm film to the thickness of 50 μm while it was being checked with an optical microscope to monitor the thickness as well as the wedge condition. Starting the wedge, the load was lowered to 100 grams to avoid the damage to sample. Below the thickness of 50 μm, the 1 μm lapping film was used to thin the sample to below 10 μm along with continuous monitoring with microscope until the wedge started i.e. the first thickness fringes

appear. Later, a 0.5 μm diamond lapping film was used to polish the sample till the interference fringes appear and the 0.1 μm diamond lapping film was used to have more defined fringes. Figure 3.2 displays an optical micrograph of an ideal polished Si sample. Eventually, the sample was removed from the paddle and rinsed in acetone and methanol alternatively to remove the residual contaminants from polishing and glue and the sample was then glued to oval molybdenum ring with epoxy 110.

Figure 0.1: MultiPrep^{TM} system by Allied High Tech Products, Inc [126].

Using this method of TEM sample preparation reduces or even eliminates the need for ion milling the sample. Therefore, the ion milling recipe was determined based on the amount of the scratches, interference fringes, and edge of the wedge condition after checking the sample with conventional TEM. Based on the polishing recipe, as well as preliminary checking with TEM, samples were cleaned by a Technoorg Linda Gentle-mill (Figure 3.3) with 300-800 eV Ar ions for approximately 60 minutes to remove the residue of polishing contamination.

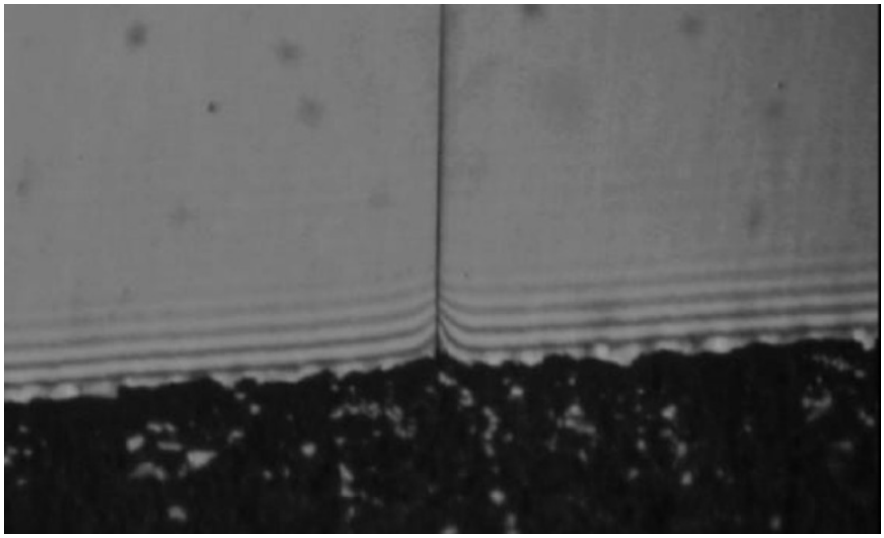

Figure 0.2: An optical micrograph of an ideal polished Si sample [Ref. 121].

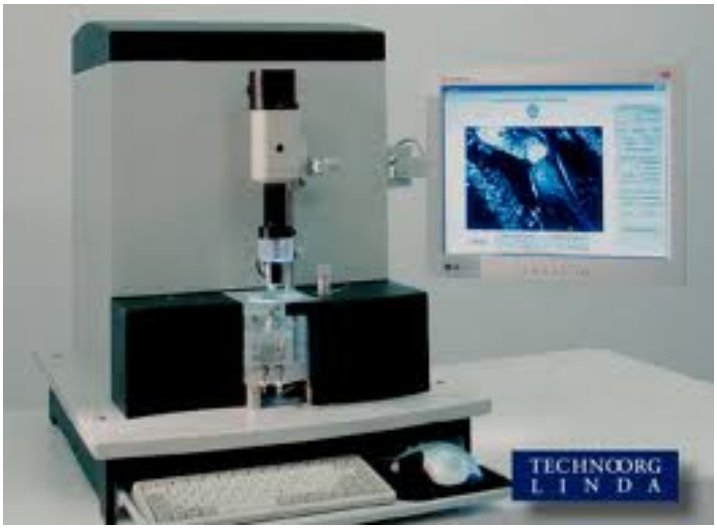

Figure 3.3: A Technoorg Linda Gentle Mill [127].

3.2.2. Conventional TEM

The phase contrast observations were performed on a Philips CM12 conventional TEM fitted with LaB_6 filament operating at 120 keV. The overall quality and the preliminary identification of defects in GaSb epilayers were studied using phase contrast imaging techniques, including bright-field (BF), strong-beam centred dark-field (DF), two-beam condition DF and BF images. BF images were simply obtained by placing the objective aperture around the straight through beam. While centred DF images with enhanced contrast were formed by centring the scattered beam in in-axis objective aperture for investigating the defects. However, in order to obtain good strong diffraction contrast, the TEM specimen were titled in DF or BF mode to two-beam conditions in which one of the diffracted beams and the direct beam were strongly excited. In addition to the enhanced contrast with respect to standard BF and DF image, BF and DF images with two-beam condition contain orientation information since the contrast corresponds to a specific set of planes rather than general scattering. Figure 3.4 displays the schematic of three standard two-beam conditions. In this research, the 002, -220, 02-2 and 200 reflections were used for two beam condition conventional TEM studies.

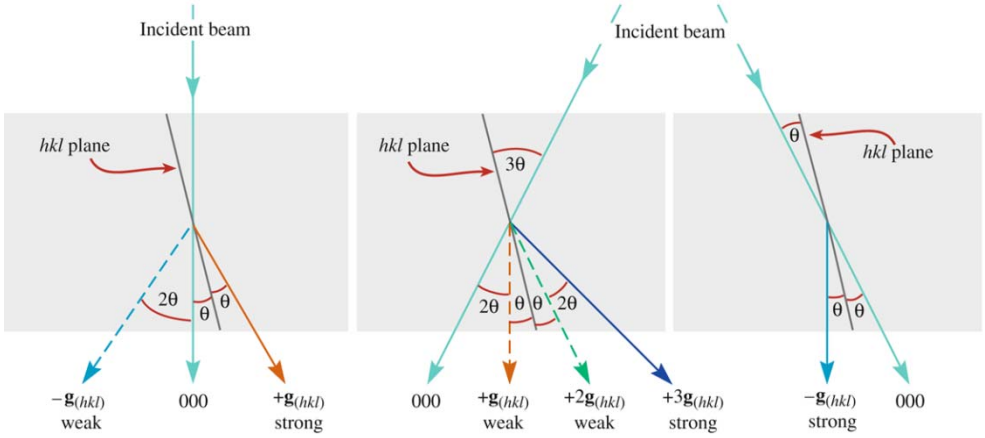

Figure 0.4: (a) Standard two-beam conditions involve the 000 spot and the hkl spot bright, (b) when the incident beam is tilted through 2θ so that the excited g_{hkl} spot moves onto the optic axis, the g_{hkl} intensity decreases because the g_{3h3k3l} spot becomes strongly excited, and (c) to get a strong hkl spot on axis for a DF image, it is necessary to set up a strong $-g_{hkl}$ condition first of all, and then tilt the initially weak g_{hkl} maximum onto the axis [128].

3.2.3. High Resolution Characterization

The detail structure of the epilayers was investigated using high resolution microscopy techniques to identify the types of defects, their orientations and origins more precisely. Investigations of the atomic arrangement at the interface between the film and the substrate using high resolution transmission electron microscopy (HRTEM) is challenging due to the strong dependency of images on specimen thickness and defocus conditions [9, 92]. Therefore, misidentification of defects, particularly APBs, can lead to imprecise conclusions on the effectiveness of the substrate type and growth conditions [7]. As a result, in this research a scanning transmission electron microscope (STEM) equipped with spherical aberration correctors was used. The ultrahigh-resolution Z-contrast HAADF images were obtained using a FEI Titan 80-300 “cubed” equipped with a high

brightness field-emission gun, an electron monochromator, and CEOS GmbH spherical aberration (C_s) correctors of the probe and image forming lenses. The fundamental of the various signals in STEM are detailed in following section.

3.2.3.1. Scanning Transmission Electron Microscopy (STEM)

Figure 3.5 displays a schematic of essential elements of a STEM. In STEM, a series of lenses converge the electron beam generated by electron source to a small spot, called electron probe, which moves in raster mode on sample. The electron diffraction pattern is therefore broadened to diffraction discs, known as convergent beam electron diffraction (CBED), according to the illumination convergence semiangle (α). Since the electron beam is coherent (the phases of the electron waves are in step) the interference features form at the overlap of the discs. Using different detectors underneath the sample, various signals can be detected and used for forming the image.

BF imaging with STEM can be recorded using an axial BF detector (highlighted as dark blue detector in Figure 3.5) on the overlap of the transmitted disc and two diffracted discs in which the intensity of the interference signal depends on the position of the probe on the sample. The contrast reversal in BF-STEM images can inherently occur due to the thickness and objective lens defocus change which become more subtle at interfaces and defects.

At increased scattering angle, thermal vibrations dominate the Bragg scattering. As a result coherent scattering is replaced by thermal diffuse scattering (TDS) which is an incoherent scattering. On the other hand, as the scattering angle of the electron beams increases, the intensity of the detected signal approaches to the Rutherford scattering proportional to Z^2. However due to screening effect of core atoms, this atomic number dependence reaches only to

$Z^{1.7}$ [11]. Therefore, by choosing a sufficiently large angle as the inner semiangle (β) of the ADF detector (shown as a light blue hollow detector) the contribution of the coherently scattered electron beams will not be considerable. As it is seen in Figure 3.6 the size of the ADF detector is much larger than the overlapping portions of the discs. These overlapping regions contain the interference fringes as a result of coherent scatterings. Therefore due to the size of ADF detector, the detected signal is mainly constituted of incoherent large-angle elastic scatterings. The difference between coherent and incoherent imaging with ADF and BF detector are shown schematically in Figure. 3.7. The contrast in BF imaging with small detector compared to interference region depends on the position of fringes i.e. phase of the scattering electron from atom. While ADF intensity which results of integration over multiple fringes, is not affected by the phase of the electrons. Hence, the interpretation of Z-contrast in HAADF-STEM images is more straightforward than their counterpart complementary BF-STEM images which are sensitive to strain. The strong contrast in HAADF-STEM images associated with the atomic numbers of the columns of substrate and film at interface plays a key role in understanding the origin of the defects at the interface. The size of the inner semiangle (β_1) of the ADF detector needs to be three or more times larger than the convergence semiangle (α) in order to assure the reliable interpretation of the contrast with less contribution of the phase contrast [11, 129-132].

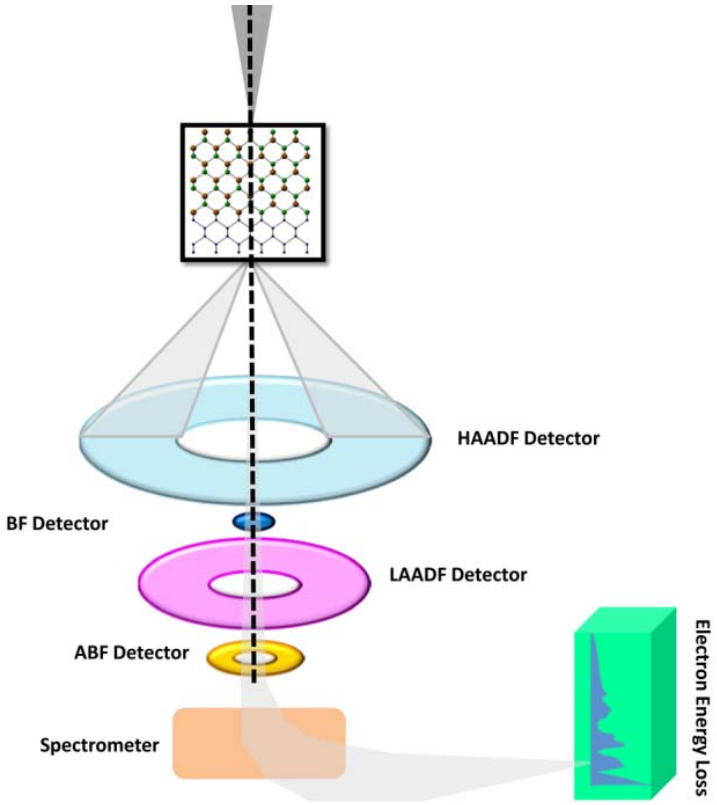

Figure 0.5: Essential elements of STEM.

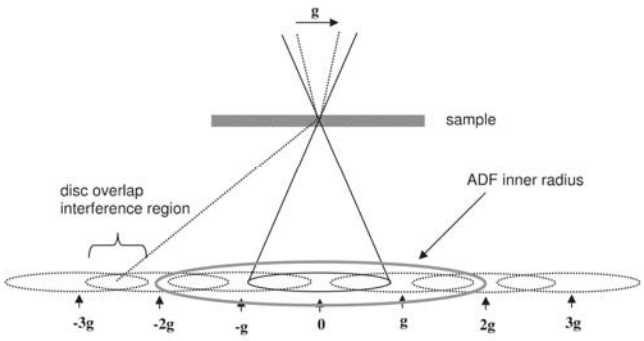

Figure 0.6: Schematic comparison between ADF detector and interface regions in discs overlap [11].

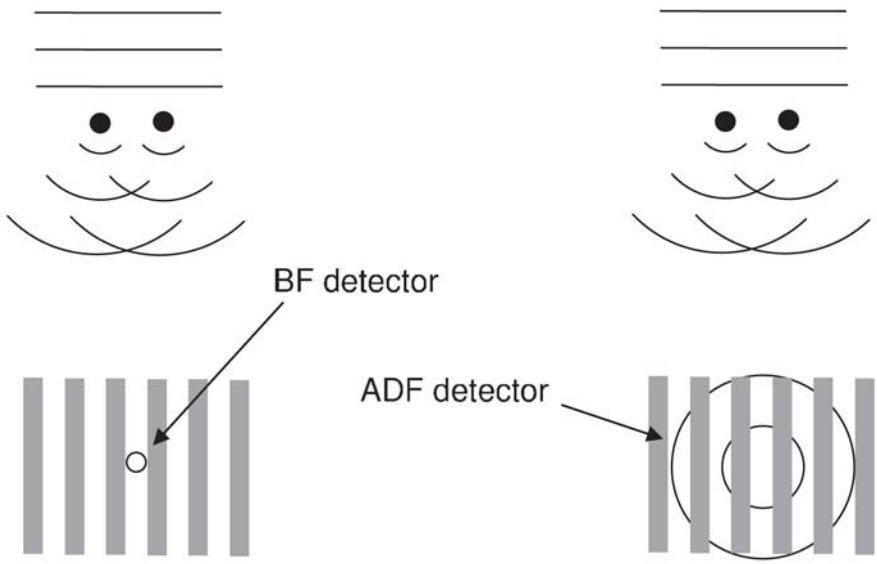

Figure 0.7: The size of BF and ADF detectors with respect to the inference fringes [11].

At an angular range lower than typical HAADF with reduced inner semiangle of detector (as shown by pink detector in Figure 3.5), another type of signals can be detected which are sensitive to the strain resulted from imperfections in crystal. These signals are the contribution of additional diffuse scatterings called Huang scatterings due the crystal imperfections [133, 134]. This range of detection angle which is lower than HAADF with small inner semiangle also referred as low-angle annular dark-field (LAADF) can simply be achieved by changing the camera length to some modest collection angles. LAADF as a complementary technique can be utilized to investigate the strain effect of defects.

If the outer semiangle (β_2) of the annular detector gets as small as the direct beam disc in CBED pattern and with the inner semiangle excluding the

central bright region of the disc, the signal of light atoms will be detected. As atoms will appear dark on a bright background, this method has been named annular bright-field (ABF). This technique is of specific interest when heavy and light atoms are located close to each other. While large-angle scattering occurs close to nucleus and are Z sensitive, the small angle scattering at the edge of atoms are comparable for light and heavy atoms due the comparable electron density at edge of atoms. Therefore, the ABF detector (highlighted as yellow detector in Figure 3.5) can detect the light and heavy atoms simultaneously. This technique has been used to successfully imaged hydrogen atoms [135-137].

As a result, in order to be able to intuitively interpret the STEM images, the optimal convergence semiangle and appropriate detection condition based on the techniques mentioned above was chosen. Additionally, the precise and thorough procedure of aberration correction was carried out to enhance the resolution of the microscope. Table 3.1 is summary of microscope setting conditions used for HAADF-STEM imaging.

Table 0.1: Setting condition of STEM used for experimental observations.

Mode	Tension (keV)	Convergence Semi-angle (mrad)	Detector Inner Semi-angle (mrad)	Camera Length (mm)
HAADF-STEM	300	17.6	48	91.1

3.2.3.2. Spherical Aberration Correction

The spatial resolution in STEM is defined by size of the probe which is formed by objective lenses. Condenser lenses also de-magnify the electron source

to a probe. The typical wavelength of electrons is in picometre range for usual accelerating voltages of 100 to 300 keV. However the resolution limit of most TEMs is 100 times worse than wavelength limit due to the aberration of lenses. Circular electromagnetic lenses of TEM suffer from aberrations similar to light-optical lenses. However, unlike to light-optical lenses it is not possible to make round electromagnetic lenses with negative spherical aberrations and compensate the positive spherical aberration. This finding is named Scherzer theorem after Otto Scherzer first introduced it in 1936 [138]. Figure 3.8 illustrates main lens aberrations. Spherical aberration (C_s) results from the change in focal point of electron rays with different distance form optical axis. The energy spread on electron beams causes a spread in focusing distance based on the energy of the rays called chromatic aberration (C_c). On other hand, to avoid the damages to specimen the energy of electron beam should be less than knock-on threshold constituent elements; therefore increasing the accelerating voltage is not only an expensive but also harmful way of enhancing the resolution.

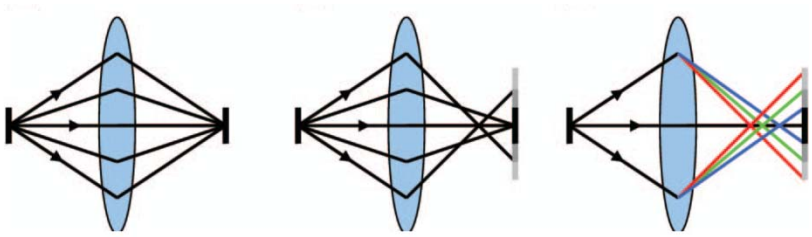

Figure 0.8: Schematic of the main lens aberrations. (a) a perfect lens with no aberration (b) higher angle rays is overfocused due to the Spherical aberration, and (c) chromatic aberration causes rays at different energies (indicated by color) to be focused at different points [139].

Using the high brightness field-emission gun (XFEG) in our FEI Titan 80-300 cubed the energy spread of the beam is small; as a result the effect of C_c is

smaller than C_s. However, C_s will change the focal point of the rays proportional to cube of the angle of the ray with optical axis resulting in a three-fold aberration such that:

$$\Delta x = C_S \theta^3 \qquad (3-1)$$

which C_S is spherical aberration or so-called three-fold aberration. When the phase change of the rays in demagnified electron beam exceeds the $\pi/2$, destructive inference of electron rays prevent formation of point probe. Therefore an objective aperture is used to exclude the contribution of highly aberrated rays in the formation of electron probe. For a given objective lens with the spherical aberration of C_S, the radius of objective aperture to be used is:

$$\alpha = 1.3\lambda^{1/4} {C_S}^{-1/4} \qquad (3-2)$$

The full width at half maximum (FWHM) of the STEM probe is a measure of resolution which is given by [11]:

$$d = 0.4\lambda^{3/4} {C_S}^{1/4} \qquad (3-3)$$

The finite source size, chromatic and spherical aberrations are bottlenecks for ultimate resolution of STEMs. The probe size in STEM either in diffraction-limited or aberration-limited conditions is affected by aberration of lenses [11]. Therefore, correcting the aberrations of lenses is the key point in enhancing the resolution of TEMs. The surface of the wave front will be affected due to the aberrations of lenses with respect to un-aberrated wave front. The aberration function (3-4) of lenses can be explained by a Taylor expansion in which the coefficients are various types of aberrations. The lower the order of the aberration the easier it can be corrected. The various types of aberration are listed in Table 3.2 [140]. In 1947, Scherzer [141] realized that with using non-rotational

symmetric electromagnetic lenses, the aberration of lenses can be compensated. However, the development of aberration correctors was not achieved until last two decades.

$$\chi(\omega) = R_e\{\tfrac{1}{2}\omega\bar{\omega}C_1 + \tfrac{1}{2}\bar{\omega}^2A_1 + \omega^2\bar{\omega}^2B_2 + \tfrac{1}{3}\bar{\omega}^3A_2 + \tfrac{1}{4}(\omega\bar{\omega})^2C_3 + \omega^3\bar{\omega}S_3 + \tfrac{1}{3}\bar{\omega}^4A_3 + \omega^3\bar{\omega}^2B_4 + \omega^4\bar{\omega}D_4 + \tfrac{1}{5}\bar{\omega}^5A_4 + \tfrac{1}{6}(\omega\bar{\omega})^3C_5 + \tfrac{1}{6}\bar{\omega}^6A_5 + \cdots\} \quad (3-4)$$

Aberration correctors are groups of asymmetric magnetic multipoles (Figure 3.9) that induce a negative C_s that compensate the positive Cs of the lens and hence focus the electron beam with various angles at the same point. Quadrupole-octupole-QO correctors (developed by Krivanek et al. 1997) [142] and hexapole correctors (developed by Haider, 1992) [143] which are named based on their rotational symmetry are two main types of aberration correctors (Figure 3.10). The QO assembly is designed specifically for dedicated STEMs. However, FEI Titan 80-300 cubed takes the advantage of hexapole which basically can reach same level of aberration correction as QO design except that the QO correctors [144] can correct the first-order chromatic aberration. Using the CEOS GmbH hexapole spherical aberration (C_s) correctors of the probe, a significantly reduced size of probe is achieved that enables the higher resolution of STEM and increased objective aperture size. With increased aperture size the diffraction-limited probe size is pushed to smaller size which provides higher spatial resolution of microscope. The larger aperture size provides higher probe current for microanalysis when the probe size is controlling the condition [11].

Table 0.2: Wave aberration coefficients and their allowed magnitude calculated from the π/4 limit at 200 kV [140].

Coefficient (symbol)	π/4 limit	π/4 limit at 200 keV for g_{max}		
		4/nm	7/nm	10/nm
Defocus (C_1-Δf)	$\frac{1}{4}(\lambda g_{max}^2)^{-1}$	6.2 nm	-2.0 nm	1.0 nm
Scherzer focus:		-69 nm	-22 nm	-11 nm
Twofold astigmatism (A_1)	$\frac{1}{4}(\lambda g_{max}^2)^{-1}$	6.2 nm	2.0 nm	1.0 nm
Threefold astigmatism (A_2)	$\frac{3}{8}(\lambda^2 g_{max}^3)^{-1}$	0.93 nm	0.17 nm	60 nm
Axial coma (B_2)	$\frac{1}{8}(\lambda^2 g_{max}^3)^{-1}$	0.31 nm	58 nm	20 nm
Spherical aberration (C_3, C_4)	$\frac{1}{2}(\lambda^3 g_{max}^4)^{-1}$	0.12 nm	13 µm	3.2 µm
Scherzer focus:		1.3 nm	130 µm	32 µm
Fourfold astigmatism (A_3)	$\frac{1}{2}(\lambda^3 g_{max}^4)^{-1}$	0.12 nm	13 µm	3.2 µm
Star aberration (S_3)	$\frac{1}{8}(\lambda^3 g_{max}^4)^{-1}$	31 nm	3.3 µm	0.79 µm
Fivefold astigmatism (A_4)	$\frac{5}{8}(\lambda^4 g_{max}^5)^{-1}$	15 nm	0.94 µm	0.16 µm
Axial coma (B_4)	$\frac{1}{8}(\lambda^4 g_{max}^5)^{-1}$	3.1 nm	0.19 µm	32 µm
Three lobe aberration (D_4)	$\frac{1}{8}(\lambda^4 g_{max}^5)^{-1}$	3.1 nm	0.19 µm	32 µm
Spherical aberration (C_5)	$\frac{3}{4}(\lambda^5 g_{max}^6)^{-1}$	1.8 nm	64 µm	7.6 µm
Sixfold astigmatism (A_5)	$\frac{3}{4}(\lambda^5 g_{max}^6)^{-1}$	1.8 nm	64 µm	7.6 µm

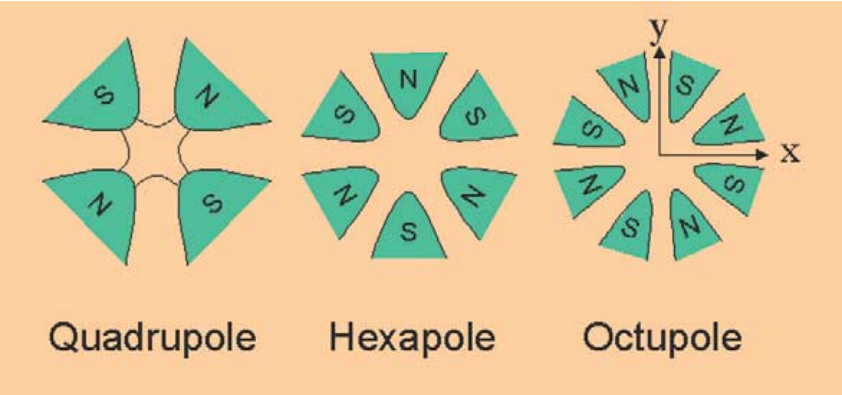

Figure 0.9: Multi-pole lenses with electron path perpendicular into page [144].

Aberration correctors enable the correction of the higher order parasitic aberrations such as axial coma (B_2) and three-fold astigmatism (A_2) which cannot be simply corrected via defocusing the beam to Scherzer defocus which is the case for spherical aberration (C_3 or C_s) [11].

Consequently, for high resolution HAADF-STEM imaging, the designated procedure of probe correcting was iterated until the accepted aberration values are achieved. This aberration-corrector has the capability of correcting the aberration up to the third order. In this procedure the shape of the beam is imaged in overfocus and underfocus conditions at different tilt angle of the probe and the aberrations are measured. Defocus and two-fold astigmatism are measured through a tilt-series, so-called Zemlin Tableaus while the lens aberrations are measured via Ronchigram at different defocus and beam tilt. Figure 3.11 displays the probe shape acquired using an Au-Pt cross-grating standard sample for aberration correctors in Titan at 300 keV and probe convergence semi-angle of 17.6 mrad.

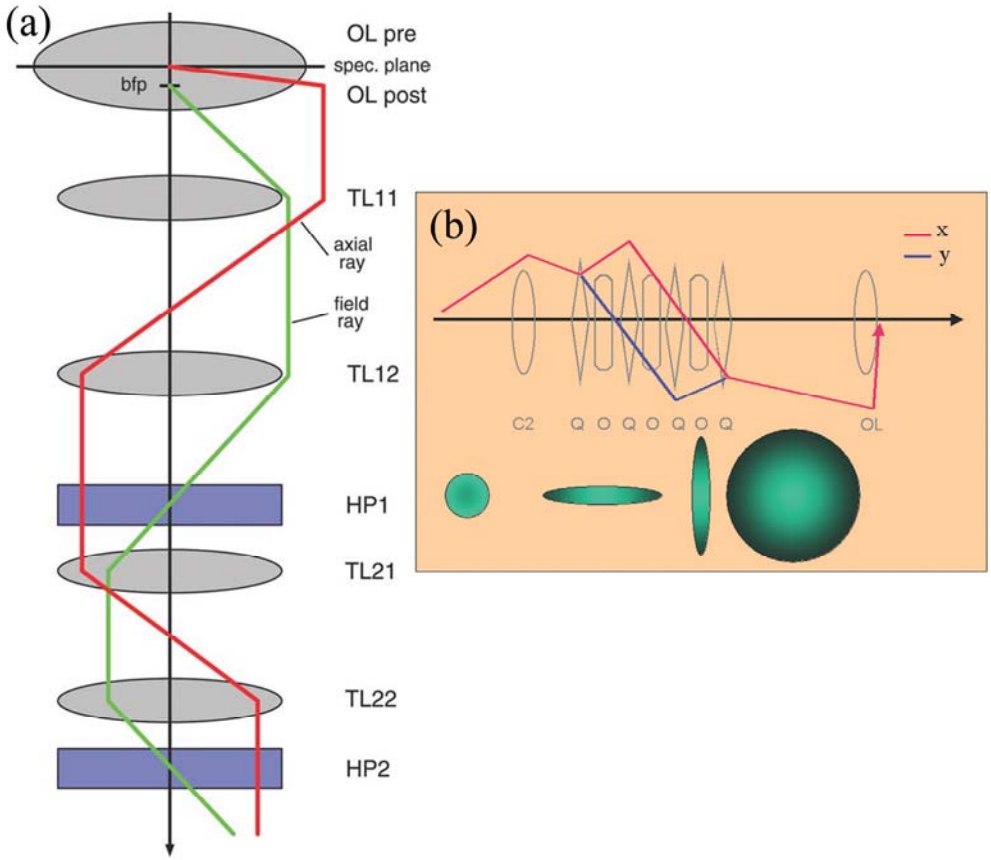

Figure 0.10: (a) Schematic of CEOS hexapole first transfer lens doublet TL11 and TL12, second transfer doublet TL21 and TL22, OL as objective lens and first and second hexapole HP1 and HP2 [145] (b) schematic QO corrector with C2 as the last condenser lens and OL as the objective lens, the crossover of beam is shown below the corrector [144].

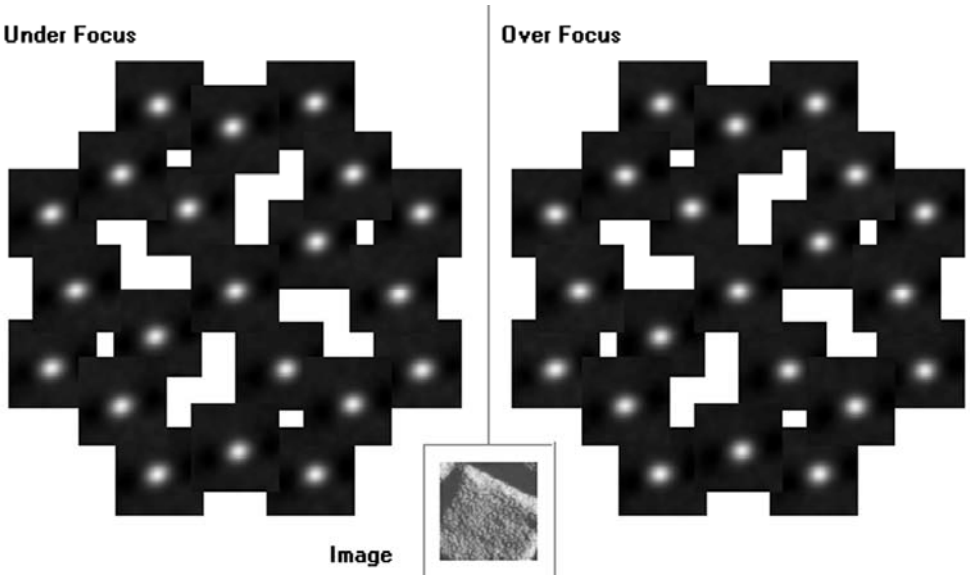

Figure 0.11: Probe shape of Titan at 300 keV with probe convergence semi-angle of 17.6 mrad acquired during the probe correcting procedure.

The computerized algorithm of this corrector measures the aberration fast enough and then feeds back the information to mulipoles in order to electromagnetic fields of the lenses in corrector are adjusted correspondingly to compensate the aberration of the microscope lens. Several iterations of the measuring and correcting procedures result in significantly reduced values of the aberration coefficients acceptable for further experimental observation of the specimen. Figure 3.12 shows the achieved values of aberration after complete alignment of microscope and correction of the probe aberrations. Figure 3.13 displays the Ronchigram of the corresponding corrected probe with extended flat phase and C2 aperture (condenser aperture) highlighted as pink circle.

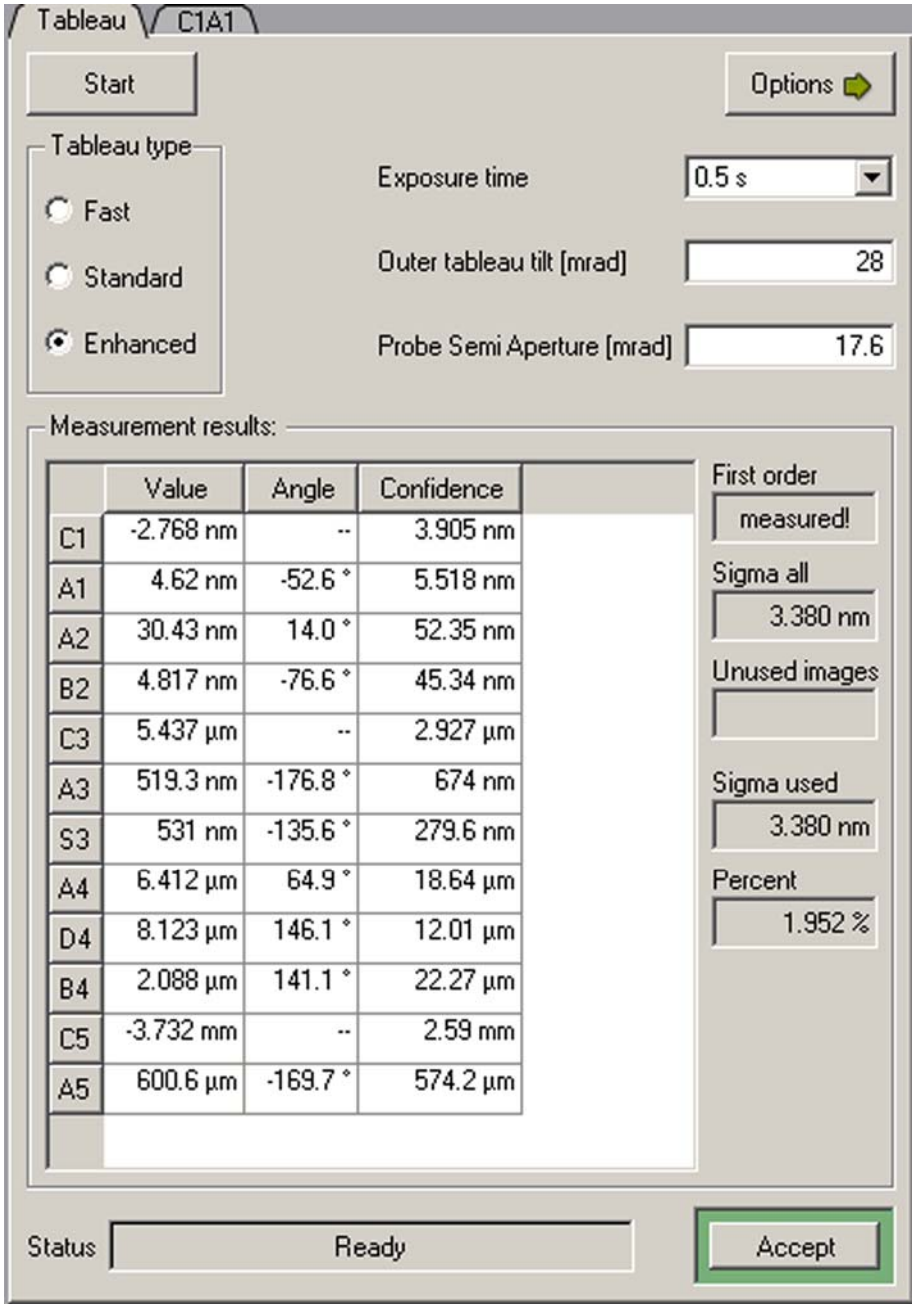

Figure 0.12: Tabulation of the aberration coefficient values obtained after complete alignment of microscope and correcting the low-order probe aberration.

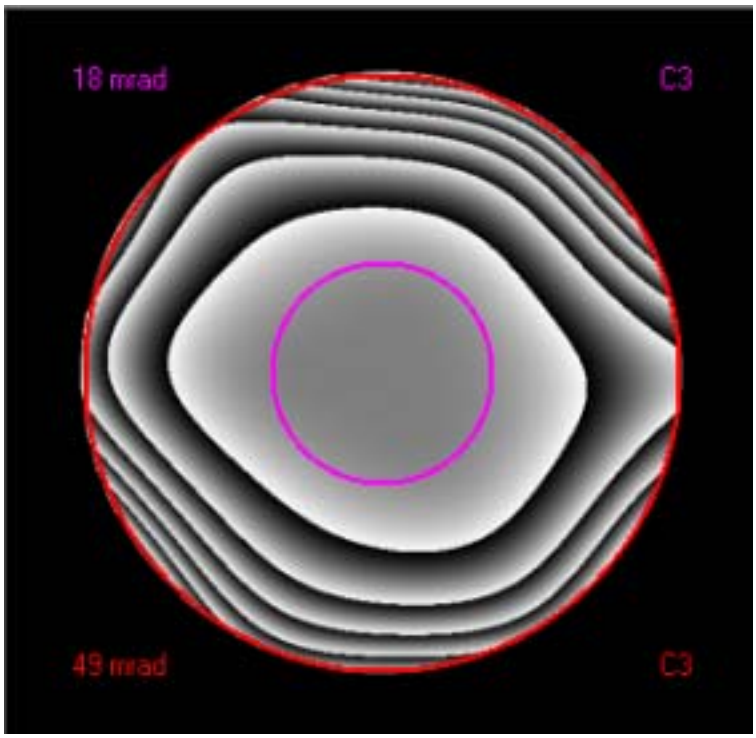

Figure 0.13: Ronchigram of corrected probe at 300 keV with convergence semi-angle of 17.6 mrad with ADF detector highlighted in pink circle.

3.2.3.2. Elemental Analysis with TEM

Elemental mapping was carried out with an energy dispersive X-ray spectrometer (EDXS) from Oxford Instrument. EDXS is based on energy transfer from incident electrons to core electrons. When a missing electron in core shell is replaced by an electron form higher orbital a photon is radiated. In EDXS the number of photons per energy window for each beam position is counted. Elemental mapping in order to understand the structure of the epilayers as well as detecting the inter-diffusion at interfaces can be carried out in STEM taking

advantage of the scanning beam with improved spatial resolution. Atomic resolution EDXS in a FEI Titan is not accessible because of limitation in collecting X-ray signals due to the geometry of objective lens pole pieces. However, the high-brightness FEG as well as sub-Å probe enables a localized chemical maps.

3.3. Multislice Image Simulation

Image simulation is an essential tool in reliable and effective interpretation of high resolution electron microscopy images. HAADF images are not sensitive to thickness changes as HRTEM images with their contrast reversal phenomenon. However, in typical thicknesses of samples multiple scattering of electron beam, due to interaction of electrons with sample and subsequent scattering more than one time, so-called dynamical scattering, leads to limitations in the direct interpretation. There are two main simulations approaches; Bloch wave and multislice. The multislice method was initially used for HRTEM images [146]. However, later it was implemented for ADF-STEM images by Kirkland [147]. In this research, the image simulations were carried out using multislice approach which can be performed in reasonable calculation times. Therefore, the simulation code implemented by Kirkland [148] and has been modified by Robertson is used to run on a parallel CPU cluster of McMaster University in significantly shorter time.

The fundamental of the multislice approach based on a two-dimensional approximation of the three-dimensional potential field of the crystal lattice. In this method, sample is divided into slices of approximately one atomic layer thickness parallel to optical axis of microscope and the projected atomic potential is calculated for each slice (Figure 3.14). The probe wave function experiences a

small phase shift due to the projected atomic potential through transmission within the slice and Fresnel diffraction when propagating the vacuum separating the slices. Then, the diffracted beam into ADF detector is incoherently integrated over annular detector and the intensity is calculated. Eventually, these calculations are iterated for each probe position.

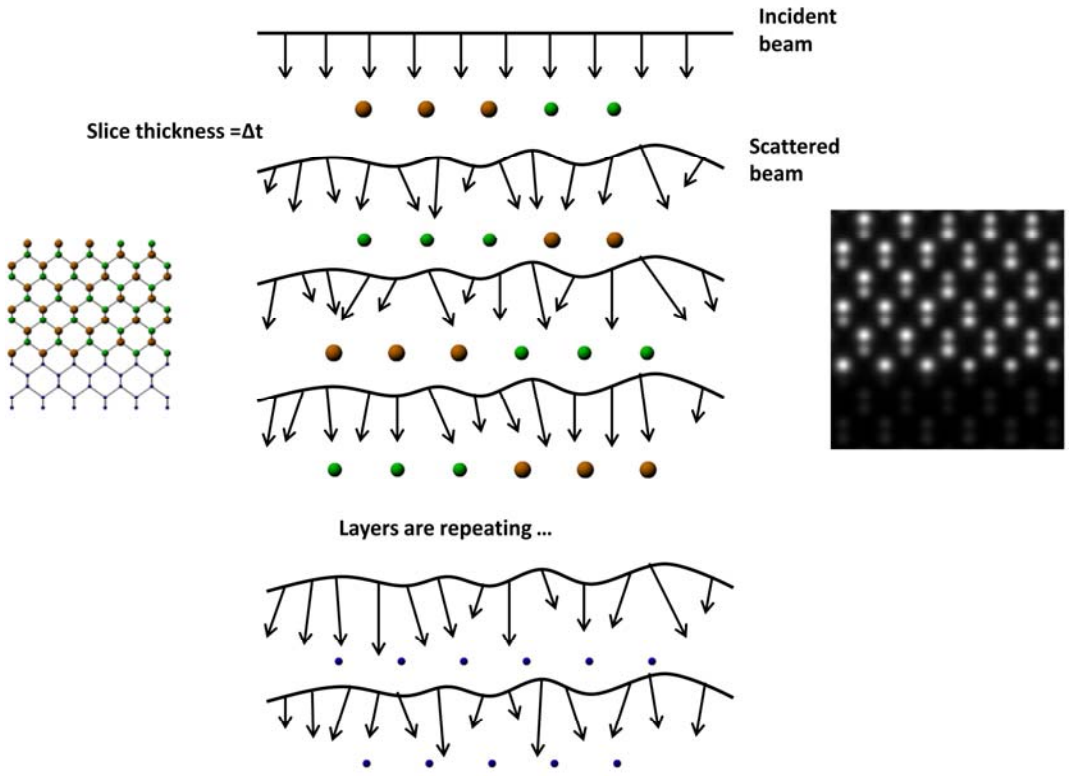

Figure 0.14: Schematic of multislice simulation.

The imaging parameters used for simulation are 2 μm for third-order astigmatism and 2 mm for fifth-order astigmatism. In order to model the source size to a first approximation, the simulated HAADF images were convolved by a

Gaussian envelope function with a FWHM of 0.03 nm, thus reducing the resultant spatial coherence.

3.4. Strain Analysis

The geometric phase analysis (GPA) [151] and peak finding procedure [152] are two main techniques used to extract quantitative information on the local atomic displacements using high resolution images. Although the HAADF images provide the necessary strong contrast, such images have not been previously used to extract quantitative information on the local atomic displacements across interfaces using the geometric phase analysis (GPA) method. The GPA method [13-16] and its variants [17] are well established for strain mapping of semiconductor thin films, and earlier work has taken advantage of the highly reproducible and nearly distortion-free HRTEM micrographs following correction through deconvolution. In these conditions, reliable GPA results are based on precise measurement of the location of the atomic columns within the films. Thanks to the dedicated environment at Canadian Centre for Electron Microscopy (CCEM) with reduced level of mechanical vibration, electromagnetic fields, and thermal fluctuations, the local strain distribution in GaSb epilayers were investigated with the GPA. The GPA method [151] is based on the concept that any lattice distortion or displacement and the corresponding strain cause a phase shift in the periodic pattern in the lattice image. Therefore, by measuring the phase changes of the lattice image, the corresponding strain and rotation can be calculated with respect to a chosen reference area in the image.

Images of a prefect crystal can be written as Fourier series of amplitude and phase. The amplitude corresponds to the contrast degree of a set of lattice fringes and phase contains the information about the lateral position of the fringes

in the lattice. The GPA is based on the Fourier filtering of the image at a strong Bragg spot. The resulting complex image has a phase component that can be used for calculating the reciprocal lattice vector. Any deviation of reciprocal lattice vector from the perfect lattice vector manifests itself as a phase change. Therefore, the phase component of the complex image gives information about the local displacement of the atomic planes. Local strain component can be calculated by analyzing the derivative of the displacement filed. The two-dimensional displacement field can be derived by choosing two non-collinear Bragg reflections. In order to analyze the strain of defects and interfaces, the HAADF-STEM images were processed with the GPA method using scripts written within the DIGITAL MICROGRAPH software package based on the work of Hÿtch *et al* [151] and implemented commercially in HREM RESEARCH™ software.

Chapter Four

Antimonide-based Heteroepitaxy

GaSb heteroepitaxial films on Si have received significant attention due to their potential applications in laser diodes and solar cells, although the lattice mismatch between Si and GaSb is a major limitation for material quality. Indeed a major determinant of film quality is expected to be the detailed strain relief mechanisms especially the type and Burgers vector of the preferred IMF dislocations and their effectiveness in accommodating strain. The presence of the misfit dislocations at the interface of GaSb and Si has previously been explored by conventional and high resolution transmission electron microscopy (HRTEM) images based on phase contrast technique [8, 19, 99, 119]. This approach is very sensitive to local variation of the sample orientation, thickness, and the defocus condition so that, qualitative interpretation and the determination of the local lattice parameter from such images are not straightforward even in aberration-corrected TEM images. Here, we report the direct observation and quantitative analysis of IMF dislocations in HAADF imaging in STEM which provides a

contrast that strongly depends on the atomic number. This approach provides direct insight on the configuration of the dislocations core and their position at the interface, yielding the most powerful approach yet to visualize and understand the strain release in lattice mismatched heterostructures.

4.1. HAADF-STEM Observations and Chemical Analysis

A HAADF-STEM image of the interface of GaSb and Si that shows strong contrast between the atomic columns in the substrate and the film is shown in Figure 4.1 (a) with its fast Fourier transform (FFT) in the inset. The silicon dumbbells (1.4Å spacing) are clearly resolved while, in the film, the image highlights the polarity of the GaSb bonds as the Sb atoms appear brighter than the Ga atoms. Multislice calculations of HAADF images of GaSb in Figure 4.2 show that the contrast between the dumbbells is reduced above a specimen thickness of 60 nm while contrast reversal due to the channeling of electron beam from adjacent atomic column is expected beyond 80 nm. Since the thickness of our TEM samples is below 30nm, we expect the polarity inference from the images to be reliable. The Burgers circuit of the IMF dislocations (Figure 4.1(b)) reveals a Burgers vector parallel to the interface. Zooming into the IMF dislocation unravels the atomic configuration of the core (Figure 4.1(c)). The atomic model reconstruction (Figure 4.1(d)) of the core structure reveals that the core is unambiguously a glide set type [42] of dislocation core consisting of a ring of eight atoms and an inner atom with dangling bonds. By inspecting the adjacent dumbbells (the first monolayer at the interface), it can be inferred that the core is an Sb column.

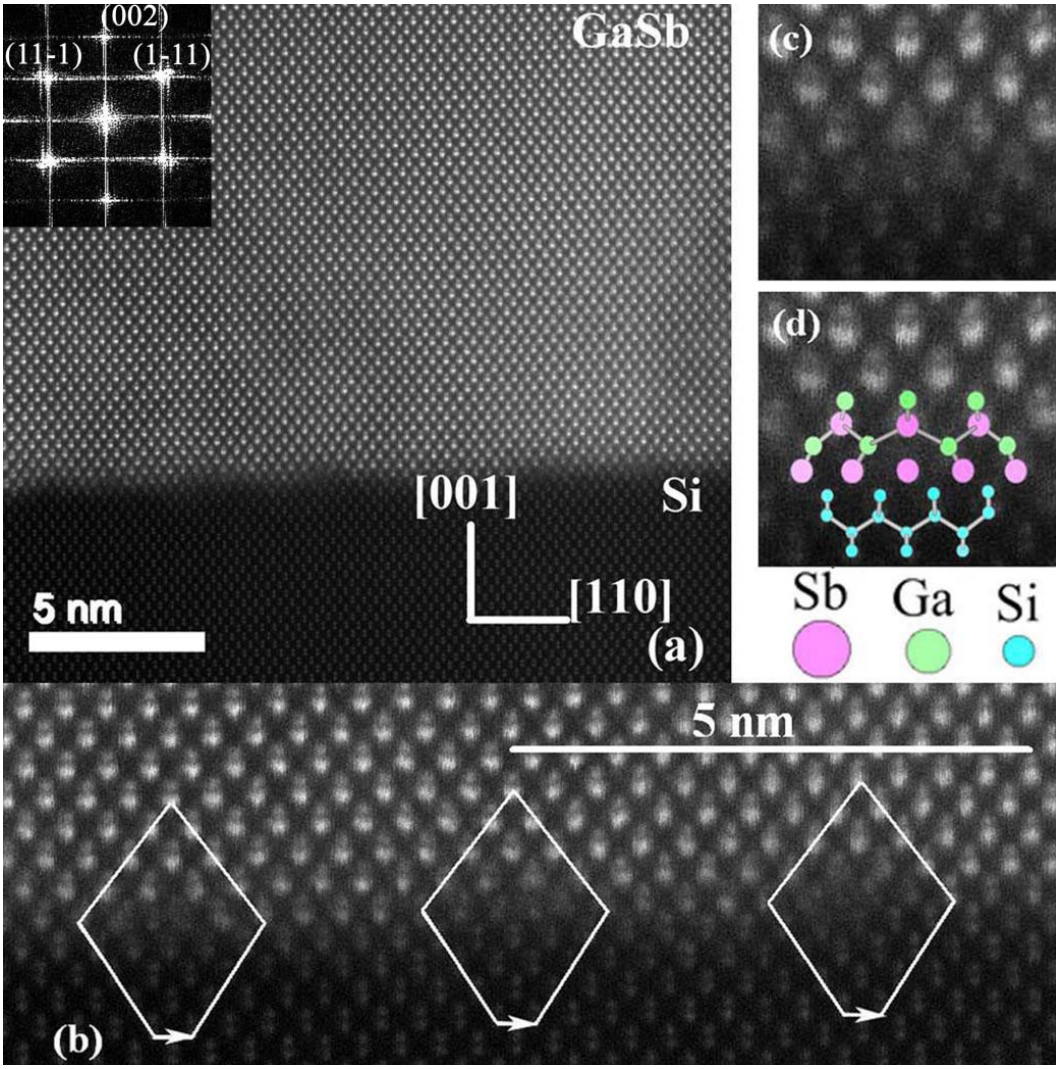

Figure 0.1: (a) Cross-sectional HAADF-STEM image of a GaSb epitaxial film on Si (un-processed images) with FFT in inset (b) A magnified image of the interface with Burgers circuits of misfit dislocations. (c) A magnified image of misfit dislocation core, and (d) the atomic model representation of the dislocation core structure.

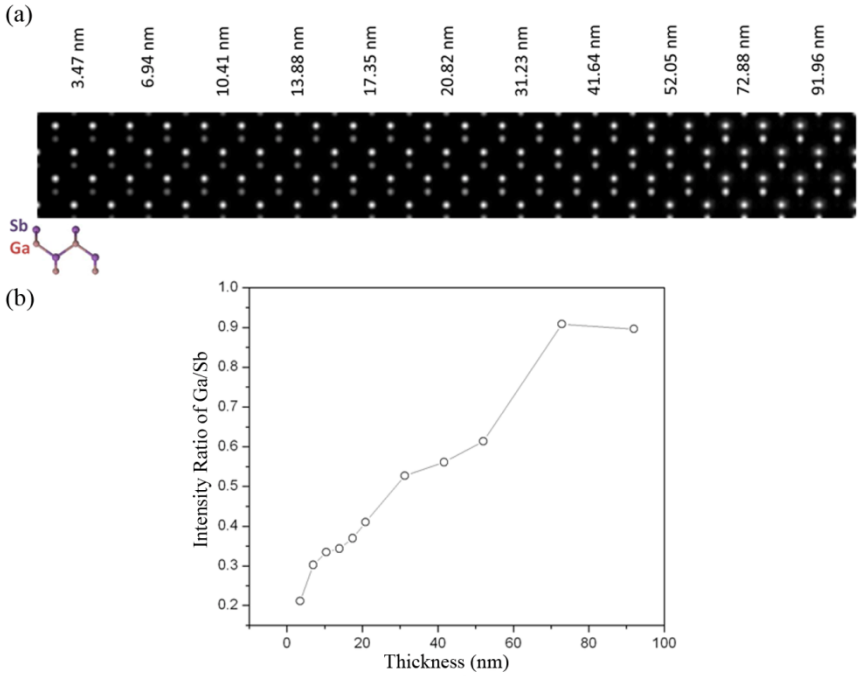

Figure 0.2: (a) Multislice HAADF-STEM simulation of GaSb in different thicknesses of sample along <110> zone axis and (b) change of intensity ratio of Ga/Sb with thickness.

From HAADF images with large fields of view, it is apparent that islands with lower HAADF signal intensity are present at the interface (Figure 4.3 (a)). From elemental mapping both with electron energy loss spectroscopy (not shown) and EDXS (Figure 4.3(b-d)) these dark features are confirmed to be AlSb islands. The islands appear as darker features in the HAADF images due to the substitution of Ga atoms with the lower atomic number Al atoms. These AlSb islands are typically 15 nm high and 35 to 50 nm wide and are bound by {111} planes resulting from 5 nm deposition of AlSb. These TEM observations, confirmed by EDXS maps, indicate explicitly that a 5 nm thick layer of AlSb

forms islands during deposition and retains the same morphology after deposition of the 500 nm thick layer of GaSb.

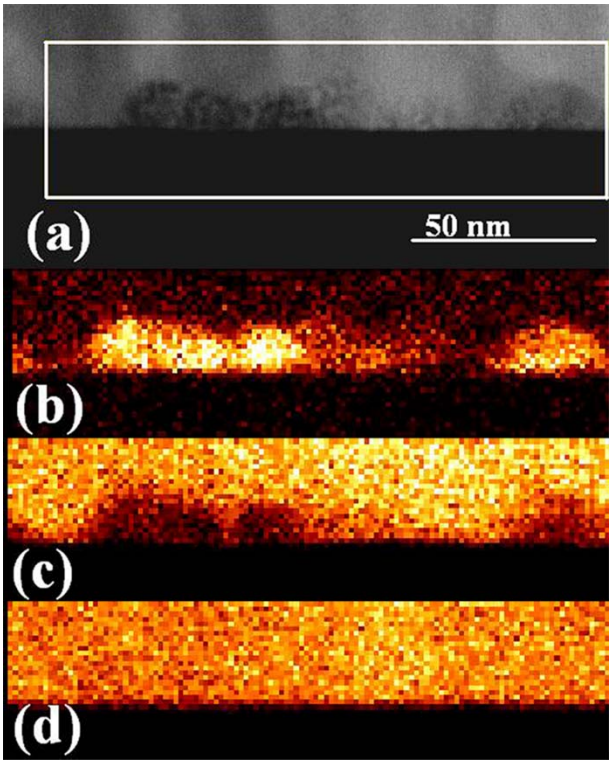

Figure 0.3: (a) A HAADF image of GaSb film with AlSb buffer on Si with the area from which EDXS mapping was carried out highlighted with a rectangle, (b) Al (c) Ga, and (d) Sb maps.

The small atomic number of Al results in not only lower HAADF signal intensity of AlSb islands but also indistinct polarity of Al atoms in AlSb dumbbells (Figure 4.4(a)). The sensitivity of ABF signal to lower atomic number elements makes the Al atoms to appear in AlSb dumbbells as it is seen in Figure 4.4(b).

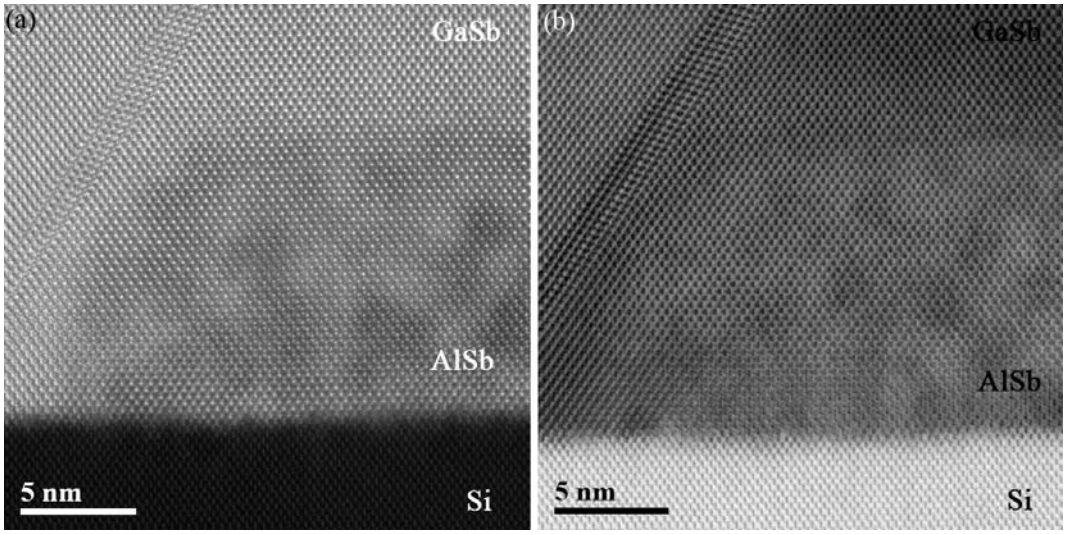

Figure 0.4: Image of GaSb film and AlSb island with (a) HAADF and (b) ABF signal.

4.2. Fourier Filtering

The periodic arrangement of the dislocations can be highlighted by Fourier filtering of (11-1) and (1-11) Bragg reflections in the inset of Figure 4.1(a). The extra (11-1) and (1-11) atomic half planes on the Si side of the interface can be observed in Figure 4.5(a) and (b) respectively. The spacing between these periodic misfit dislocations is approximately 3 nm i.e. every 9 atomic planes of Si. The two additional half {111} planes in Figure 4.5 are indicative of the presence of two 60° partial dislocations with complementary Burgers vectors [41] known to yield in a perfect Lomer dislocation with a ½ a[110] Burgers vector, perfect edge dislocations (90° dislocations). These perfect Lomer dislocations identified here are the most effective [41] misfit dislocations for relieving the strain between film and substrate and are unambiguously shown to be located at the interface in the HAADF images.

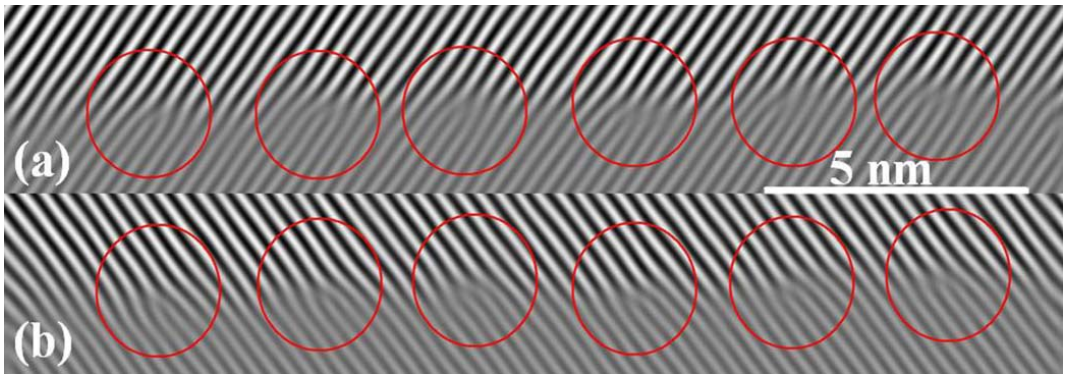

Figure 0.5: Fourier filtered images using (a) (11-1) and (b) (1-11) Bragg reflections of Fig. 1(a) displaying extra half plane of Si in circles.

4.3 Strain Analysis

The (111) lattice fringes have been analyzed using a mask size of 1.04 nm^{-1} in reciprocal space resulting in spatial resolution of 0.96 nm in the resulting images. The strain maps parallel with the interface ε_{xx} ([001] direction) (Figure 4.6(a)) and perpendicular to the interface ε_{yy} ([110] direction) (Figure 4.6(b)) obtained with the GPA show the larger lattice constant (positive apparent strain) of the GaSb film defined with respect to the Si substrate reference lattice. The strain distribution of dislocation cores (Figure 4.6(c)) shows that the Si lattice is under compression to accommodate the extra half plane while the GaSb lattice is under tension. The local measurement of strain as a function of the distance perpendicular to the interface (Figure 4.6(d)) indicates that, far from the interface, the apparent strain reaches the value of 12.2% which is consistent with the lattice mismatch between Si and GaSb and implies that the lattice parameter of the layer is completely relaxed to its bulk value within three unit cells from the interface. As is highlighted in Figure 4.6(a), the profile is extracted from the area in between

dislocation cores avoiding the scanning modulations in ε_{xx} map which is therefore similar to strain profile in ε_{yy} map. The standard deviation of strain in both film and substrate sides, at the location of the area where the profile extracted, is less than 0.4%.

AlSb (a_{AlSb}=6.1355 Å) has a large lattice mismatch of 12.9% with respect to Si and high bonding strength, therefore it tends to form islands which allow partial relaxation of the interface strain [111, 112]. In order to assess the apparent strain relaxation from the island and its proximity GPA was also carried out in the region shown in Figure 4.7(a) which has two AlSb islands 20 nm high and widths ranging from 35 to 50 nm. The GPA is shown in Figure 4.7(b) with the Si lattice again used as reference and mask size of 1.2 nm. The GPA shows a similar array of IMF dislocations both in the GaSb and AlSb regions and a local apparent strain in the AlSb island (as measured with respect to the Si lattice) of 12.9% with a standard deviation of <0.4% measured in reference lattice. Although our observations clearly show that the buffer layer forms islands, it is clear that the AlSb promotes the formation of high-quality planar fully relaxed films and the IMF dislocations are also present. The insertion of AlSb buffer promotes the planar growth of GaSb, and also facilitates the growth of GaSb with a bulk lattice parameter within a few unit cells of the interface.

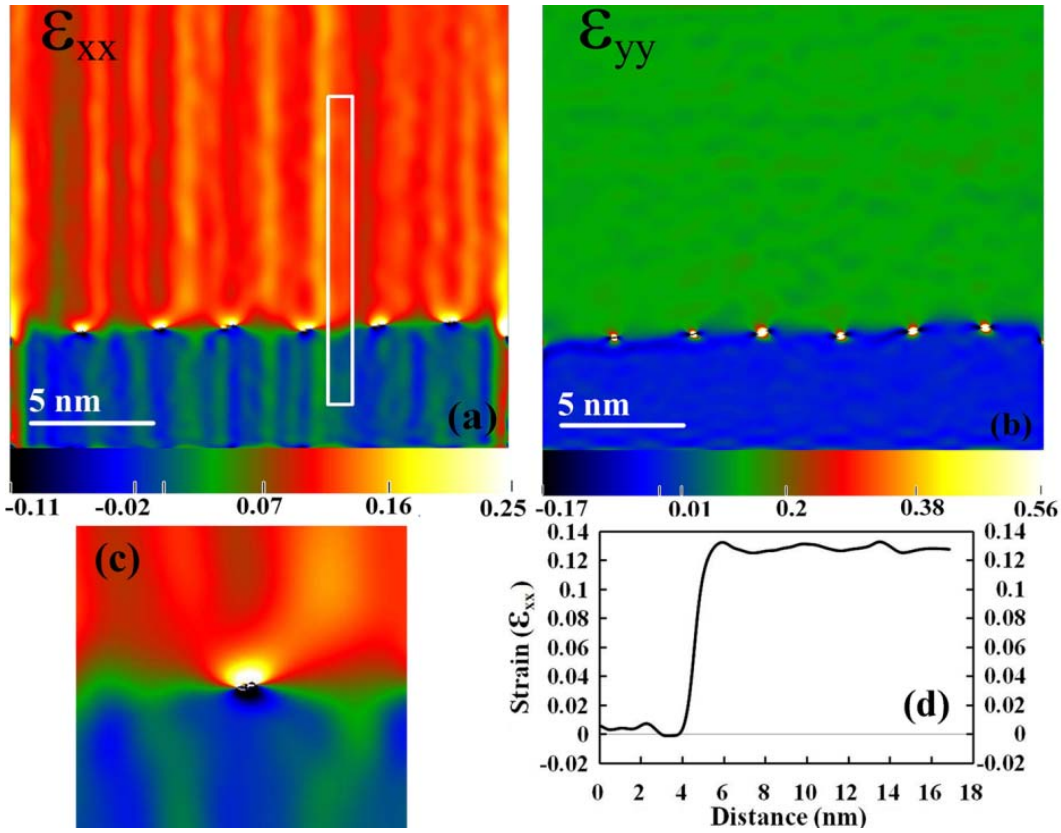

Figure 0.6 The strain map (a) parallel (ε_{xx}) with and (b) perpendicular (ε_{yy}) to the interface. (c) Strain in a dislocation core (d) line profile of the εxx strain vs. distance from highlighted area in Fig. 3 (a) (color online). The vertical modulations are the residual electron beam instabilities of the scan coils in the un-processed images.

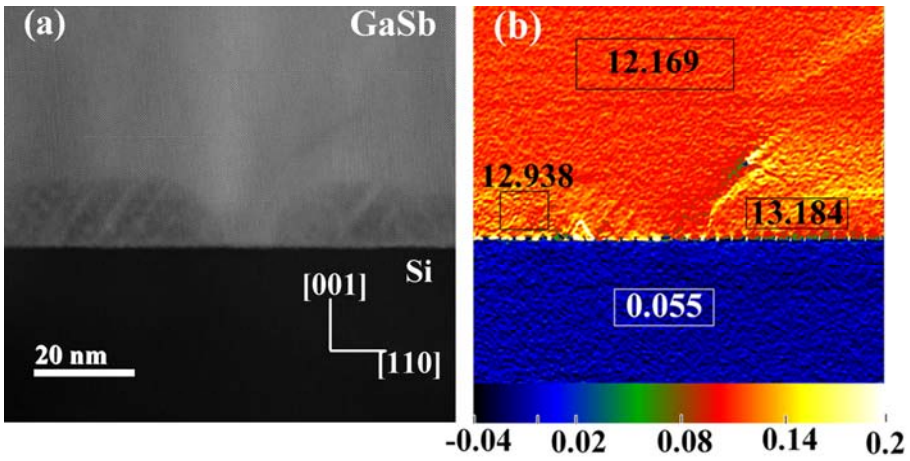

Figure 4.7: (a) A HAADF image of AlSb islands at the interface (b) Map of the strain ε_{yy} with the value of strain averaged in the rectangles highlighted in each region.

4.4 Summary

We have characterized the interface of GaSb and Si in the presence of an AlSb buffer layer. Our local measurements of strain clearly demonstrate that the presence of an array of IMF dislocations of Lomer type very effectively relaxes the lattice mismatch of system. The atomic reconstruction of the interface and dislocations core corresponding to HAADF images indicates glide-type cores for IMF dislocations. The AlSb buffer layer, generally used for promoting the growth of good quality films, has been shown to form islands along the interface and also to generate the IMF dislocations. The HAADF-STEM images together with GPA and EDXS have enabled simultaneous study of the differences in local lattice parameter due to the AlSb buffer islands as well as their chemical composition and strain field.

Chapter Five

Polarity Reversal in GaSb

The characterization of APBs is not only important to understanding the origins of the defect formation but is also relevant since APBs are electrically active defects. In fact, APBs act as non-radiative recombination centers [44, 64, 81] and as a result are the most deleterious planar defect [44] for many applications. As it was seen in previous chapter STEMs equipped with spherical aberration correctors have played a prominent role in pinpointing the atomic configuration of interfaces and defects. The contrast mechanism exploited in the high-angle annular dark-field (HAADF) technique in STEM is strongly correlated with the atomic number of the scattering atoms. HAADF-STEM is also used for direct determination of polarity for example in the wurtzite structure [153]. Hence, HAADF can unambiguously elucidate the precise configuration of APBs and their origins. This technique is therefore able to reveal the influence of the substrate surface or nucleation condition on the structure of the APBs. Therefore, imaging of APBs gained through HAADF-STEM can reveal their atomic configuration and crystallographic nature, thus providing feedback on effective

methods of suppressing the APBs. Additionally, the quality of the growth methods can be judged without misidentification of the defects [8] so that newer methods and approaches can be developed to assist in growing APB-free films. In this chapter, a detailed analysis of APB configurations in GaSb using HAADF-STEM and the possible causes of these defects are reported. Using the GPA method, quantitative measurements of the APB's strain distribution were carried out in order to eliminate any possible ambiguities regarding the structure of the APBs and determine the likely reasons for the faceting in APBs.

5.1 Conventional TEM Observations

Figure 5.1(a) shows the two-beam condition dark-field (DF) image obtained with the superlattice reflection g = 002. As the strain field of the SLS repels the dislocations and forces them to bend toward the substrate, the density of threading dislocations propagating to the film surface decreased beyond the SLS. The red arrows in Figure 5.1(a) show the area featuring an APB in the GaSb film which has initiated from the interface with Si and propagated to the epilayer surface. The APB is invisible in the bright field (BF) image with fundamental reflection g = -220 (Figure 5.1(b)) since the displacement of the APB satisfies the g.R = 0 criterion. This verifies that the observed defect is likely an APB. The polarity studies with CBED also confirmed the polarity reversal across the APB [49]. As seen in Figure 5.1(a) the majority of the facets in the APB lie on or close to {110} planes and are perpendicular to the viewing direction. However, sections of the APB with stacking-fault like fringes indicate the inclination of the boundary with respect to the transmitting electron beam. Based on formation energy calculations [60-63] the {110}-oriented APBs have the lowest formation energy and hence are expected to be the most favored type of APBs in the zinc-blende structure.

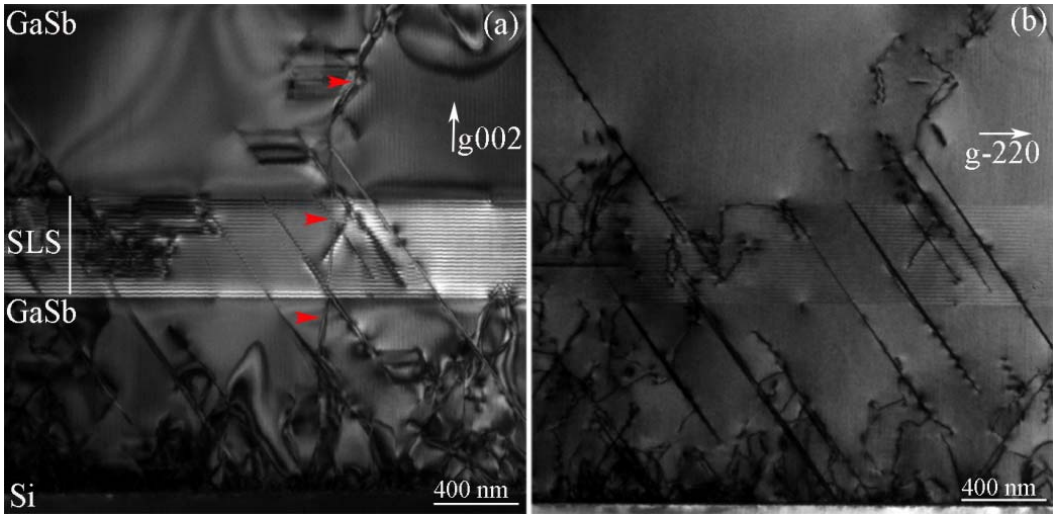

Figure 0.1: TEM two-beam images of the area featuring APBs. (a) DF image with superlattice reflection g = 002, red arrows are highlighting the APB originating from interface and propagating to epilayer surface. (b) BF image with fundamental reflection g = -220.

5.2 HAADF-STEM Observations

In HAADF imaging, the bond polarity can be identified both in GaSb and AlSb. Figure 5.2 displays the HAADF-STEM image of the interface between AlSb layer (right side) and GaSb layer (left side) in the SLS area of the heterostructure. The interface appears atomically sharp without any noticeable intermixing. There is a strong contrast between the atomic columns in the GaSb and AlSb regions. The polarity of GaSb bonds is resolved as Sb atoms appear brighter than Ga atoms according to their atomic numbers. However, the Al atoms appear as faint tails next to the Sb atoms due to the low Z number of Al. The HAADF-STEM simulations (Figure 5.2(b) and 5.2(c)) obtained with imaging conditions similar to those of the experiments confirm the main features deduced from the experimental micrographs. The polarity of GaSb and AlSb bonds in the

simulated images is consistent with the experimental image with the Sb atoms appearing brighter than the Ga atoms while the Al atoms are not discernible in the AlSb film. The HAADF-STEM simulation results (Figure 4.2) also indicated that the difference between the intensities of the Sb and Ga columns are not distinguishable in samples with thicknesses greater than 60 nm due to the strong column-to-column scattering. The Z-number dependence of the intensity in the HAADF-STEM images thus offers exquisite sensitivity to the atomic number in very thin samples.

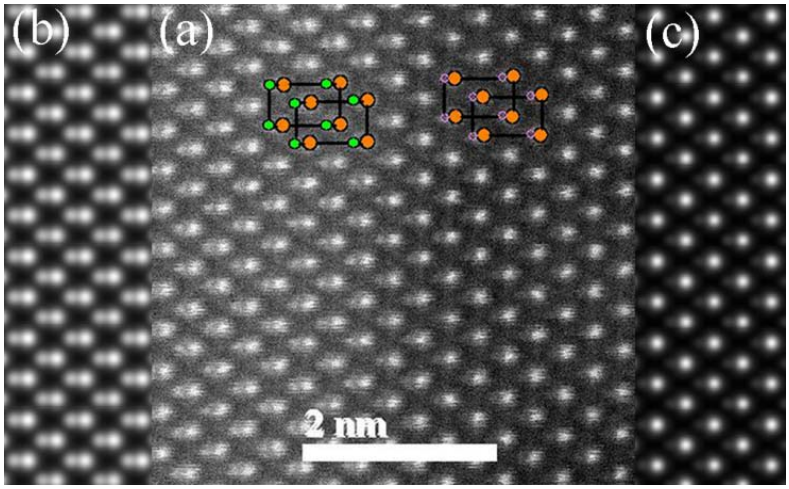

Figure 0.2: (a) Experimental HAADF-STEM image of an atomically sharp interface of the AlSb and GaSb layer in the SLS. HAADF-STEM simulation of (b) GaSb and (c) AlSb in <110> projection for a sample thickness of 20 nm, and similar microscope parameters as in experiments.

We can put to use this sensitivity to the bond polarity in the identification of APBs in the SLS. Here, the presence of APBs in the AlSb region is more easily detected due to the changes in the intensity of the Al columns. Figure 5.3(a) illustrates a polarity swap between the right and left regions of the micrograph within the APB region highlighted between the arrows. The region where the

reversal of the bonding directionality is visible in the image is much broader than the simple ball and stick model of a {110}-oriented APB (Figure 5.3(b)) and extends to a width of 3.3 nm. The Al columns in AlSb are practically not detected in the HAADF image. However, in the APB region, the intensity of the nominal Al columns increases noticeably. The increase in the intensity of the Al columns in the middle of the boundary region indicates that a fraction of Al atoms within the column is replaced by Sb atoms and that a fraction of Sb atoms is replaced by Al atoms. The width of the APB region also indicates that the APB plane is not perfectly parallel to the electron beam. In order to further confirm these assumptions, an arbitrarily chosen {310}-oriented APB is simulated with the multislice approach in the GaSb (Figure 5.3(c)) and AlSb (Figure 5.3(d)) structures. The {310} plane is perpendicular to the (001) surface but inclined with respect to the {110} planes and thus the electron beam. In the simulated images Figure 5.3(c) and (d), the atoms interchange their sites across the APB, both in the GaSb and AlSb layers. The gradual change in the intensity of the Al columns in the simulations (Figure 5.3(d)) is consistent with the experimental image and can thus be explained solely with the presence of the APB without inter-diffusion of atoms within the APB. The consistency of the simulation with our experimental images also supports the assumption that the Sb atoms have replaced Al atoms through the thickness of the TEM foil and hence that the boundary is inclined with respect to the viewing direction. It is also inferred that the APB is lying on a higher index crystallographic plane which is inclined with respect to {110} planes but prepndicular to the (001) surface.

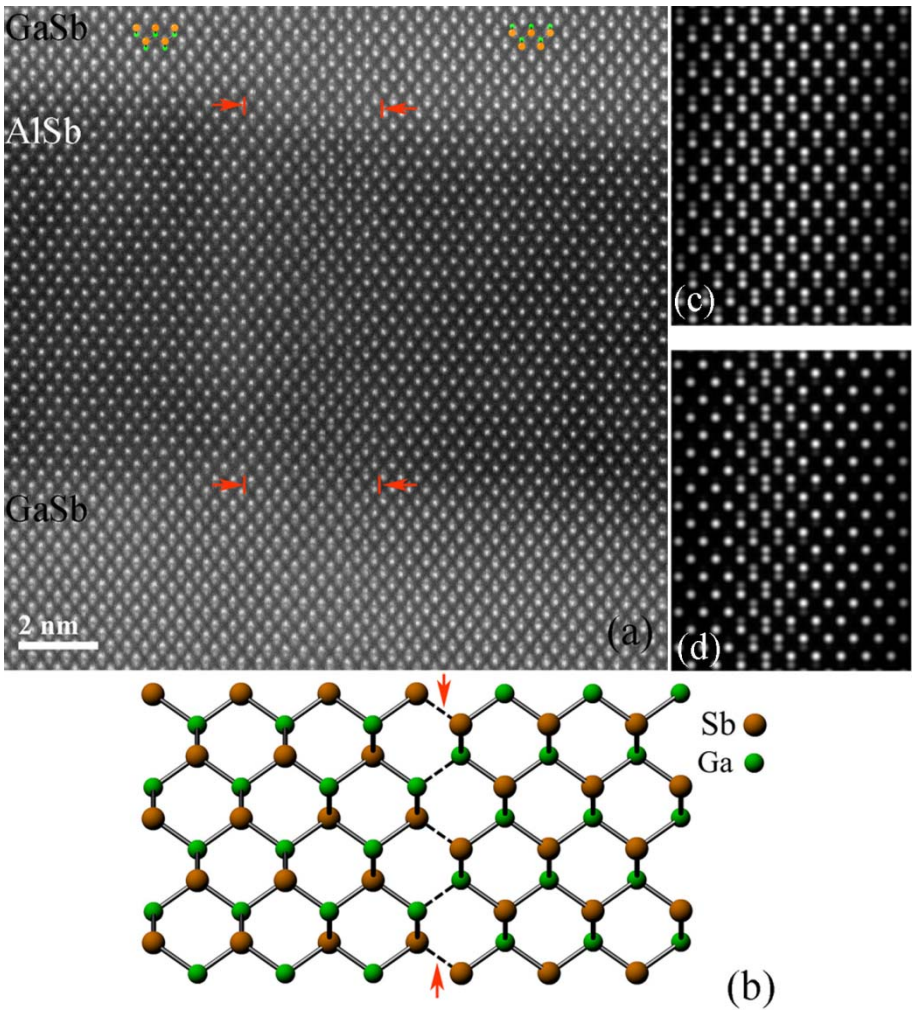

Figure 0.3: (a) HAADF-STEM image of alternating GaSb and AlSb layers in the SLS, red arrows outline an APB crossing the SLS and (b) schematic of a {110}-oriented APB, the dashed line highlights the wrong bonds between same-type atoms. Multislice simulation of an arbitrarily chosen {310}-oriented APB in (c) AlSb and (d) GaSb.

The schematic atomic model of the simulated APB (Figure 5.3(d)) is shown in Figure 5.4(a). The model demonstrates a {310}-oriented APB that propagates vertically with respect to the interface but is inclined with respect to

the viewing direction, i.e. the {110} planes. Figure 5.4(b) displays the side view (perpendicular to the electron beam direction) of the same model in which θ is the angle between the APB plane and the projection plane. The angle θ can be calculated using the thickness (t) of the sample and width (w) of the APB. The partial or complete replacement of the Al atoms with Sb atoms through the thickness of the specimen can be seen in Figure 5.4(c). The number of Al atoms that are replaced by Sb depends on the location of the intersection of the APB plane and atomic column and hence the intensity of the atomic column changes accordingly.

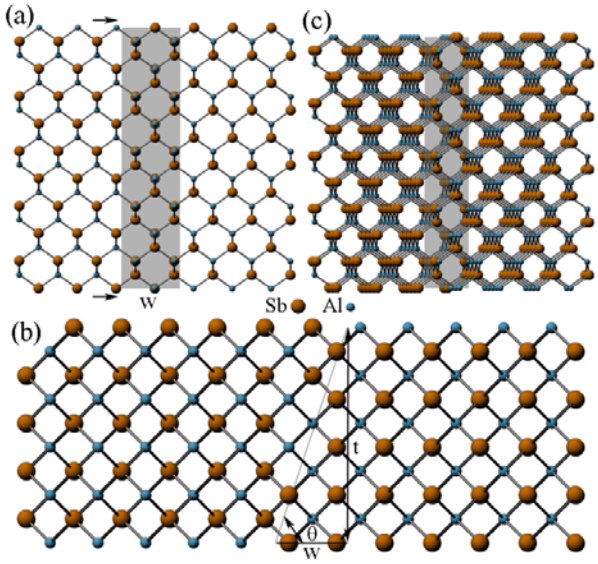

Figure 0.4: (a) Schematic projection of an arbitrarily chosen {310}-oriented APB perpendicular to {001} and inclined to [110] view direction, the arrows show the top surface of the specimen, w is the width of the ABP in projection, (b) side view of the plane in (a) along [001] view direction, **t** is the thickness of sample in the region of the APB and θ is the angle between APB and the projection plane and (c) partial or complete replacement of Al atoms with Sb atoms depending on the location of the intersection of the APB plane and Al columns.

In order to understand the origins of the formation of the APBs, we focus on the APBs at the interface between GaSb and Si. Figure 5.5(a) displays an APB

right at the interface between the Si substrate and the GaSb film which propagates into the film. In this case, the APB is a {110}-oriented boundary that originates vertically from the interface. The APB in Figure 5.5(a) appears as a line rather than a band unlike the APB in Figure 5.3(a), thus it lies parallel to the direction of the transmitting electron beam. From the change in contrast between the Ga and Sb columns, it is possible to identify the precise location of the APB and show that the boundary deviates from the initial vertical orientation at the interface to an average irrational plane. Large segments of the boundary have faceted to other crystallographic planes for lengths of few unit cells. However, segments lying on or close to {211} planes and the other {011} planes, leaning 45° from the interface normal, can be identified. The lower HAADF signal intensities apparent on the left and right sides of the HAADF image point out the presence of AlSb islands used as a buffer layer to promote a fully relaxed planar film of GaSb as pointed out in the previous chapter using energy dispersive X-ray spectrometry mapping. The other planar defect highlighted with red lines is a first-order twin with {111} habit plane lying at an angle of 54.7° from the interface. Figure 5.5(b) is the Fourier transform of the image in which the yellow and red indices belong to the epitaxial and twinned GaSb, respectively. As seen from the image, the microtwin gives rise to additional twin reflections in the form of streaks which are rotated with respect to the epitaxial GaSb. The displacement of the (001) atomic planes along the growth direction [001] can be observed by Fourier filtering using the (002) reflection. As seen in Figure 5.5(c), the (002) atomic planes are displaced half of the (002) interatomic distance along growth direction which is equal to ¼ a<001>. The detailed view of the interface region where the APB intersects the substrate further highlights the last atomic plane of Si (Figure 5.5(d) and (e)). In Figure 5.5(d) the last atomic plane of the substrate is indicated by arrows on both sides of the APB. The white lines drawn on the last atomic plane of the Si substrate show a double atomic-high step at the interface (Figure 5.5(e)).

The arrow on the left side of Figure 5.5(e) also highlights the first atomic monolayer of lower intensity than the right side of the APB which is assumed to be Ga-prelayer domain.

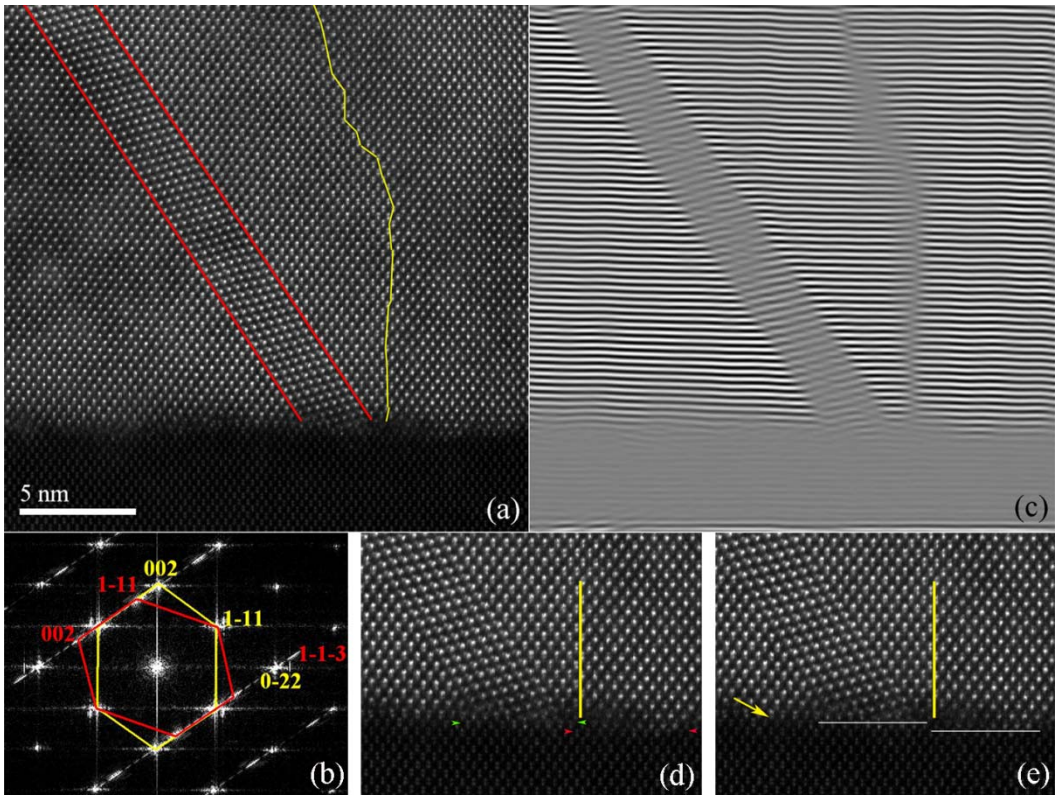

Figure 0.5: (a)The HAADF-STEM image of GaSb-Si interface with an APB (outlined with yellow line), (b) Fourier transform of the image, red and yellow indices show the Bragg reflections of the twinned and epitaxial GaSb, (c) the Fourier filtered image of (a) using the (002) reflection. The ¼ a<001> displacement along the growth direction is distinguishable at the APB, (d) the magnified image of interface at the APB in (a) with arrows displaying the last atomic plane of Si and (e) the white lines are drawn on the last atomic plane of Si on either side of the boundary to show the double atomic high step at surface. The arrow highlights a domain starting with Ga-prelayer.

To avoid the possible misinterpretation of the intensities in an image of the interface due to the channeling effect of the electron beam, multislice simulations were carried out on the structure shown in Figure 5.6(a). Figure 5.6(a) is a ball and stick structural model of an APB resulting from the coalescence of a Ga-prelayer domain (left side) and a Sb-prelayer domain (right side) originating from mixed nucleation on the surface of a flat (001) Si substrate. Two dangling bonds of the surface-layer Si atoms are oriented perpendicular to the interface between Si and GaSb which is the more energetically favorable configuration when a double step exists on a Si surface [24]. On the other hand, in this configuration of the interface layer, the left and right sides are comprised of Ga-Si and Sb-Si dumbbells, respectively. Since the mixed dumbbells adjacent to the interface are the closest species, we have to consider the possible channeling from the Sb/Ga column to the Si column and back to the Ga/Sb column and the effect of the mixed pair on interpretation of the image intensity of the individual columns. The multislice HAADF-STEM simulations of the model with a sample thickness of 20 nm (Figure 5.6(b)) indicate that the intensity of the Ga column in the Ga-Si pair and the intensity of the Sb column in the Sb-Si pair are distinguishable. The intensity profiles of the left (Figure 5.6(c)) and right (Figure 5.6(d)) sides of the APB clearly demonstrate that the intensity of an Sb atom in an Sb-Si pair is approximately similar to the intensity of an Sb atom in a Ga-Sb dumbbell and furthermore that the Sb atom at the first monolayer is noticeably brighter than the Ga atom in the first monolayer. This observation implies that the intensity of HAADF-STEM images with a specimen thickness 20 nm and below can be interpreted reliably.

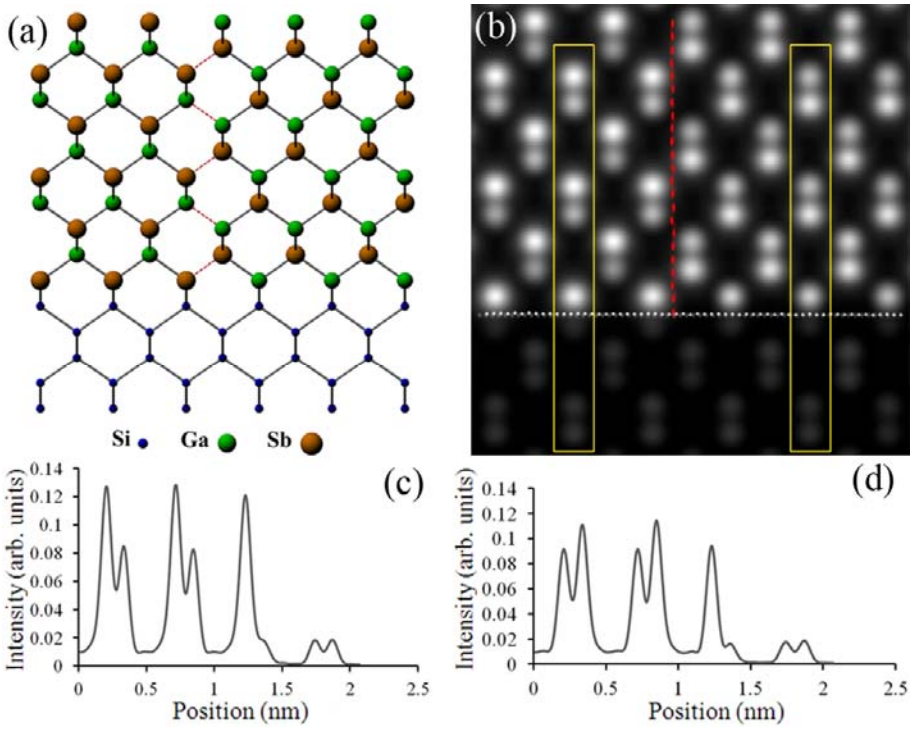

Figure 0.6: (a) The ball and stick model of a {110}-oriented APB marked by red dashed line and (b) Multislice HAADF-STEM simulation of the superlattice in (a) for a specimen thickness 20 nm. Intensity profile of (c) left side and (d) right side of the APB boxed in yellow. The GaSb and Si interface is highlighted by white dotted line.

Additional observation confirming the ambiguous nucleation of GaSb on Si(001) substrate is displayed in Figure 5.7(a). The reversal in extracted intensity profile of the GaSb dumbbells within adjacent atomic columns (shown in boxed regions in red and green, and pink and blue) at both sides of APB highlighted in yellow is indicating that bonding directionality is swapped. The evaluation of atomic species at the interface shows that the first atomic mono-layer switched from Ga-atom (Figure 5.7(b)) on the left to Sb-atom (Figure 5.7(c)) on the right.

Additionally, the GaSb/Si interface (dashed line) in Figure 5.7(a) confirms the mixed domain nucleation within one terrace, further.

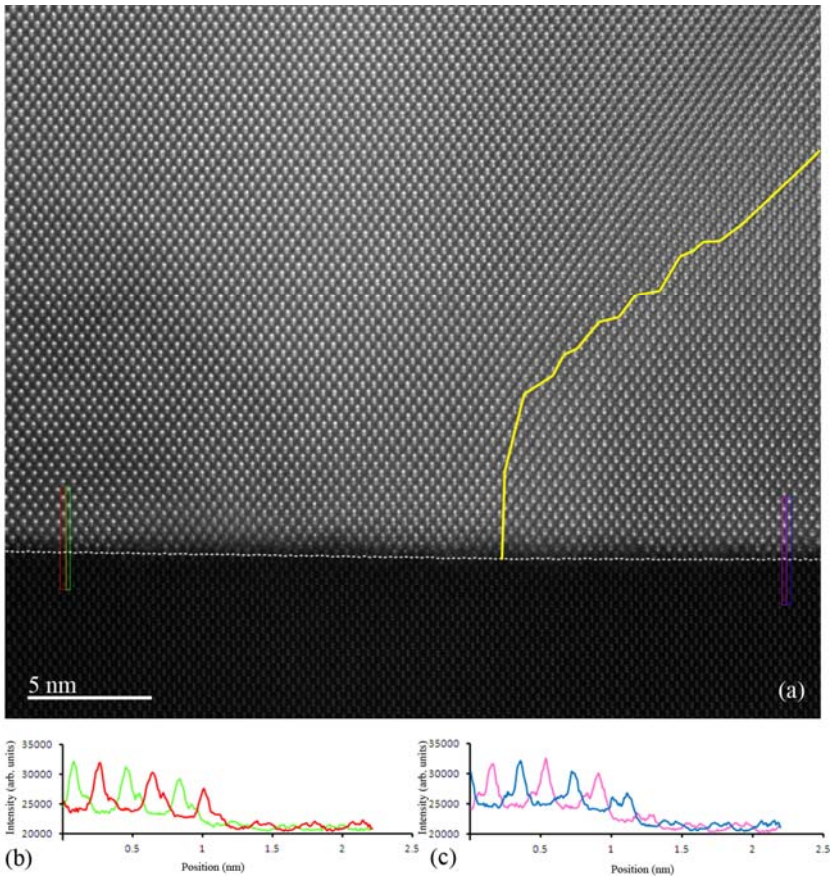

Figure 0.7: a) Cross-sectional HAADF-STEM image of the interface of GaSb epilayers on nominal Si(001) with an APB outlined in yellow. The intensity profiles of the adjacent atomic columns on the (b) left (boxed in red and green) and (c) right (boxed in pink and blue) side of the APB are shown in the orientation as indicated by the arrow. The last atomic plane of Si, denoting the GaSb/Si interface is visibly marked by a dashed line.

It is common for APBs to form on some low-index crystallographic planes such as {110}, {211} and {111}. However, our observations using HAADF-STEM technique shows that APBs can lie on a variety of crystallographic planes such as some uncommon high index crystallographic planes (Figure 5.3(a)). Large segments of {110}- and {211}-oriented APB planes in Figure 5.5(a) and Figure 5.7(a) display the preferential origination of the APBs on stoichiometric planes and retain their stoichiometric characteristics by faceting accordingly due to energetics and interface neutrality considerations [60-63]. However, if there is any change in the intrinsically stoichiometric growth conditions of the MBE such that it deviates from stoichiometry, we can expect it will induce APBs of the non-stoichiometric type, such as {111} planes.

The domain with a Ga-prelayer in Figure 5.5(d) and Figure 5.7(a) unambiguously indicates that mixed domain nucleation has induced the APB. This phenomenon implies that the initiation of growth with Sb-prelayer soaking cannot guarantee that Sb will overlay on the Si substrate as the first atomic layer. Unlike GaAs/Si where As soaking can prevent mixed nucleation [154], in GaSb growth the low sticking coefficient of Sb to Si can cause Ga-prelayer and Sb-prelayer domain formation [155, 156]. The ball and stick model in Figure 5.8 shows that in spite of the presence of the double atomic high step, the sequence of the Sb and Ga layers on the either side of the step will not change. However, on the left side of Figure 5.8 we introduced an APB forming due to the coalescence of the domain started with Sb as the first monolayer with the Ga-prelayer domain. In the model, the starting point of the Ga-prelayer domain does not coincide with the double step to reduce the complexity of the model.

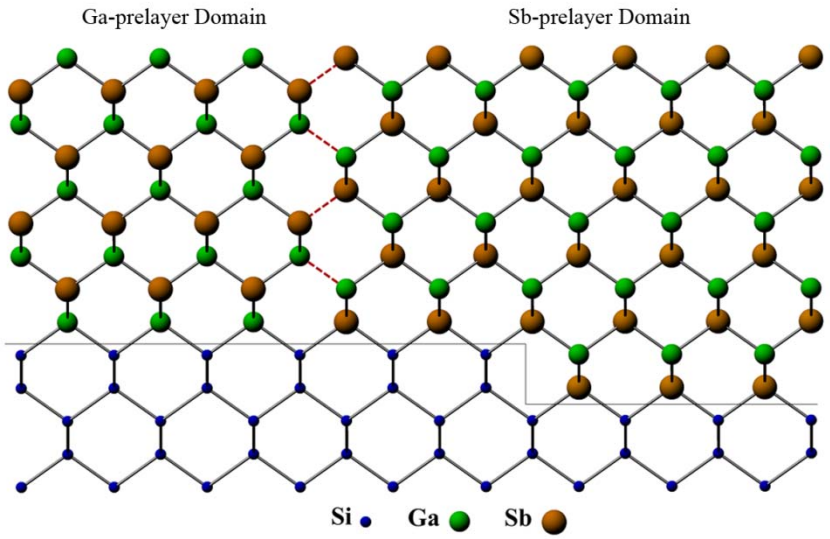

Figure 0.8: Schematic model of a double atomic high step at the Si substrate showing the formation of an APB due to the coalescence of anti-phase domains with Sb and Ga as their first monolayer. The dashed lines display the wrong bonds along the APB.

5.3 Strain Analysis

The Bragg reflections $g_1 = 200$ and $g_2 = -220$ in the Fourier transform of the image in Figure 5.5(a) were analyzed using a Gaussian mask with the size of 1.09 nm^{-1} in reciprocal space resulting in 1/1.09 = 0.91 nm spatial resolution. From the resulting phase image (Figure 5.9(a)) it is clear that the phase of the two adjacent domains shifted from 0 to π (or $-\pi$) due to the half inter-planar spacing displacement of the atoms across the APB. The π phase shift in Figure 5.9(a) is consistent with the polarity reversal characteristic of the APBs. Figure 5.9(b) and (c) display the in-plane strain fields ε_{xx} and ε_{yy}, respectively, derived from GPA. The strain maps in Figure 5.9(b) and (c) show the smaller lattice constant of the Si substrate (negative apparent strain) defined with respect to the reference lattice of

the GaSb film. The visibility of the APB is more pronounced in the ε_{yy} map (Figure 5.9(c)) as a result of the larger strain component along y (growth direction) than along x (parallel to interface). It is also apparent that the strain is larger in the curved segment of the APB than the edge-on segment. The strain field of the twin adjacent to the APB is apparent as well. The measurement of the local apparent strain in the ε_{xx} map indicates that there is a 4% strain between Si and the twinned GaSb. This strain corresponds to the mismatch between {113} planes of the twinned GaSb and {022} planes of the Si substrate which were included inside the mask used for calculating of the phase images. In Figure 5.9(d) the in-plane rotation matrix of Figure 5.9(a) is shown in which the positive and the negative angles correspond to counter-clockwise and clockwise rotations of the lattice, respectively.

To study the strain distribution of the interfacial misfit dislocations, the (-111) and (1-11) Bragg reflections were evaluated with the GPA method (Figure 5.10(a)). The positive apparent strain of GaSb film is indicative of its larger lattice constant with respect to the Si substrate reference lattice. The black arrows on the image show the core of the misfit dislocations with spacing smaller than the 90° Lomer dislocations in the GaSb/Si heterostructure that was seen in previous chapter. The rotation of the twinned GaSb lattice with respect to the epitaxial GaSb and the Si substrate can also be seen in Figure 5.10(b).

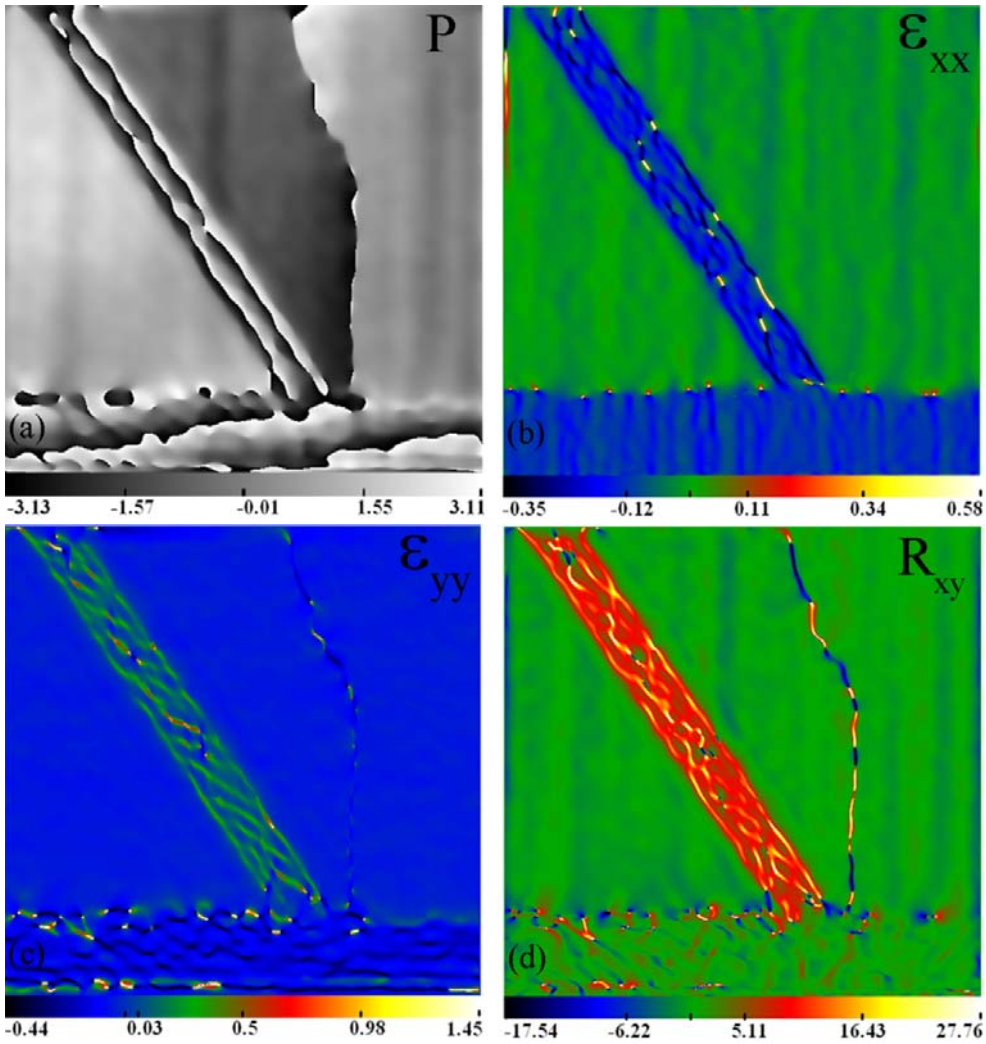

Figure 0.9: (a) Phase image of Bragg reflection (002). The strain map (b) parallel (ε_{xx}) with and (c) perpendicular (ε_{yy}) to the interface, and (d) the rotation matrix (R_{xy}). GaSb lattice is used as the reference lattice.

This strain and lattice rotation caused by the APB in Figure 5.5(c) and (d) can be attributed to the different bond length of the anti-phase bonds compared to the in-phase bonds. The higher strain in the curved segment of the APB may be due to the unequal number of wrong bonds forming the APB. The strain of the

lattice due to the presence of an APB relaxes and causes the adjacent atomic bond to shrink or stretch in order to accommodate the strain from the wrong bonds and hence results in a rotation of the lattice. The ball and stick model in Figure 5.11 illustrates the influence of the bond length on the rotation of the lattice due to the change in the wrong bonds lengths (Ga-Ga = 252 pm, Sb-Sb = 272 pm [58]) compared to the correct bond length (Ga-Sb = 262 pm). As pointed out by the arrows, the rotation direction of the bonds is induced by the change in the length of the Ga-Ga and Sb-Sb wrong bonds. When these clockwise and counter-clockwise rotations are unbalanced, there is a net rotation of the APB. The APB maintains its normal direction by counterbalancing the rotation; consequently the rotation direction is reversed for two consecutive sections of the APB (Figure 5.5(d)). This change in the rotation direction may also be due to the local excess or deficit of Ga or Sb that make the small segments of {111}-oriented APBs favorable, similar to what Vanderbilt *et al.* [61] proposed based on their theoretical calculations.

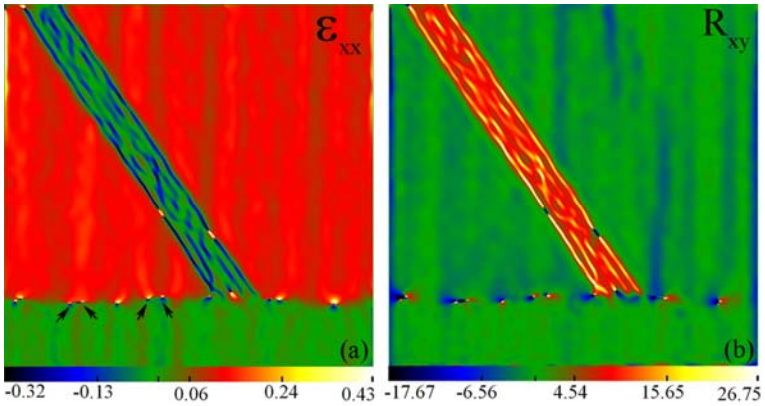

Figure 0.10: (a) Strain map ε_{xx} along the interface and (b) Rotation map R_{xy}. Si lattice is used as a reference lattice.

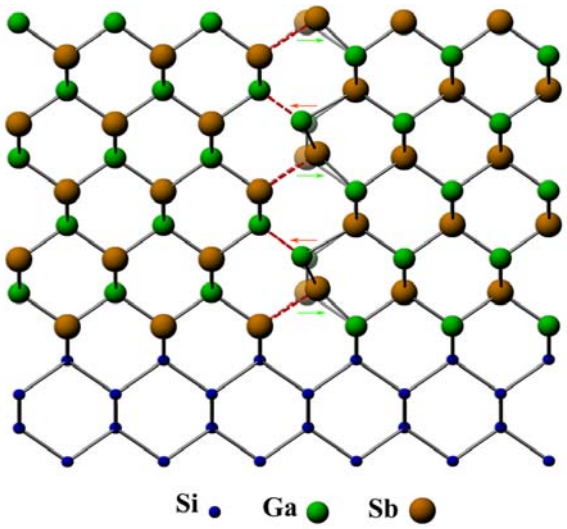

Figure 0.11: Schematic of atomic bond distortion along the APB and the induced lattice rotations. The arrows show the rotation direction of the atomic bonds.

Our observations reveal that all of the APBs in GaSb have initiated normal to the substrate regardless of whether they propagate to the film surface or annihilate within the film. However they often facet to the other crystallographic planes and change their lateral positions. Sometimes two APBs with reversed kinking directions annihilate each other. It is believed that this faceting is due to local relaxation and lattice rotation to accommodate the change in bond length in addition to interfacial energy considerations. The proposed mechanism of the self-annihilation supports the theoretical work by Vanderbilt *et al.* [61] and suggests a possible reason for the kinking which was unclear in their work. The scarcity of the self-annihilated APBs on the flat substrate is the result of the larger step spacing of the substrate compared to offcut substrates. Because of this, the density of the self-annihilated APBs in the GaSb film grown on an offcut substrate is significantly higher than that on the flat substrate [155]. The number of closed-loop APBs may also increase by increasing the growth thickness.

It is clear from the strain map parallel to the interface (ε_{xx}) in Figure 5.10(a) that the strain in the GaSb film has relaxed to its bulk value of 12%. The strain distribution of the dislocation cores shows that the GaSb lattice is under tension to accommodate the extra atomic half plane in the Si lattice. The dislocation core shown by the arrows belongs to two pairs of 60° dislocations on the distinct {111} planes that were not able to react to the 90° dislocations. The 60° dislocations are not as efficient as the 90° dislocations in accommodating the lattice mismatch. The rotation angle of the twin region corresponds to the first-order twining operation (the rotation of the {111} planes around the <110> foil normal).

5.4 APBs and Twins Interaction

Based on the visibility of the APB in HAADF images and the reversal of the polarity of dumbbells, we can now demonstrate how APBs interact with other defects in thin films. Figure 5.12(a) and (b) illustrate the interactions of the APB, highlighted with a yellow line, with a nano-twin. In Figure 5.12(a) the APB prevents the propagation of the nano-twin (4 atomic planes wide) and thus terminates the twin. However, in Figure 5.12(b), the APB (entering from the highlighted region in Figure 5.12(c)) is bent by the twin (displayed in Figure 5.12(d)), propagates some distance along the twin, and eventually exits from it (shown in Figure 5.12(e)). The reversal of Ga-Sb dumbbells' direction across the APB path in Figure 5.12(d) is visible. Because of the interaction between the twin and the APB, the position of the SLS interfaces changes (Figure 5.12(b)) indicating that the growth rate is affected not only by the twin as reported in [9] but also by the APB. The annihilation of the twin boundary after the interaction with an APB has been attributed to the presence of a kinetic barrier [92] and a larger amount of disorder caused by the APB [94].

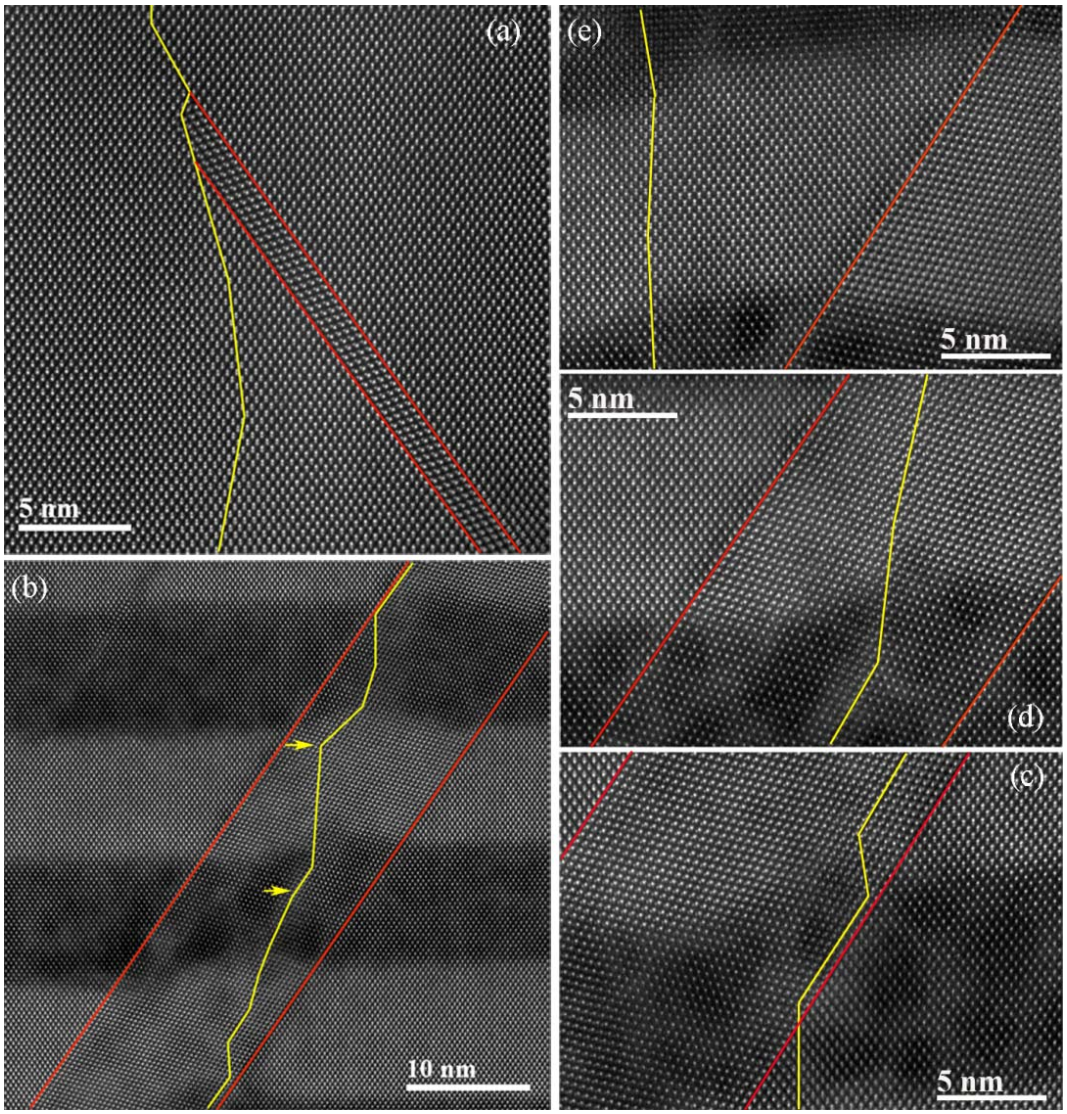

Figure 0.12: APB and twin boundary intersections are outlined with yellow and red lines, respectively. (a) Twin blockage and APB propagation and (b) propagation of both APB and twin. The APB in (b) is shown in (c) entering into the twin region, (d) bent by the twin, and (e) exiting from the twin region, section (d) is the magnified image of part of the APB highlighted with yellow arrows in (b), while sections (c) and (e) are magnified images of the sample shown in (b) from regions below and above, respectively.

5.4 Summary

We have demonstrated the atomic resolved configuration of APBs in GaSb grown on Si and their resultant polarity reversal. The direct detection of the presence of APBs from the HAADF-STEM micrographs avoids tedious polarity studies and allows very direct studies of the origin of the APBs and their interaction with other defects. The results presented show that the orientation of the APBs can be intuitively inferred from the Z-contrast images. The extracted phase images through GPA image processing illustrate the phase change across the APBs. The local measurements of the strain at the interface of domains with reversed polarity have revealed the strain induced by the incongruous bond length of the wrong bonds. Compensating the lattice rotation by lateral shifting and faceting plays an important role in the self-annihilation of the APBs. The prelayer soaking step plays a crucial role in the formation of the APBs. In order to reduce the formation of the APBs, precise control of the substrate offcut as well as the growth recipe should be implemented simultaneously. The interaction of the APB and the twin boundaries can manifest distinct consequences.

Chapter Six

Heteroepitaxy of GaSb on Si (211)

It is observed that the high lattice mismatch of GaSb grown epitaxially on Si (12.2%) is relieved through interfacial misfit dislocations with optimized growth procedures. However, the GaSb/Si(001) interface can still be influenced by the formation of anti-phase boundaries (APBs) due to the reversal of Ga and Sb sublattices in the zinc-blende structure of GaSb. Incongruous nucleation of domains of reverse polarity results in the formation of APBs. This is due to the low affinity of Sb atoms to the Si substrate which causes the reversal of the atomic prelayer at the interface regardless of the species used in exclusive prelayer soaking techniques [155, 156]. Therefore, the approach of mitigating the formation of APBs induced by single atomic high steps in GaSb/Si through using off-cut Si substrates is not as successful as in GaAs/Ge due to the weak sticking coefficient of Sb-atoms. Moreover, it has been shown that in most of the common crystallographic orientations of Si substrates, there is an accumulation of charge at the interface due to the abrupt change in the nature of the structure, from diamond to zinc-blende. This charge imbalance is partially reduced by the interface

reconstruction which induces defects [157-161]. Si(211) is one of the orientations that satisfies the required crystallographic condition for interface neutrality [158, 160, 161].

Si(211) as a high-index crystallographic plane has been conventionally used for epitaxial growth of II-VI compound semiconductors. Superior quality CdTe, ZnTe, and CdZnTe films grown on Si(211), as compared to the other orientations, makes these films appropriate buffers for the subsequent growth of HgCdTe [162, 163]. Step arrays on the Si(211) surface promote step flow growth by providing nucleation sites at the step edges and limiting the migration of the adatoms. This step flow growth mode can be enhanced by As passivation which results in the reduction of twins [163-165]. Additionally, using vicinal Si(211) [162, 164] or thin ZnTe buffer layers on nominal Si(211) [165-169] improves the quality of CdTe epilayers on Si(211) by suppressing the twinning and misorientation between the epilayer and the substrate.

Wright et al. [158] initially suggested the use of other Si substrate orientations rather than the widely used Si(001) orientation for growth of III–V compound semiconductors. Based on theoretical considerations, they showed that the Si(211) surface can overcome problems of accumulated charge at the interface and ambiguous nucleation due to the sublattice reversal. They also experimentally observed that appropriate site allocation in GaP/Si(211) is achieved by preferential bonding of Ga and P atoms to two distinct sites available on the Si(211) surface [158-160]. However, the effect of the Si(211) orientation on the suppression of APBs and film quality in the growth of III-V compound semiconductors has been limited to the earlier works of Wright et al. on GaP/Si and Uppal et al. on GaAs/Si, studied with conventional transmission electron microscopy (TEM) techniques and chemical etching.

In this chapter, we report the direct observation of the individual atomic columns at the interface of GaSb epilayers on Si(211) substrates utilizing HAADF-STEM. The use of atomic resolution HAADF-STEM in a spherical aberration-corrected electron microscope capable of forming a sub-Ångstrom electron probe provides an intuitive interpretation of the contrast in the acquired image of the atomic configurations and bonds at the interface. This direct insight combined with relative strain mapping across interfaces using geometric phase analysis (GPA) elucidates the strain relief mechanism in lattice-mismatched GaSb/Si(211) heterostructures.

6.1 Conventional TEM Observations

Conventional TEM evaluations of cross-sectional specimens indicate that the grown film consists primarily of alternating bands of micro-twins and epitaxial regions which are seen in the two-beam condition bright-field image along the [01-1] viewing direction with g=200 (Figure 6.1(a)). However, in the orthogonal viewing direction, along [-111], twins and epitaxial regions appear as stripes lying almost parallel to the interface (Figure 6.1(b)) since the bands of twins and epitaxial regions are cut perpendicular to the interface. Although few stacking faults and threading dislocations are observed in the [-111]-view TEM specimen, the overall quality of the GaSb epilayer grown on Si(211) is improved with respect to GaSb films grown on Si(001). The pole figures [170] obtained from Two-Dimensional X-ray Diffraction (2DXRD) data reveal that the GaSb epilayer exhibits a dominant [211]-orientation, as well as major first order twins about ⟨111⟩. These first order twins produce [552]-oriented normal variants. Moreover, GaSb films also contain some second order twins due to the twinning of {552} planes about {111} which are visible and highlighted by red arrows in the TEM micrograph of Figure 6.1(a).

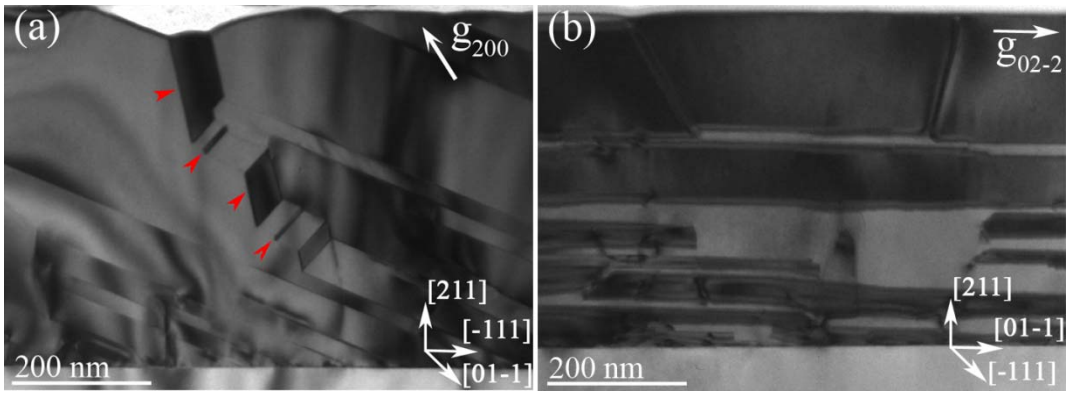

Figure 0.1: (a) Two-beam bright field image of the [01-1]-zone axis with g=200 and (b) two-beam bright field image of the [-111]-zone axis with g=02-2.

6.2 HAADF-STEM Observations and Chemical Analysis

From HAADF-STEM images with a large field of view, islands featuring lower HAADF signal intensities are apparent at the interface (Figure 6.2(a) and (d)). Using elemental mapping with energy dispersive spectrometry (EDXS), these are confirmed to be AlSb islands (Figure 6.2(b)) beneath a GaSb film (Figure 6.2(c)). AlSb islands appear darker due to the lower atomic number of Al as compared to Ga. In Chapter Four, we showed that a 5 nm deposition of AlSb on Si(001) substrate also results in the formation of AlSb islands. However, AlSb islands on the Si(211) surface have asymmetric morphology when viewing along the [01-1] zone axis (Figure 6.2(a)) due to the intrinsic asymmetry of the Si substrate. Moreover, unlike to the AlS islands on Si(001), these AlSb islands are bound by {111} planes (along the longer edge) which lie 22° from the interface (19.47° + 2.5° tilt) and by {101} planes (along the shorter edge) lying 76° from interface (73.22° + 2.5° tilt).

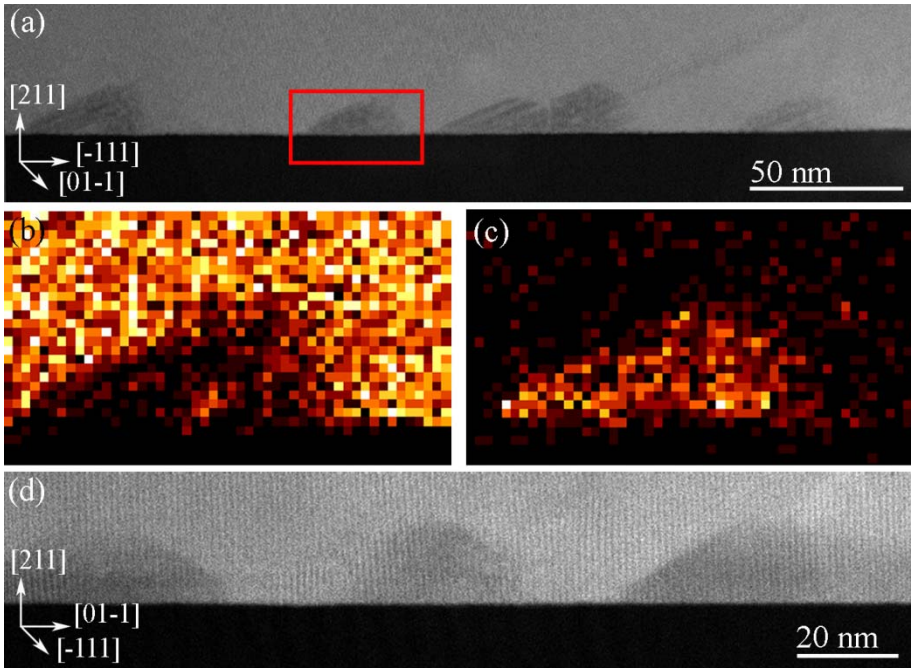

Figure 0.2: (a) HAADF image of GaSb film with AlSb buffer on Si(211) along [01-1] zone axis and EDXS mapping on one of the AlSb islands highlighted by red rectangle in (a) displaying, (b) Ga map, (c) Al map, and (d) HAADF image of GaSb film with AlSb buffer on Si(211) along [-111] zone axis.

In order to understand the GaSb epilayer structure and verify the misorientation observed in the low-resolution image of Figure 6.1, atomic-resolved images of the specimens were acquired. The HAADF-STEM image of [-111]-view specimen (Figure 6.3(a)) displays multiple atomic-resolved and unresolved bands corresponding to the epitaxial and twinned stripes observed in Figure 6.1(b), respectively. The atomic pattern of the zinc-blende structure along the [-111] viewing direction is well resolved in the epitaxial regions. However, the twinned stripes appear fuzzy due to unresolved atomic columns as can be expected from the ball and stick model of the first order twins, with a [552]-oriented normal, along the [-111] view direction (Figure 6.3(c)). This could also

occur because of the overlapping of the twinned and epitaxial regions when viewing along the [-111] direction. As it is seen in Figure 6.3(a), the interface between GaSb and Si is not sharp due to the overlap of the first few atomic layers of GaSb with the atomic layers of Si surface along the step direction.

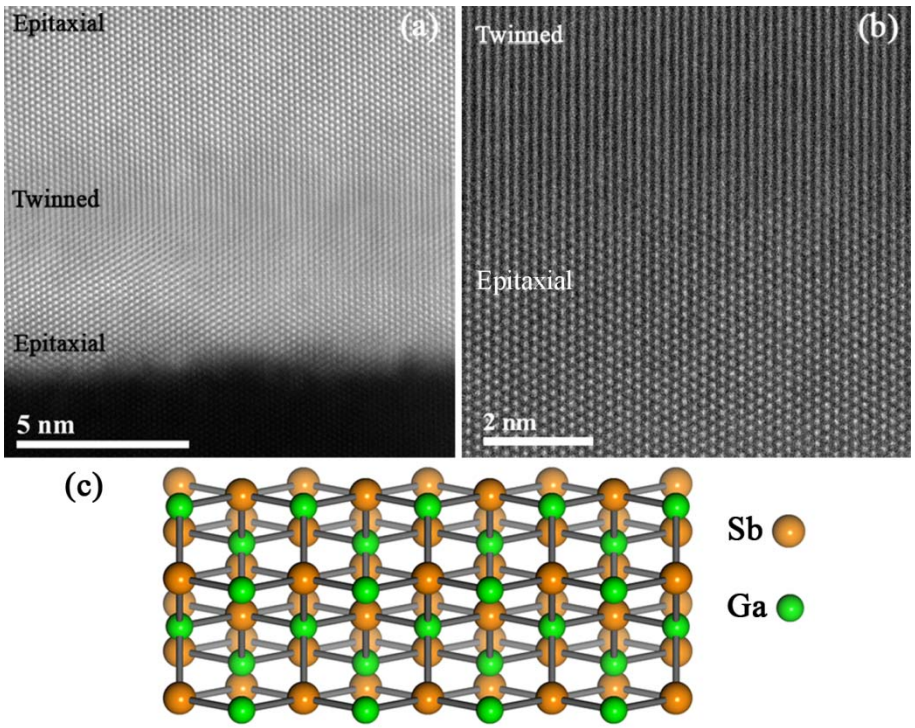

Figure 0.3: (a) HAADF-STEM image of specimen with [-111] zone axis, (b) magnified image of epitaxial and twinned stripes, and (c) ball and stick model of (552)-oriented twins along the [-111] zone axis.

The HAADF-STEM image of the [01-1] zone axis cross-sectional specimen in Figure 6.4(a) provides clear insight about the structure of the GaSb film at its interface with Si. Two regions of distinct lattice registry corresponding to the twinned (highlighted between red arrows) and untwinned (epitaxial) regions (highlighted between green arrows) are observed. The {111} atomic planes of

twinned GaSb and Si, highlighted by white lines at the left side of the Figure 6.4(a), are atomically well-registered as might be expected if there was no lattice-mismatch between the twinned GaSb film and the Si substrate. In contrast, the Burgers circuit (yellow lines) at the interface of epitaxial GaSb and Si displays the Burgers vector (blue arrow) of the interfacial misfit dislocations, indicative of the large lattice-mismatch between GaSb and Si. The red and green line drawn along the {111} planes of GaSb and Si, respectively, demonstrate a tilt of 2.5° between the GaSb film and the Si substrate in both epitaxial and twinned regions. The inset of Figure 6.4(a) is the Fourier transform (FT) of the image with red and green hexagons belonging to the reflection sets of the epitaxial and twinned gaSb, respectively. The same amount of tilt was also observed between (1-1-1) reflections of Si (blue arrow) and epitaxial GaSb (yellow arrow). These observations confirm the tilt between film and the substrate lattices previously seen in Figure 5.2(a). The atomic model reconstruction at the interface of the triple convergence of the Si substrate, the epitaxial GaSb region, and the twinned GaSb region (Figure 6.4(b)) reveals that Sb atoms preferentially bind to edge Si atoms regardless of the formation of epitaxial or twinned GaSb regions. Based on this observation and our growth procedure that initiates with Sb soaking, it is suggested that incoming Sb atoms stick to every available site on the Si surface. However, due to the low sticking coefficient of Sb to Si, Sb atoms are replaced by Ga atoms as soon as Ga atoms impinge on the Si substrate. Since the binding energy between Sb and edge Si atoms is stronger than between Sb and terrace Si atoms due to its two back bonds, Ga atoms preferentially substitute with terrace Sb atoms. As a result, a regular and uniform initial nucleation is promoted and a sublattice-ordered film is produced. This sublattice-ordering prevents mixed domain nucleation and hence prevents APB formation.

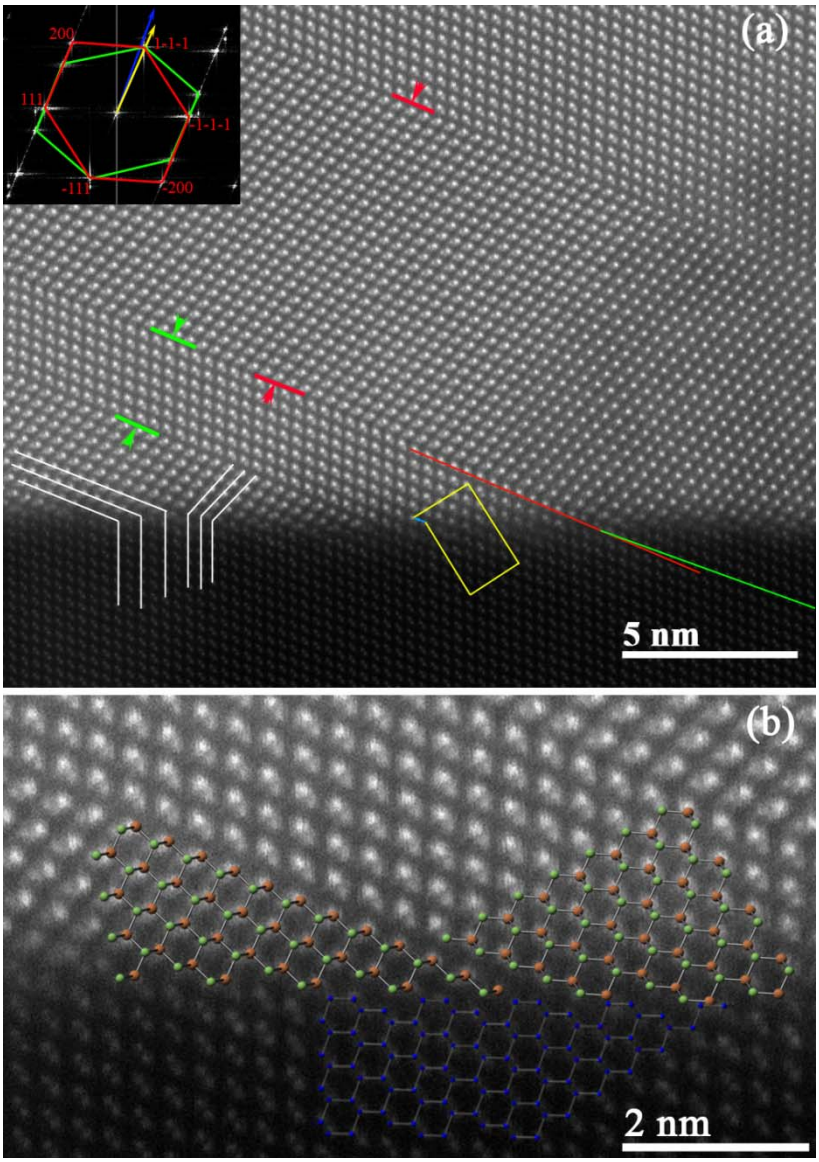

Figure 0.4: (a) HAADF-STEM image of specimen with [01-1] zone axis with its FT in inset, white lines highlighting the {111} planes in twinned GaSb and Si and yellow lines displaying the Burgers circuit and blue arrow as Burgers vector of the interfacial misfit dislocations. The red and green line shows the tilt between the GaSb and Si lattice. (b) A magnified image of the interface with superimposed atomic model.

In order to understand the origin of the GaSb lattice tilt, ball and stick models of the GaSb film on the Si(211) substrate were constructed. The ball and stick models in Figure 6.5 demonstrate the effect of GaSb lattice tilt with respect to the Si lattice on inducing lattice-registered growth of twinned GaSb film on Si. As seen in Figure 6.5(a), the {111} planes of Si and twinned GaSb without any tilt (highlighted by narrow back lines) are aligned at the interface; while the other sets of {111} planes of Si and {002} plane of twinned GaSb without any tilt (highlighted by continuous red lines) are not registered to one another. However, with a tilt of 2.5 degrees, twinned GaSb (Figure 6.5(b)) is registered with Si in two directions: a) {111} planes (red lines) in twinned GaSb with {111} planes of Si (highlighted by narrow back lines) b) {002} planes of twinned GaSb with the other sets of {111} planes of Si (highlighted with red continuous lines).

Figure 6.5(c) is a geometric representation of registered sets twinned GaSb and Si {111} which are highlighted in Figure 6.5(b). The registry of the two sets of planes at both sides of the interface yields $\frac{a_{Si}}{Sin\theta_1} = \frac{a_{GaSb}}{Sin\theta_2}$ in which θ_1 and θ_2 are the angle between the {111} planes of Si and GaSb with the interface, respectively. Using a_{Si} = 5.4310 Å, a_{GaSb} = 6.0959 Å and the value of θ_1 = 19.471° (calculated based on the crystallography of the lattice) as the angle between Si {111} planes and the interface, we can calculate the tilt angle, as $\omega_1 = \theta_2 - \theta_1$ = 2.500°.

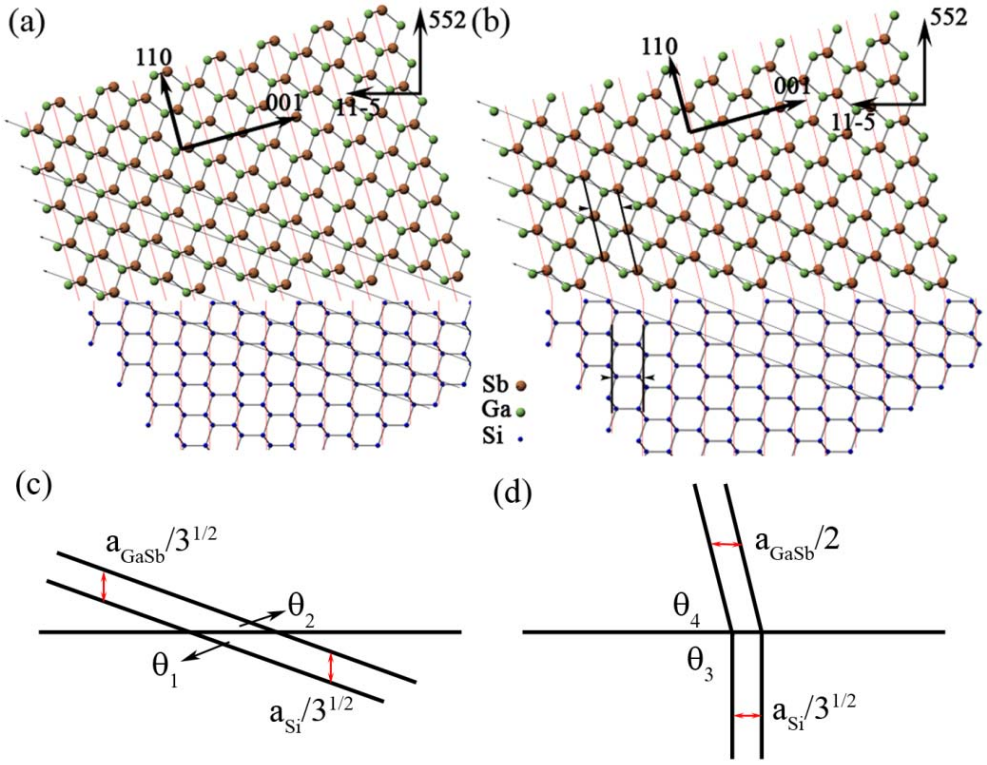

Figure 0.5: Ball and stick model of twinned GaSb films on a Si substrate (a) without tilt, (b) with tilt toward interface, (c) geometric representation of {111} planes of Si and GaSb with their spacing labeled, and (d) geometric representation of {111} planes of Si and {002} planes of GaSb with their spacing labeled.

Surprisingly, we find nearly identical registration between the other set of {111} planes and a major crystallographic direction of GaSb, i.e., the {002} planes. The geometric representation of the orthogonal direction in Fig. 6.5(d) (highlighted with thick black lines and indicated by black arrows for each set in Fig. 6.5(b) indicates the registration of the other set of {111} planes of Si and the {002} planes of twinned GaSb at the interface. It also implies that the two horizontal lines highlighted by red arrows necessarily have equal length. The variant region with [552]-oriented normal to the substrate produced by first order

twinning, causes {115} GaSb planes to be nominally aligned with {111} planes of the Si substrate. This leads to an angle of 74.207° between [002] and the surface normal [552] based on crystallographic considerations. The registry of these two sets of planes at both sides of the interface yields $\frac{a_{Si}}{\sqrt{3}\times Sin\theta_3} = \frac{a_{GaSb}}{2\times Sin\theta_4}$, with θ_3 = 90°. This results in $\theta_4 = \omega_2 + 74.207°$ and a calculated tilt angle, $\omega_2 = 2.215°$ for registration.

These models and geometric calculations shows that a very similar tilt angle (2.500° and 2.215°) can optimally align both the {111} planes of Si and GaSb and the other set of Si {111} planes with the GaSb {002} planes. If we use a slightly larger value (by 0.13%) for a_{GaSb} of 6.1039 Å, then we find that $\omega_1 = \omega_2$ = 2.530°, which is consistent with the measured value. The close and apparently coincidental nature of the agreement between orthogonal directions is based only on geometric considerations and the relative lattice constants of GaSb and Si. When this condition is met, the apparent lattice mismatch between GaSb and Si is reduced to zero in the twinned orientation. We note that this unusual geometric condition is only possible for highly lattice mismatched sets of materials as a result of simultaneous titling and twining-induced reduction in the interfacial strain.

6.3 Strain Analysis

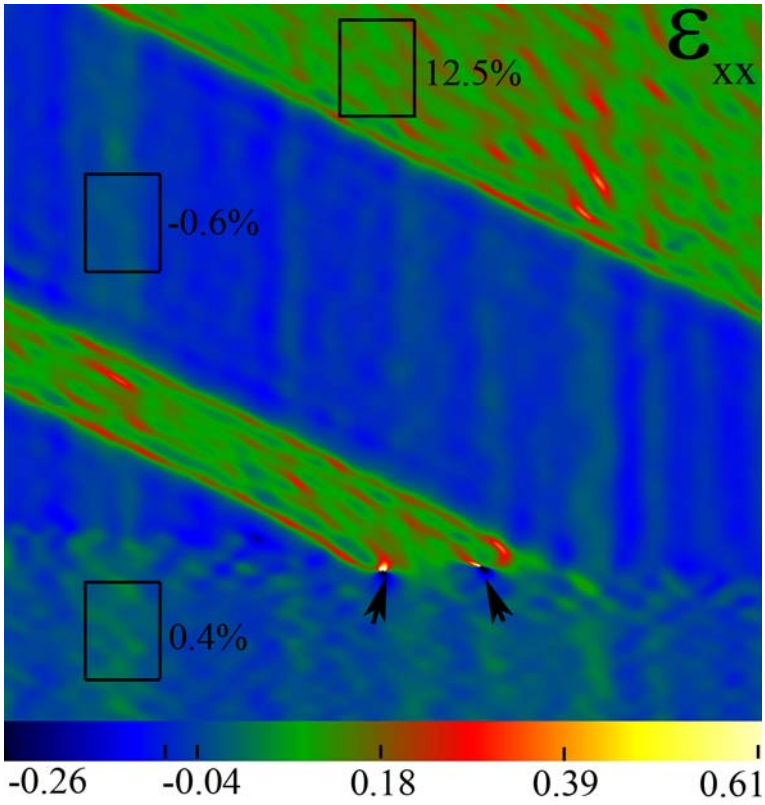

Figure 0.6: The GPA strain map parallel to the interface (ε_{xx}) with the average value of strain indicated for each of the rectangles representative of the Si lattice (0.4%), the epitaxial GaSb film (12.5%) and the twinned GaSb film (-0.7%). The analyzed region is the same as shown in Figure 6.4(a).

To investigate the effect of the lattice tilt of the GaSb film on the overall strain distribution of the GaSb film shown in Figure 6.4(a), (111) and (1-1-1) lattice reflections were analyzed using GPA with a mask size of 1.1 nm^{-1} resulting in a spatial resolution of 0.89 nm. The average values of strain in the rectangles in displayed in each region of the figure. The strain map parallel to the interface (ε_{xx})

in Figure 6.6 indicates that the apparent strain of the twinned GaSb regions is almost the same as in Si which is used as a reference lattice (and thus has a zero percent strain). However, the apparent strain of the epitaxial GaSb reaches its bulk value with respect to Si as highlighted in the figure. While the interfacial misfit dislocations are formed to release strain between the film and substrate at the interface of the epitaxial GaSb region and the Si substrate, the twinned GaSb grows without formation of any interfacial misfit dislocations as expected from lattice-registered heteroepitaxy.

6.4 Summary

The results presented here demonstrate the remarkable observation of lattice-registered MBE growth of GaSb on a Si (211) substrate, leading to strain relaxation in two of the three crystallographic directions of the epitaxial film. The direct detection of atomic configurations at the interface displays that the preferential bonding of atomic species to atomic sites on the Si surface results in sublattice-ordering and hence avoids the formation of APBs. The GaSb film is fully relaxed with the correct lattice constant of ~6.1 Å, and it is registered with the Si lattice in two orthogonal directions through a lattice tilt of 2.5°. We speculate that this tilt is energetically driven by the consequent strain relief. A similar registration is not expected in the perpendicular [01-1]-direction, where misfit dislocations are expected to primarily accommodate the significant lattice mismatch between the GaSb film and the Si substrate as in the case of GaSb on Si(100).

Chapter Seven

Growth Mechanism of GaSb Epilayer on Si

Epitaxial growth of the group III-Sb based semiconductor compounds has been motivated by monolithic integration of a wide range of electronic properties with the existing Si platform. Using Si substrates for growing compound semiconductors has significant advantages, such as the low cost, high quality of the wafer supply and the numerous benefits of using a well-established manufacturing platform. Accordingly, understanding the growth mechanism of GaSb and AlSb epilayers can pave the way toward highly lattice-mismatched heteroepitaxy. The very first report of growing GaSb films on Si substrate dates back to Malik et al. work [95]. Their Normanski interference microscopy and TEM observations demonstrated that the GaSb film was not of ultimate quality. The high lattice mismatch of Sb-based compounds and Si substrates presents fundamental growth problems and hence understanding the growth mechanisms of GaSb and AlSb films is essential for growing high-quality films on Si. Despite the common usage of AlSb as a buffer for growing group III-Sb based compounds, it is not thoroughly understood that how the AlSb buffer layer

influences the growth of GaSb epilayers. AFM and RHEED, as prevalent characterization tools for investigating the epitaxy process, are unable to explain the interfacial phenomena. However, as it was seen in previous chapters of this thesis, state-of-the-art aberration-corrected transmission electron microscopy has displayed phenomenal capabilities in the investigation of interfaces and defects. The use of atomic resolution HAADF-STEM in a spherical aberration corrected electron microscope capable of forming sub-angstrom electron probes offers important advantages in pinpointing the individual atomic columns at interfaces and defects. The atomic number-dependent [11] contrast can clearly identify the location of interfaces and morphology of growth and therefore provide a direct insight about the growth mode and mechanisms.

Consequently, in this chapter, we present a detailed study of the GaSb/Si interface structure with and without AlSb buffer. The mechanism of growth was investigated by aberration-corrected HAADF-STEM imaging to elucidate the interfacial structure and to identify the morphology and the role of the AlSb buffer layer on the film structure.

7.1 Methodology of Experiments

Epitaxial samples were grown based on two main objectives: investigating the effect of AlSb layer thickness and studying the growth mode of GaSb epilayers on Si. Therefore, the samples were grown based on the procedure explained in Chapter Three. In order to compare the epilayers grown on Si(001) with various thicknesses of AlSb buffer and GaSb films, the growth conditions were rigorously maintained. Table 7.1 summarizes the details of the film thicknesses and substrate type for different samples.

Table 0.1: Details of substrate orientation and thickness of AlSb and GaSb epilayers in different samples.

Sample	Si(001) Substrate Type	Thickness of AlSb Buffer (nm)	Thickness of GaSb Film (nm)
A	Vicinal 4.7° towards [110] tilt orientation	0	500
B	Vicinal 4.7° towards [110] tilt orientation	0.31 ~ 2 Monolayer	500
C	Vicinal 4.7° towards [110] tilt orientation	20	500
D	Nominal	0	5
E	Nominal	5	5
F	Nominal	5	10
G	Nominal	5	20

7.2 Role of AlSb Buffer Layer

The HAADF-STEM investigation of cross-sectional specimen of sample **A** in Figure 7.1(a) indicates that the deposition of a GaSb epilayer on a Si substrate without using a AlSb buffer results in the formation of large coalesced islands with occasional minor solitary islands (indicated by red arrows). Moreover, the surface of the film in the coalesced regions is not planar, clearly demonstrating that the coalescence of the islands is incomplete even after 500 nm deposition of GaSb. The high contact angle of the GaSb islands with the Si substrate (highlighted by yellow dotted lines in Figure 7.1(a)) implies that the higher surface energy of GaSb compared to Si along with the large lattice-mismatch prevents the formation of 2D film growth [Ref. 100]. The high surface energy of GaSb also inhibits the complete wetting of the Si surface resulting in the formation of voids in between the coalesced islands (pointed by yellow arrows). As highlighted in Figure 7.1(b), the electron microscopy analysis of the

GaSb/Si interface of the samples also displays substantial surface roughness at the interface with the Si substrate caused by the film growth, suggesting that GaSb has replaced Si in some regions. The GaSb islands formed on the Si substrate also exhibit high density of multi-twinning. Figure 7.1(c) shows a GaSb island with first-order and second-order twins. The red arrows highlight two stacking faults which have formed to assist the arrangement of multiple variants of high-order twinning at their convergence region. Yellow arrows in Figure 7.1(c) also display the formation of incoherent boundaries at the intersection of twins resulting in atoms with dangling bonds and a major disruption in atomic arrangements.

Using the elemental mapping through EDXS at the interface (Figure 7.2 (a-d)), we studied the interfacial region shown in Figure 7.1(b) and determined that GaSb is present below the nominal Si surface. The chemical maps of Ga (Figure 7.2(c)) and Sb (Figure 7.2(d)) clearly demonstrate that GaSb has dissolved the Si substrate locally and penetrated below the apparent surface line of the Si substrate. The surface of the Si substrate in Figure 7.2(b) is completely different from what we have reported in the GaSb film grown on Si using the AlSb buffer in Chapter Four. This surface roughness of Si induces a high density of planar defects inside the GaSb islands. Therefore, the observed multiple twinning can be attributed to the surface roughness of Si substrate or resulted from the accommodation of the large misfit strain.

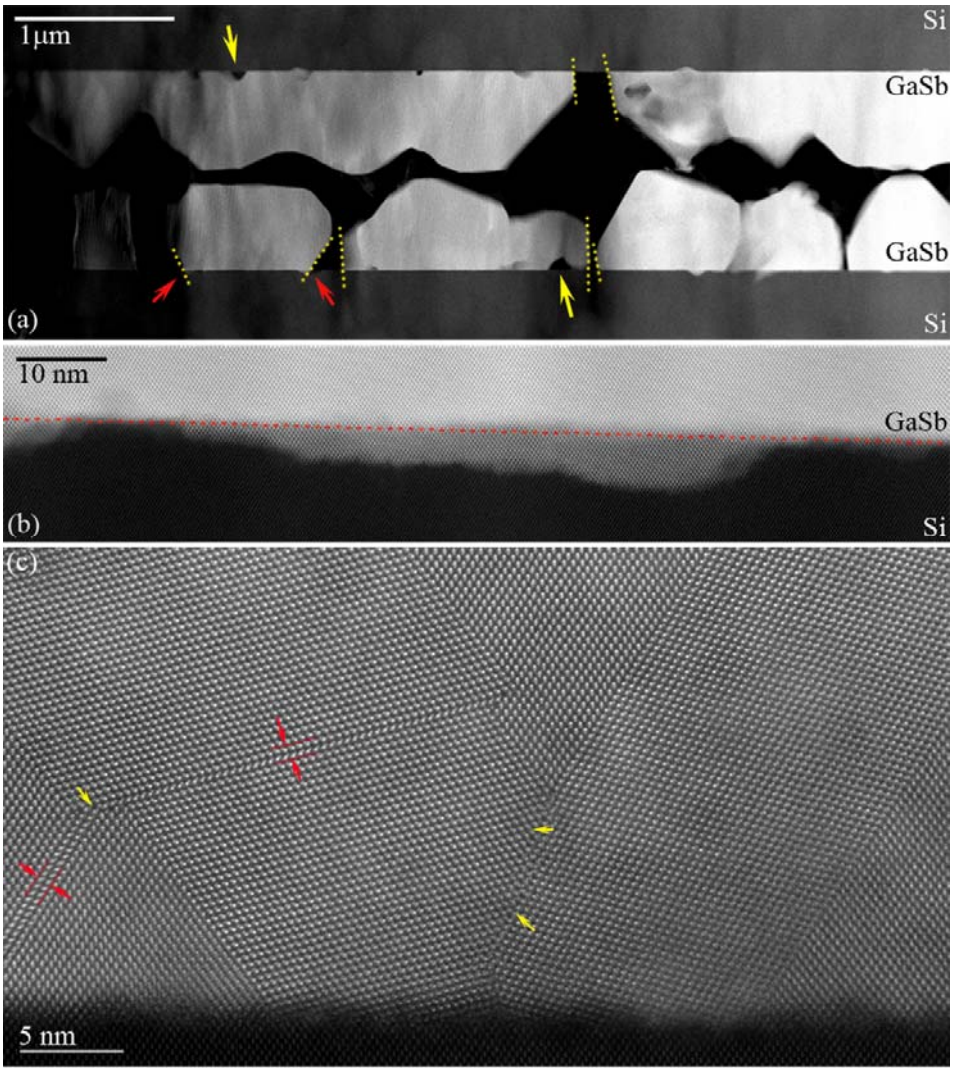

Figure 7.1: (a) HAADF-STEM image of the [1-10] cross-section specimen of sample **A** with red and yellows arrows indicating solitary island and voids in GaSb layer, respectively and yellow dotted lines highlighting the contact angle between GaSb islands and Si, (b) magnified image of the interfacial region with red dashed line showing the Si substrate surface, and (c) atomic-resolution HAADF-STEM image of a GaSb island containing multiple-twinning with red arrows highlighting the stacking faults and yellow arrows indicating incoherent intersection of twins. In the part (a) the sequential order of the sandwich TEM sample from above is: substrate / film / glue / film / substrate.

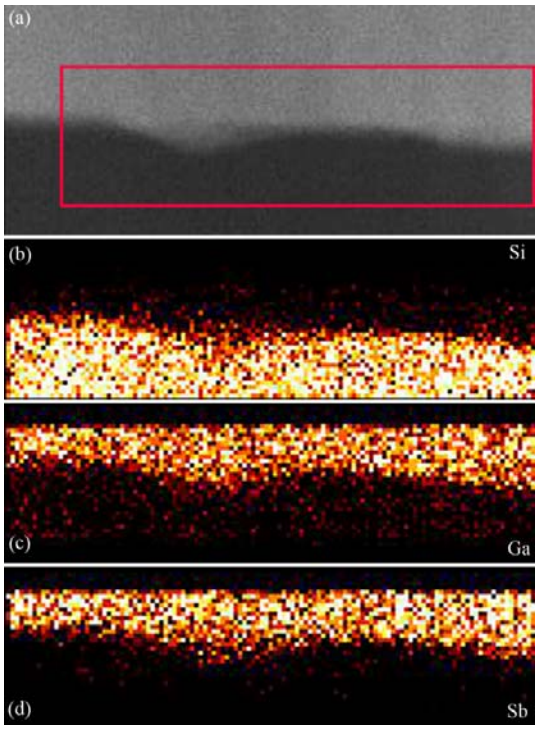

Figure 0.2: (a) HAADF image of sample **A** highlighting, with a red rectangle, the area where EDXS mapping was carried out: (b) Si, (c) Ga, and (d) Sb maps.

In order to study the effect of the AlSb buffer layer, sample **B** was grown using a two monolayer thick AlSb buffer layer prior to the deposition of the GaSb epilayer. The AlSb layer was not seen directly, however we observe (Figure 7.3(a)) that the AlSb layer significantly improves the growth characteristics of the GaSb epilayer even with thicknesses as thin as two monolayers. The AlSb buffer layer facilitates the coalescence of GaSb islands at lower film thicknesses. Planar growth of GaSb is therefore achieved with 500 nm deposition of GaSb, resulting in an almost smooth film surface. However, electron microscopy analysis of the interface shows that the interface of GaSb and Si still suffers from local melting as seen in Figure 7.3(b). The GaSb film also contains multiple twinning due to the effort of deposited film to maintain the orientation of the rough surface of Si.

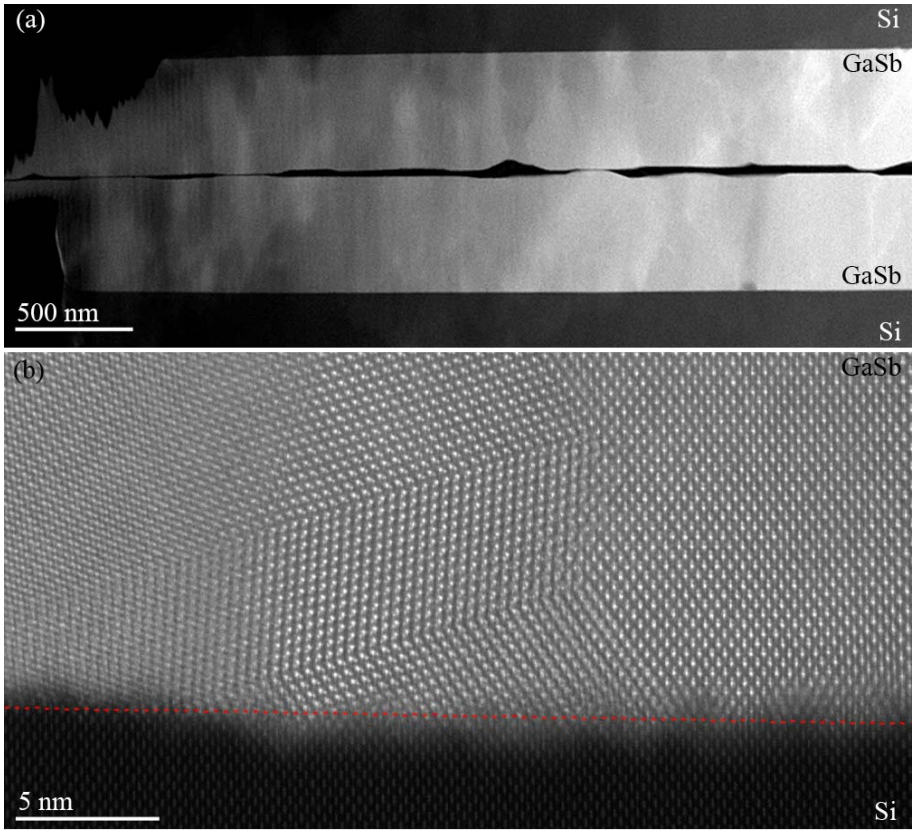

Figure 0.3: (a) HAADF-STEM image of the [1-10] cross-section specimen of sample **B** and (b) magnified image of the interfacial region with red dashed line showing the Si substrate surface. In the part (a) the sequential order of the sandwich TEM sample from above is: substrate / film / glue / film / substrate.

Increasing the thickness of the AlSb deposited layer to 20 nm (sample **C**) resulted in the direct observation of the AlSb islands which appear with weaker HAADF signal intensities due to the lower atomic number of the Al atoms as compared to the Ga atoms (Figure 7.4(a)). We have observed similar results with deposition of a 5 nm AlSb buffer layer (Chapter 4); but with smaller AlSb islands. The formation of AlSb islands has prevented the local melting of the Si substrate

(Figure 7.4(b)) and hence, misoriented GaSb regions due to the substrate roughness are absent.

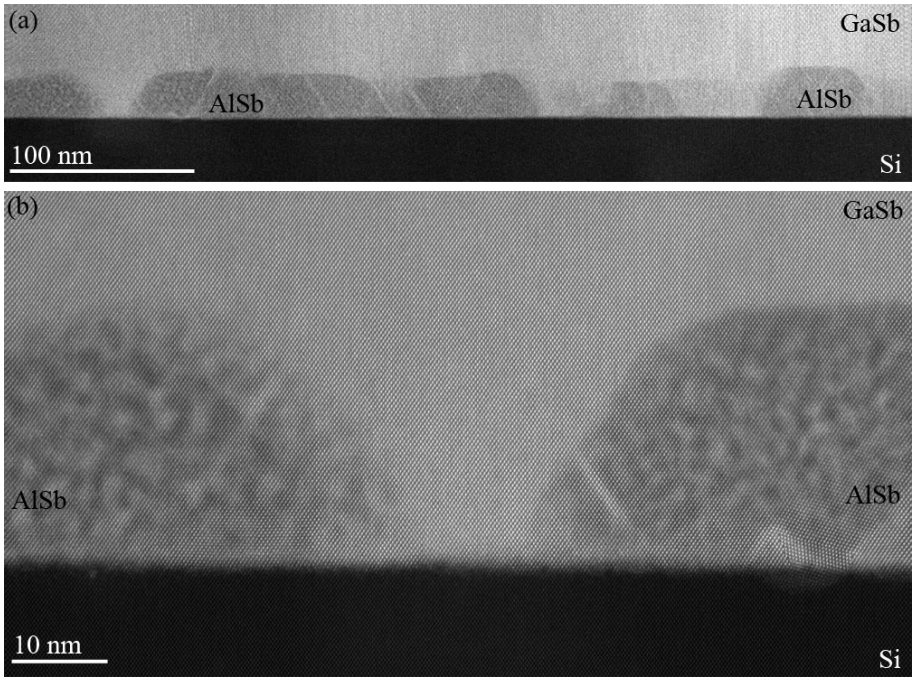

Figure 0.4: (a) HAADF-STEM image of the [1-10] cross-section specimen of sample **C** and (b) magnified image of the interfacial region with AlSb islands appearing darker than the GaSb film.

The evolution of the GaSb film and the change in Si surface roughness at the interface with GaSb with the introduction and variation of the of AlSb buffer layer thickness shows that using an AlSb buffer layer is not only necessary for forming planar GaSb films but is also crucial for avoiding the dissolution of Si. It was shown in Chapter Five that although the growth begins with super-saturating the Si substrate with Sb atoms, Sb atoms substitute with Ga atoms at the interface as soon as the Ga flux is initiated due to the low sticking coefficient of Sb to Si compared to that of Ga at the growth temperature of 600 °C. Ga atoms can

therefore be first atomic monolayer on the Si surface in some regions. Ga atoms have a longer surface diffusion length (i.e. mean distance between the point that an atom is adsorbed to the point that is incorporated into crystal structure) as compared to Al atoms [100, 171] which can cause a local accumulation of Ga atoms before bonding to Sb. Based on phase diagram of Ga-Si, diffusion of few Si atoms into Ga can result in the formation of eutectic composition and consequently melting point of Si, drastically decreases to that of the eutectic composition. Considering the amount of Si atoms that are needed for the formation of eutectic composition and the size of the surface roughness caused by Si dissolution in Ga, the Ga droplet will soon supersaturate. From this, we surmise that the Si atoms precipitate somewhere on the Si substrate which are not detected in our EDXS maps. In contrast, the much shorter surface diffusion length of Al and stronger bonding between Sb and Al preclude the occurrence of Si local melting. Roughening of the Si surface was not observed in GaSb grown at lower temperatures (such results are not presented for conciseness) implying a higher rate of Sb desorption from the surface as well as a smaller Ga diffusion length at lower temperatures.

7.3 Growth Mechanism of GaSb

To understand the growth mechanism of the GaSb epilayer on the Si substrate at early stage of growth, a sample with 5 nm of GaSb was grown (as compared to 500 nm for sample **A**). TEM investigation of the 5 nm deposited GaSb film on Si (sample **D**) displays GaSb islands formed sparsely-distributed on the Si substrate (Figure 7.5(a)). The majority of islands are dispersed at least 1 μm apart on the Si substrate surface. These GaSb islands have fairly uniform size with a height of 40 nm and width of 60 nm. It is seen in Figure 7.5(b) that the voids in GaSb islands resulting from high surface energy of GaSb are formed during the

initial stage of growth and persist till higher thickness of GaSb depositions as observed in Sample **A**. The local melting of the Si substrate, due to the direct growth of GaSb on Si, is also seen in Figure 7.5(c) and in this case generated a small crevice in the corner of the island with additional deposited material penetrating into it.

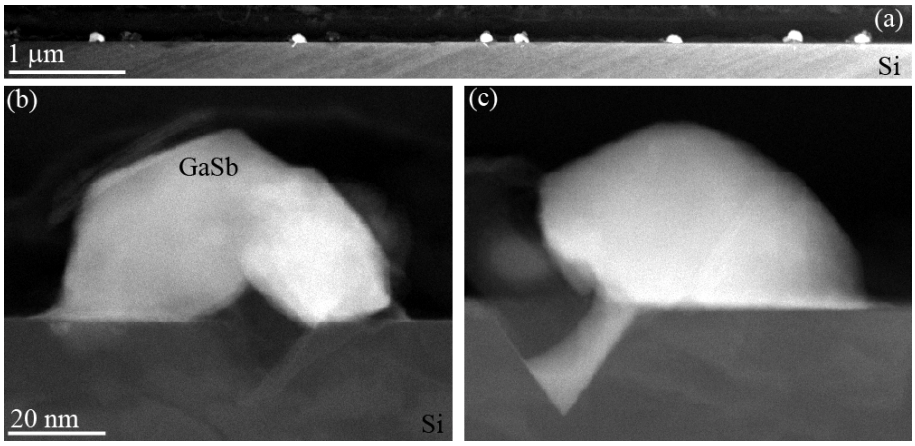

Figure 0.5: (a) HAADF-STEM image of sample **D** (b) a GaSb island with a void in middle, and (c) local melting of Si substrate showing the diffusion of the over-layer into Si substrate.

The EDXS maps in Figure 7.6 demonstrate that, as expected, Ga atoms (Figure 7.6(c)) are responsible for the local melting of the Si substrate due to the presence of Ga in the crevice created by the local melting. As highlighted by arrows in Figure 7.6 (c) and (d), some of the Ga atoms have not reacted with Sb atoms and have formed Ga particle adjacent to GaSb islands. We believe that Ga atoms due to high surface diffusion migrate on the surface and incorporate to each other and form Ga droplets at growth temperature and, if they have enough time, they gradually form GaSb islands with the incoming Sb_2 flux. The existence of un-reacted Ga droplets in this sample can be associated to high growth rate

compared to the film thickness since the Ga atoms do not have sufficient time to react with Sb atoms. However, fully understanding of this phenomenon needs further investigations.

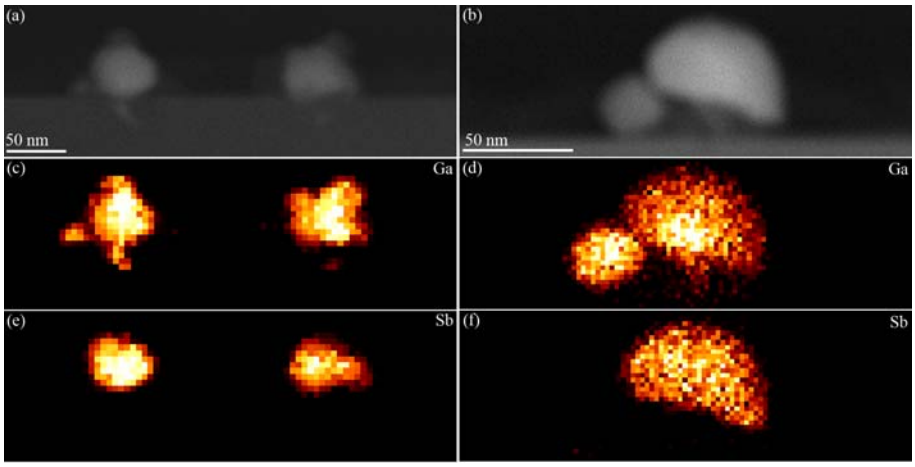

Figure 0.6: (a) and (b) HAADF-STEM images of two GaSb islands which EDXS mapping was carried out with (c) and (d) Ga maps and (e) and (f) Sb maps.

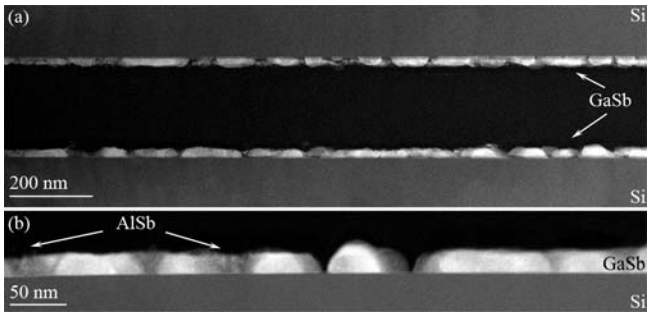

Figure 7.7: (a) A low-magnification HAADF-STEM image of the [1-10] cross-section specimen of sample **E**, (b) coalesced and individual GaSb islands adjacent to AlSb islands indicated by arrows with uncapped AlSb islands pointed by arrows. In the part (a) the sequential order of the sandwich TEM sample from above is: substrate / film / glue / film / substrate.

To better understand the role of the AlSb buffer layer, a series of GaSb epilayers with different thicknesses were deposited after deposition of a 5 nm thick AlSb buffer layer. The low magnification HAADF-STEM image of sample **E** with 5 nm thick GaSb film grown using 5 nm AlSb buffer in Figure 7.7(a) displays the very significant influence of AlSb in promoting the GaSb growth on Si. Although the growth front is not still planar, the scattered GaSb islands have grown denser (Figure 7.7(b)). The AlSb islands are laterally elongated as compared to GaSb islands of the same deposited epilayer thickness (Figure 7.5(b and c)). In the higher magnification image in Figure 7.8(a) and (b), the AlSb islands are discernible by their lower HAADF signal intensities as expected due to the lower atomic number of the Al atoms as compared to the Ga atoms. As seen in Figure 7.8(a) the GaSb tend to grow at the side walls of the AlSb islands due to the lower nucleation energies because of lower surface energies of {111} planes in GaSb structure. With further deposition of GaSb, the growth continues at the side walls and above the top surface of the AlSb islands. Eventually if sufficient GaSb epilayer is deposited, the AlSb islands would be buried underneath of the GaSb islands (indicated by yellow arrow in Figure 7.8 (a)). The apparent disordered and spotty appearance of the AlSb islands seem to be oxidation or ion-milling artifacts due to exposure of bare AlSb islands (not fully capped by GaSb) to air during sample preparation and handling and small deposition thickness. This growth mechanism of the GaSb film suggests that GaSb islands nucleate heterogeneously adjacent to the AlSb islands. Despite the fact that the AlSb buffer produces 3D islands on the Si substrate due to the high interfacial energy similar to GaSb, the morphology of the AlSb islands are distinctly different from the GaSb islands in terms of size and shape of the islands. AlSb islands form truncated pyramids of 20 nm height with rectangular base of 50 to 60 nm width.

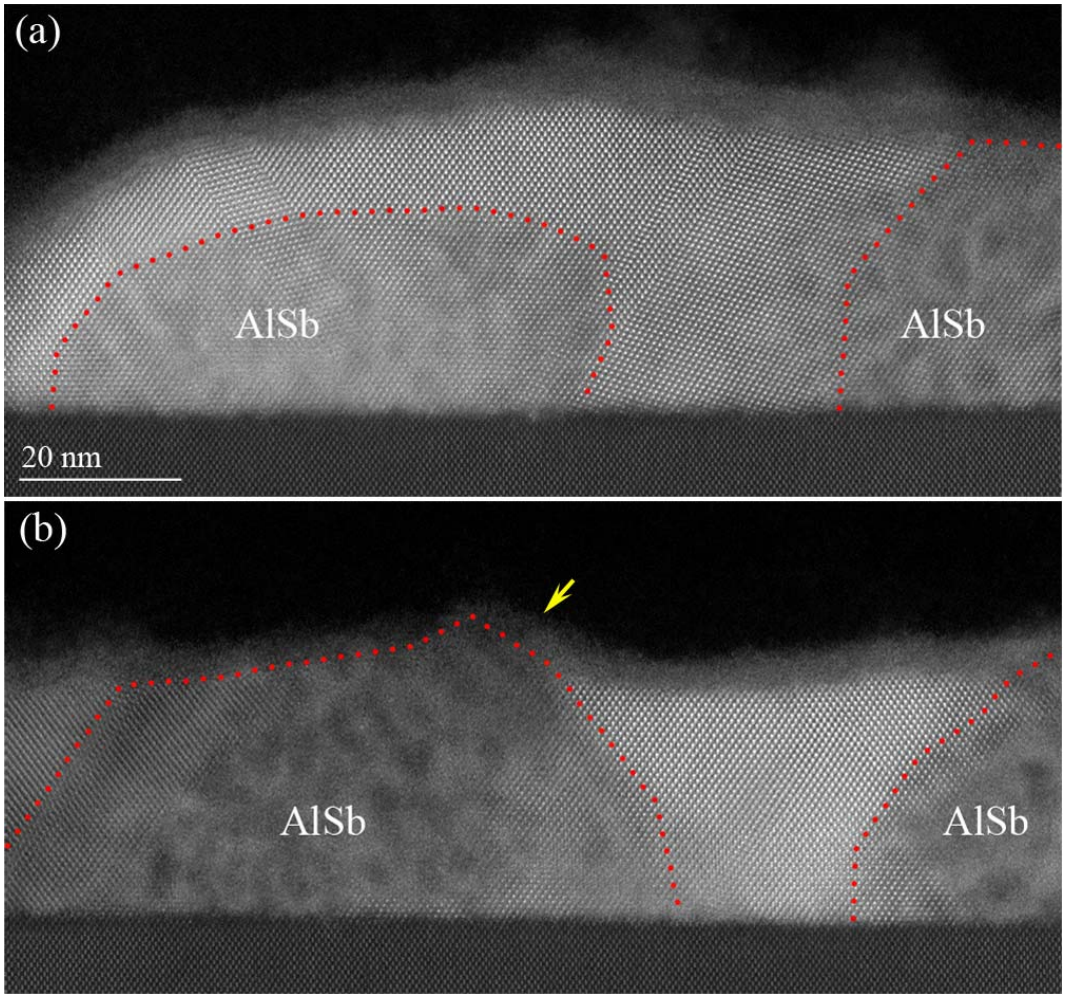

Figure 0.8: (a) A high-magnification HAADF-STEM image of the [1-10] cross-section specimen of sample **E** and (b) oxidized uncovered AlSb islands highlighted by a yellow arrow.

To further study the growth evolution of GaSb epilayers, a GaSb layer of 10 nm thickness (sample **F**) was investigated. Figure 7.9 displays the low-magnification overall view of the GaSb layer in which uncovered AlSb islands (one indicated by red arrow) are still present. The presence of at least one AlSb island inside each GaSb islands strongly supports our speculation of the

heterogeneous nucleation of the GaSb islands adjacent to the AlSb islands. The examination of the higher magnification views of the GaSb islands in Figure 7.10 indicates that the growth of GaSb islands initiates at the side walls of the AlSb islands (Figure 7.10(a)) and proceeds until covering the entire the AlSb island (Figure 7.10 (b) highlighted by red arrow).

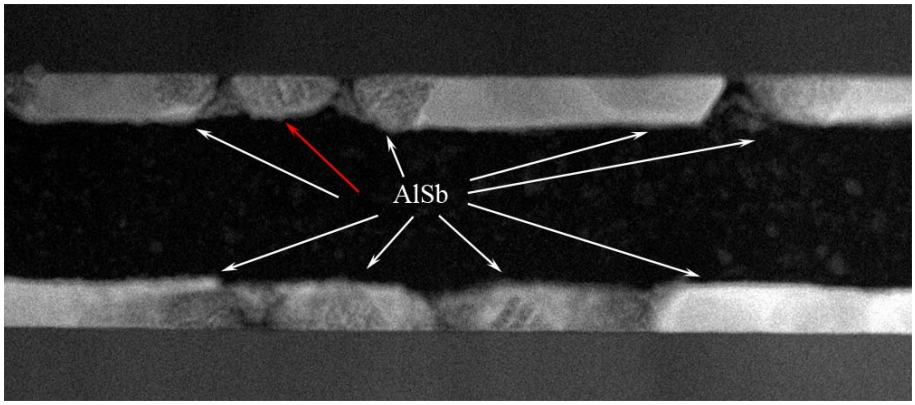

Figure 0.9 Overall view of sample **F** (10 nm thick GaSb layer grown on Si using a 5 nm thick AlSb buffer layer) at low magnification with white arrows indicating AlSb islands inside GaSb islands. Red arrow shows an uncovered AlSb island. The sequential order of the sandwich TEM sample from above is: substrate / film / glue / film / substrate.

As seen in Figure 7.11, by increasing the thickness of the deposited GaSb layer to 20 nm (sample **G**), the majority of the GaSb islands coalesce and the growth front become flatter compared to films with smaller thicknesses (Figure 7.7 and 7.9). The length of coalesced islands at this point is 250 nm or even greater in most of the regions on the surface of the Si substrate; however, there are still some uncovered regions of the Si surface indicated by red arrows. The yellow arrows in Figure 7.11 highlight steps along the film surface due to the coalescence of the GaSb islands with different heights.

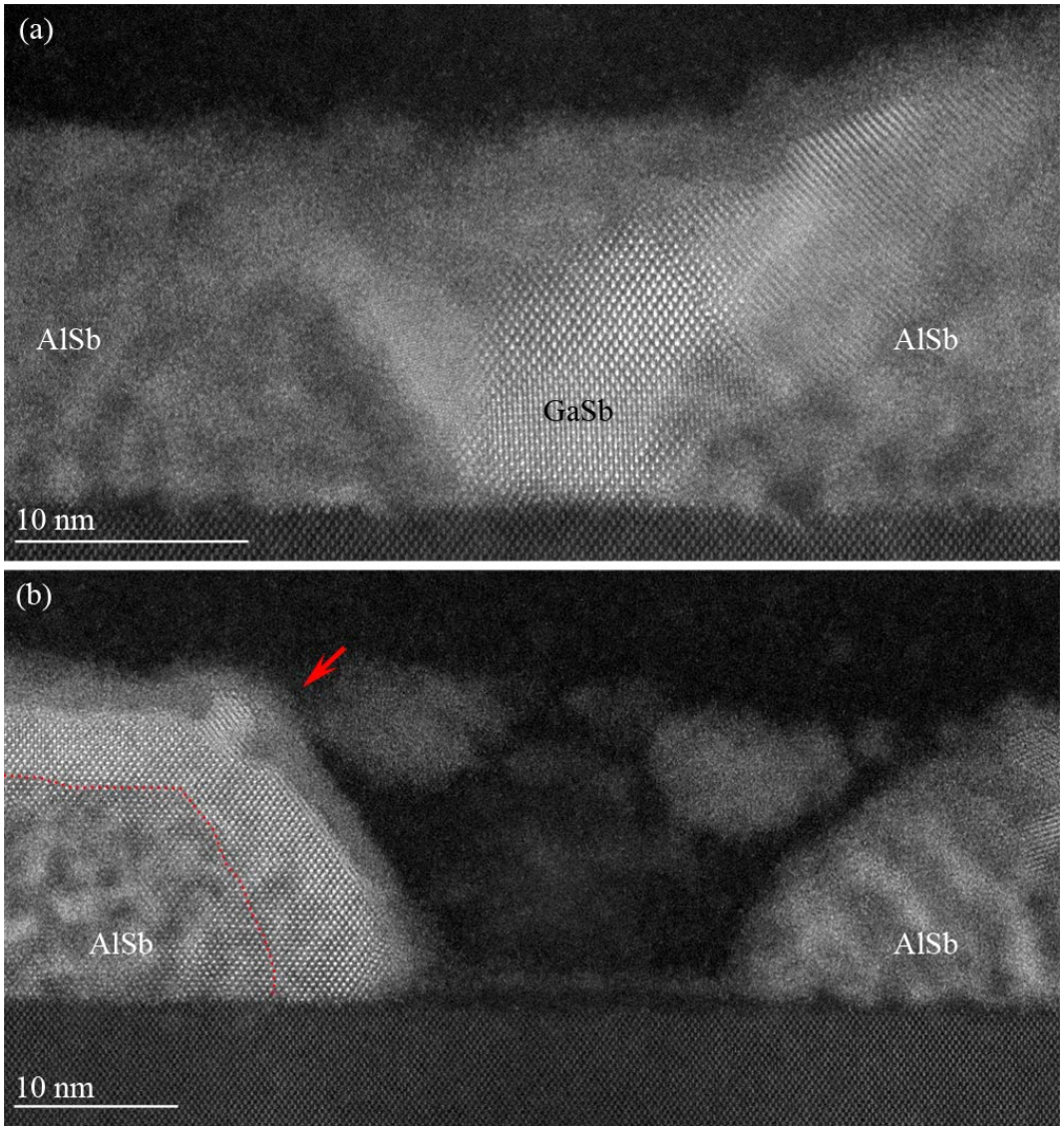

Figure 0.10: High-magnification image of GaSb islands (a) nucleating adjacent to AlSb island and (b) covering AlSb island with red dotted line showing covered AlSb island and red arrow indicating the GaSb island.

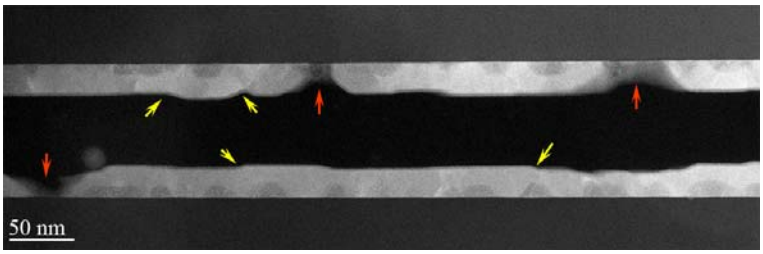

Figure 0.11: Overall view of sample **G** 20 nm thick GaSb layer grown on Si using a 5 nm thick AlSb buffer layer) at low magnification. Red and yellow arrows show uncovered Si surfaces and height differences on GaSb film surface, respectively.

The higher magnification imaging of the samples shows that the GaSb islands have a similar morphology to the AlSb islands during growth and that the AlSb islands play a template role for subsequent growth of GaSb islands, as illustrated clearly in Figure 7.12(a). Figure 7.12(b) displays a surface step on the GaSb film resulting from the coalescence of two GaSb islands with unequal growth heights formed on two coalesced AlSb islands. The coalescence of GaSb islands is sometimes accompanied by formation of twins as seen in Figure 7.13(a) or anti-phase boundaries as seen in Figure 7.13(b). The formation of twins that are induced by the low energy associated with the creation of stacking faults in the zincblende crystal structure of GaSb and AlSb helps the registry of atomic layers at the interface of two islands. Figure 7.13(b) presents evidence of the formation of an anti-phase boundary at the contact plane of two AlSb islands with reversed polarity. The registered growth of GaSb on the AlSb islands, each with opposite polarities, resulted in the formation of two GaSb domains with opposite polarity, which then coalesced with an intervening anti-phase boundary. Therefore, this anti-phase boundary leads to the subsequent formation of anti-phase GaSb domains at either side of the AlSb island. Figure 7.13(c) displays the detailed view of the interface region where the APB intersects the substrate. The lower

intensity of the first atomic monolayer on the Si substrate at the left side of the anti-phase boundary compared to the right side unambiguously indicates the reversal of the first monolayer from Al to Sb.

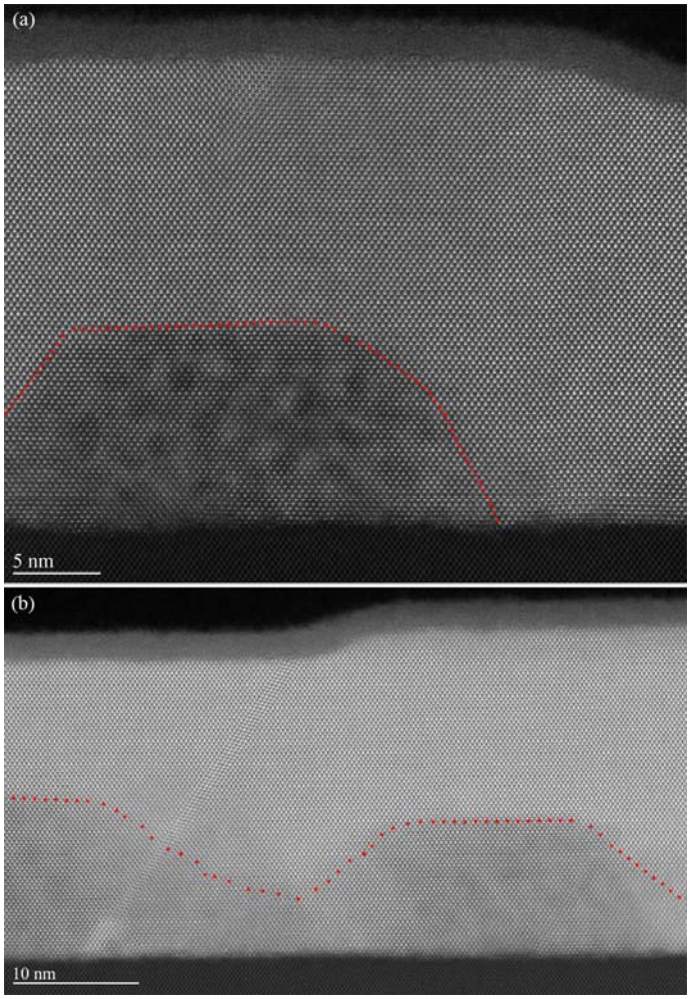

Figure 0.12: (a) High-magnification HAADF-STEM image of AlSb island with lower HAADF signal intensity at the interface and the GaSb film following the outline shape of AlSb and (b) two coalesced AlSb islands with subsequent GaSb film on top with different height of growth.

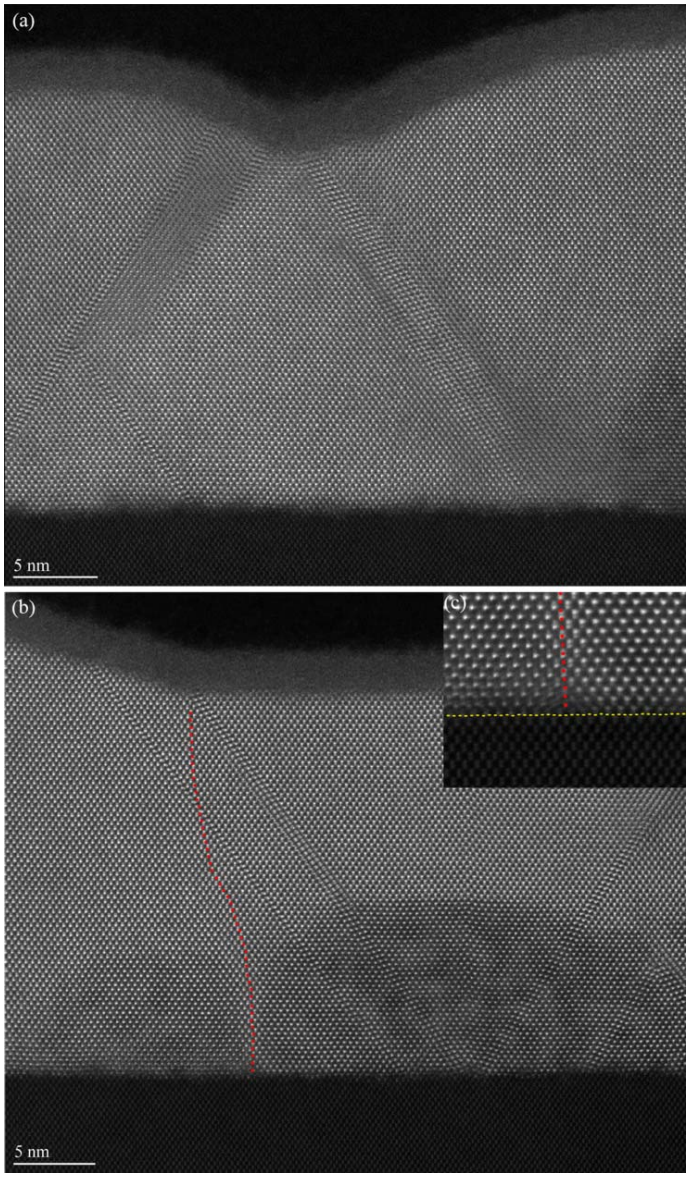

Figure 0.13: (a) Formation of twin boundaries at the interface of two GaSb islands (b) an anti-phase boundary (highlighted with red dotted line) starting at the Si surface at the contact plane of two AlSb islands and continuing into the GaSb film, the insert in (b) displays the interface of AlSb and Si substrate at the anti-phase boundary, red dotted line and yellow dashed line show the anti-phase boundary and the last atomic plane of Si surface.

Our observations of the evolution of GaSb epilayers structure with increasing thickness using an AlSb buffer layer indicate that AlSb forms a higher density of nuclei as compared to GaSb alone. This is due to the smaller diffusion length of Al compared to Ga which causes Al atoms adsorbed to the Si surface to have more time to bond to the substrate before the chance of diffusion on the surface. The greater the number of AlSb nuclei, the higher is the formation probability of nuclei of critical minimum size and growth. Therefore, the density of the AlSb islands on the Si surface is larger than the GaSb islands. These densely nucleated AlSb islands act as appropriate nucleation site for GaSb due to decreased interfacial surface energy as well as significantly smaller misfit strain of 0.6% between AlSb and GaSb. Hence, the deposited Ga and Sb species nucleate as GaSb on the side walls of AlSb islands. These densely nucleated AlSb islands also restrain the surface diffusion of Ga atoms and consequently prevent the local melting of the Si substrate surface. The presence of uncovered Si surface regions implies that GaSb does not form a uniform 2D film among AlSb islands as previously suggested [Ref. 100]. This also contrasts with the conclusion made by other groups as AlSb forms a wetting layer or plays a surfactant role [22, 100, 108, 109, 119]. This is because if AlSb had formed a wetting layer on all over the Si substrate, GaSb epilayers would have grown as a 2D film among AlSb islands because of lower interfacial energy. Nucleation of GaSb on the side walls of AlSb islands further proceeds until GaSb growth fronts from each side coalesce above the AlSb islands, completely encapsulating them. The AlSb islands serve as a template for GaSb to grow due to the similarity between the peripheries of the AlSb and GaSb islands. Subsequent deposition of GaSb results in the increase in the size of the GaSb islands and coalescence of neighboring islands. When adjacent islands merge, the interface between them are often delineated by faults. These faults can be either due to the misfit that introduces a small random rearrangement between the lattices of neighboring islands [172] or due to the

reversed polarity between them as seen in Figure 7.13(b). The resultant grooves where adjacent GaSb islands touch are energetically favorable for newly impinging atoms to bond, in order to reduce chemical potential and hence surface energy and curvature. Further deposition of GaSb leads to the formation of a planar growth front and hence smooth film surface at higher thicknesses. This is the 3D island, or so-called Volmer-Weber (VW), growth mechanism of AlSb and GaSb epilayers on Si that has been previously observed in InSb films grown on GaAs substrates [173] where the high lattice mismatch and interfacial surface energy is the common characteristics of all these systems. Although the Volmer-Weber growth mode tends to result in a large amount of imperfections in the epilayers, including threading dislocations, planar defects such as stacking faults, twins and anti-phase boundaries, GaSb films of enhanced structural quality are still achieved by introducing the AlSb buffer layer.

7.4 Summary

We have presented the results of detailed structural imaging using the HAADF-STEM technique of the initial growth stages and evolution of deposited GaSb epilayers on Si substrates. The atomic-number sensitivity of this imaging technique enables the discrimination between GaSb and AlSb islands and indicates that GaSb and AlSb epilayers growth occur by the 3D island (so-called Volmer-Weber (VW)) growth mode rather than the monolayer followed by island (Stranski-Krastanov) mode. Without a buffer layer, growth of GaSb layers on Si leads to large coalesced islands with non-planar surfaces even at thicknesses as high as 500 nm due to high surface diffusion of Ga atoms. The surface diffusion of Ga atoms additionally causes formation of surface pits at the interface with Si due to the local melting of the Si substrate. Introducing the 3D island-forming AlSb buffer layer, prior to deposition of the GaSb layer, significantly changes the

film characteristics of subsequent GaSb layers since AlSb islands act as energetically favorable sites for nucleation of highly lattice-mismatched GaSb islands on Si. Subsequent growth, coalescence, and planarization of GaSb epilayers results in smooth GaSb films with considerably enhanced quality.

Chapter Eight

Conclusions and Future Works

High lattice mismatch and heterovalent characteristics of the GaSb/Si interface influence the GaSb/Si interface by causing high density of structural defects including threading dislocation, twins, stacking faults, and anti-phase boundaries. These defects can strongly change the electronic structure of heterojunction and hence deteriorate the electrical properties. This chapter summarizes the finding of the thesis and presents concluding remarks of present work.

8.1 Conclusions

Atomic-resolution imaging using high-angle annular dark-field (HAADF) technique in aberration-corrected scanning transmission electron microscopy enabled unprecedented observations on growth and strain relief mechanisms as well as detection of defects and has allowed the study of their origins. These observations have not only changed our perceptions and anticipations of epitaxial growth of group III-antimonide compound semiconductors (AlSb and GaSb) on

Si but also broadened our knowledge on highly lattice-mismatch polar-on-nonpolar epitaxial growth. Introducing the 3D island-forming AlSb buffer layer prior to depositing GaSb layer significantly facilitated the planar growth of GaSb epilayers and enhanced their quality. AlSb islands act as a template for subsequent growth of GaSb, hinder the surface diffusion of Ga atoms and prevent the formation of Ga droplets and hence local melting of the Si substrate. Depositing the 5 nm AlSb buffer at 600°C can optimally improve the growth of GaSb film. The investigation of the local distribution of strain indicated that both AlSb islands and GaSb films lattices were relaxed to their bulk value.

The atomic-resolution images of interfaces demonstrated that GaSb films accommodate the misfit strain by formation of interfacial misfit dislocations of Lomer type with glide-type core. The local measurements of strain with the geometric phase analysis (GPA) clearly demonstrated that the presence of an array of interfacial misfit (IMF) dislocations of Lomer type very effectively relaxes the lattice mismatch of the system. However, the GaSb/Si interface is susceptible to a variety of structural defects including threading dislocation, stacking faults, twins, and anti-phase boundaries due to highly lattice mismatch and heterovalent GaSb/Si interface. Therefore, understanding the nature of these defects and their origins is pivotal to suppress their formation.

In this thesis, using atomic-resolution images with the contrast mechanism that strongly depends on atomic-number, the presence of defects was confirmed and their type and origins were studied precisely. The comprehensive study with HAADF-STEM technique combined with investigating the local distribution of strain through GPA has provided further insight into anti-phase boundaries that arise from ambiguous nucleation of GaSb on Si. The atomic-resolution detection of the polarity reversal in GaSb structure enabled the unprecedented direct observation of APBs. This detection ability elucidated the existing

misinterpretation in literature and highlighted the major difference between GaSb/Si and GaAs/Si system in terms of APB-suppressing strategies. The Å-level detection of discordancy in atomic-bonding lengths demonstrated the strain field adjacent to APBs.

In order to suppress the formation of APBs, the GaSb epilayers were grown on a (211)-oriented Si substrate. The epitaxial growth of GaSb on the Si(211) substrate not only fulfilled the initial purpose of suppressing the formation of APBs but also demonstrated the phenomenal lattice-registered GaSb epilayers growth on Si(211) substrates. It was observed that preferential bonding of impinging Ga and Sb atoms at the interface, due to two distinctive bonding sites on the Si(211) surface, enabled the growth that is sublattice-ordered and free of anti-phase boundaries. Heteroepitaxy of GaSb on a Si(211) substrate is dominated by numerous first-order and multiple higher order micro-twins. The atomic-resolved structural study of GaSb films by high-angle annular dark-field scanning transmission electron microscopy reveals that a slight tilt, along with twinning, favors the lattice registry to Si(211) substrates.

Concisely, a wide range of insight can be gained through aberration-corrected HAADF-STEM. This technique combined with quantitative strain studies such as the GPA and chemical investigation like EDXS provide intuitive direct information on defect distribution and propagation as well as growth mechanisms.

8.2 Future Works

As a part of future works, the self-annihilated APBs still require more investigations. The growth parameters such as III/V flux ratio or temperature can be changed to study their effect on the amount of twin formation in GaSb film on

Si(211) substrates. It is anticipated that larger offcut angle for Si(001) substrate would induces more self-annihilated APBs with reduced anti-phase domains. Due to growth mode of GaSb, the evaluation of introducing a low-temperature GaSb buffer layer prior to growth of GaSb film can further enhance our knowledge about the effect of buffer layer on the growth of GaSb epilayer. The behavior of Ga atoms on a Si substrate needs further investigation to gain more in-depth insight about formation of Ga particles. The growth of GaSb and AlSb epilayers on Si can be simulated with molecular dynamic simulation method to understand the agreement between simulation and experiment. AlSb is susceptible to oxidation; therefore in-situ transmission electron microcopy studies will be helpful to investigate the formation and morphology of AlSb islands at the initial stage of growth.

References

[1] K. Tanabe, *A Review of Ultrahigh Efficiency III-V Semiconductor Compound Solar Cells: Multijunction Tandem, Lower Dimensional, Photonic Up/Down Conversion and Plasmonic Nanometallic Structures*, Energies **2**, 504-530 (2009).

[2] G. F. Brown and J. Wu, *Third Generation Photovoltaics*, Laser & Photon. Rev. **3** (4), 394–405 (2009).

[3] III-V compound semiconductor material systems, Accessed 4 Nov. 2012, <http://web.tiscali.it/decartes/phd_html/node4.html>

[4] B. R. Bennett, R. Magno, J. B. Boos, W. Kruppa, M. G. Ancona, *Antimonide-based Compound Semiconductors for Electronic Devices: A Review*, Solid-State Electronics **49**, 1875-1895 (2005).

[5] A. W. Bett and O. V. Sulima, *GaSb Photovoltaic Cells for Applications in TPV Generators*, Semicond. Sci. Technol. **18**, S184–S190 (2003).

[6] Y. H. Kim, Y. K. Noh, M. D. Kim, J. E. Oh, and K. S. Chung, *Transmission Electron Microscopy Study of the Initial Growth Stage of GaSb Grown on Si (001) Substrate by Molecular Beam Epitaxy Method*, Thin Solid Films **518**, 2280–2284 (2010).

[7] A. Beyer, I. Ne´meth, S. Liebich, J. Ohlmann, W. Stolz, and K. Volz, *Influence of Crystal Polarity on Crystal Defects in GaP Grown on Exact Si (001)*, J. Appl. Phys. **109**, 083529 (2011).

[8] S. H. Huang, G. Balakrishnan, A. Khoshakhlagh, L. R. Dawson, and D. L. Huffaker, *Simultaneous Interfacial Misfit Array Formation and Antiphase*

Domain Suppression on Miscut Silicon Substrate, Appl. Phys. Lett. **93**, 071102 (2008).

[9] Z. Liliental-Weber, M. A. O'Keefe, and J. Washburn, *Inversion Boundaries in GaAs Grown on Si*, Ultramicroscopy **30**, 20-26 (1989).

[10] N. D. Browning, E. M. James, K. Kishida, I. Arslan, J. P. Buban, J. A. Zaborac, S. J. Pennycook, Y. Xin, and G. Duscher, *Scanning Transmission Electron Microscopy: An Experimental Tool for Atomic Scale Interface Science*, Rev. Adv. Mat. Sci. **1**, 1-26 (2000).

[11] P. D. Nellist, *Scanning Transmission Electron Microscopy in Science of Microscopy*, edited by P. H. Hawkes and J. C. H. Spence, Springer, New York, (2007), pp. 65–132.

[12] H. Lakner, B. Bollig, S. Ungerechts, and E. Kubalek, *Characterization of III-V Semiconductor Interfaces by Z-Contrast Imaging, EELS and CBED*, J. PHYS. D: APPL. PHYS. **29**, 1767-1778 (1996).

[13] M. J. Hÿtch, J.-L. Putaux, and J.-M. Penisson, *Measurement of the Displacement Field of Dislocations to 0.03Å by Electron Microscopy*, NATURE (LONDON) **423**, 270-273 (2003).

[14] J. Chung and L. Rabenberg, *Measurement of Incomplete Strain Relaxation in a Silicon Heteroepitaxial Film by Geometrical Phase Analysis in the Transmission Electron Microscope*, APPL. PHYS. LETT. **91**, 231902 (2007).

[15] E. Snoeck, B. Warot, H. Ardhuin, A. Rocher, M. J. Casanove, R. Kilaas, and M. J. Hÿtch, *Quantitative Analysis of Strain Field in Thin Films from HRTEM Micrographs*, Thin Solid Films **319**, 157-162 (1998).

[16] M. J. Hÿtch, J. L. Putaux, and J. Thibault, *Stress and Strain Around Grain-Boundary Dislocations Measured by High Resolution Electron Microscopy*, Philos. Mag. **86** (19-31) , 4641-4656 (2006).

[17] F. Houdellier, M. J. Hÿtch, E. Snoeck, and M. J. Casanove, *High-resolution Electron Holography for the Study of Composition and Strain in Thin Film Semiconductors*, Mater. Sci. Eng. B **135**, 188-191 (2006).

[18] A. M. Sanchez, P. L. Galindo, S. Kret, M. Falke, R. Beanland, and P. Goodhew, *Quantitative Strain Mapping Applied to Aberration-corrected HAADF Images*, Microsc. Microanal. **12**, 285-294 (2006).

[19] Y. H. Kim, J. Y. Lee, Y. G. Noh, M. D. Kim, S. M. Cho, Y. J. Kwon, and J. E. *Oh, Effect of Two-Step Growth on the Heteroepitaxial Growth of InSb Thin Film on Si (001) Substrate: A Transmission Electron Microscopy Study*, Appl. Phys. Lett. **89**, 031919 (2006).

[20] Y. H. Kim, J. Y. Lee, Y. G. Noh, M. D. Kim, Y. J. Kwon, and J. E. Oh, *Observation of V-Shaped Defects in the Growth of $In_{0.8}Al_{0.2}Sb$/InSb Layers: Temperature and V/III Flux Ratio Dependences*, J. Cryst. Growth **296**, 75–80 (2006).

[21] I. Vurgaftmana, J. R. Meyer, and L. R. Ram-Mohan, *Band Parameters for III–V Compound Semiconductors and Their Alloys*, J. Appl. Phys. **89** (11), 5815-5875 (2001).

[22] K. Akahane, N. Yamamoto, S. -I. Gozu, A. Ueta, and N. Ohtani, *(In)GaSb/AlGaSb Quantum Wells Grown on Si Substrates*, Thin Solid Films **515**, 4467–4470 (2007).

[23] D. J. Chadi, *Stabilities of Single-Layer and Bilayer Steps on Si(001) Surfaces*, Phys. Rev. Lett. **59** (15), 1691-1694 (1987).

[24] S. F. Fang, K. Adomi, S. Iyer, H. Morkoç, and H. Zabel, *Gallium Arsenide and Other Compound Semiconductors on Silicon*, J. Appl. Phys. **68** (7), R31-R58 (1990).

[25] H. Kroemer, *Polar-on-Nonpolar Epitaxy*, J. Crys. Growth **81**, 193-204 (1987).

[26] C. H. Grein, *First Principle Calculations of Si(211) Surface Reconstruction*, J. Cryst. Growth **180**, 54-60 (1997).

[27] C. Fulk, S. Sivananthan, D. Zavitz, R. Singh, M. Trenary, Y.P. Chen, G. Brill, and N. Dhar, *The Structure of the Si (211) Surface*, J. Electron. Mater. **35** (6), 1449-1454 (2006).

[28] S. Mankefors, *Ab Initio Study of the Ge(211) and Si(211) Bulk Terminated Surfaces*, Surf. Sci. **443**, 99-104 (1999).

[29] D. J. Chadi, *Theoretical Study of the Atomic Structure of Silicon (211), (311), and (331) Surfaces*, Phys. Rev. B **29** (2), 785-792 (1984).

[30] A. A. Baski, S.C. Erwin, and L.J. Whitman, *The Structure of Si(112):Ga-(N×1) Reconstructions*, Surf. Sci. **423**, L265–L270 (1999).

[31] S. M. Prokes, and O. J. Glembocki, *Formation and Characterization of Metal Atom Nanostructures on Si(112) Facet Surfaces*, J. Vac. Sci. Technol. A **17** (4), 1410-1414 (1999).

[32] Z. Gai, R. G. Zhao, W. S. Yang, and T. Sakurai, *Atomic Structure of the Si(112)7×1-In Surface*, Phys. Rev. B **61** (15), 9928-9931 (2000).

[33] E. -S. Cho, J.-W. Park, H. Hur, N.-H. Kim, J.-Y. Baik, C.-H. Jeon, C.-C. Hwang, K.-S. An, and C.-Y. Park, *Structure of the Sb/Si(112) Surface Studied by Low Energy Electron Diffraction*, Jpn. J. Appl. Phys. **43** (4A), 1312-1314 (2004).

[34] C. Fulk, R. Sporken, J. Dumonts, D. Zavitz, M. Trenary, B. Gupta, G. Brill, J. Dinan, and S. Sivananthan, *Arsenic Deposition as a Precursor Layer on Silicon (211) and (311) Surfaces*, J. Electron. Mater. **34** (6), 846-850 (2005).

[35] P. Sen, I. P. Batra, S. Sivananthan, C. H. Grein, N. Dhar, and S. Ciraci, *Electronic Structure of Te- and As-Covered Si(211)*, Phys. Rev. B **68**, 045314 (2003).

[37] F. C. Frank and J. H. van der Merwe, *One-Dimensional Dislocations. I. Static Theory*, Proc. Roy. Soc. (London)A **198**, 205-216 (1949).

[37] F. C. Frank and J. H. van der Merwe, *One Dimensional Dislocations. II. Misfiting Monolayers and Oriented Overgrowth*, Proc. Roy. Soc. (London) A **198**, 216-225 (1949).

[38] J. H. van der Merwe, *Crystal Interfaces. Part I. Semi-Infinite Crystals*, J. Appl. Phys. **34** (1), 117-122 (1963).

[39] Y. H. Lo, M. C. Wu, H. Lee, and S. Wang, *Dislocation Microstructures on Flat and Stepped Si Surfaces: Guidance For Growing High Quality GaAs on (100)Si Substrates*, Appl. Phys. Lett. **52** (17). 1386-1388 (1988).

[40] Y. Wang, P. Ruterana, L. Desplanque, S. El Kazzi, and X. Wallart, *Strain Relief at the GaSb/GaAs Interface Versus Substrate Surface Treatment and AlSb Interlayers Thickness*, J. Appl. Phys. **109**, 023509 (2011).

[41] E. A. Fitzgerald, *Dislications in Strained-layer Epitaxy: Theory, Experiment, and Applications*, Mater. Sci. Rep. **7**, 87-142 (1991).

[42] J. Hornstra, *Dislocations in the Diamond Lattice*, J. Phys. Chem. Solids **5**, 129–141 (1958).

[43] J. P. Hirth and J. Lothe, Theory of Dislocations, Wiley, New York, (1982).

[44] D. B. Holt, and B. G. Yacobi, Extended Defects in Semiconductors: Electronic Properties, Device Effects and Structures, Cambridge University Press (2007).

[45] L. Esaki, R. Tsu, *Superlattice and Negative Differential Conductivity in Semiconductors*, IBM J. Res. Dev. **14** (1), 61-65 (1970).

[46] N. A. Elmasry, J. C. Tarn, and N. H. Karam, *Interactions of Dislocations in GaAs Grown on Si Substrates with InGaAs GaAsP Strained Layered Superlattices*, J. Appl. Phys. **7** (1), 3672-3677 (1988).

[47] J. W. Matthews and A. E. Blakeslee, *Defects in Epitaxial Multilayers I. Misfit Dislocations*, J. Cryst. Grwoth **27**, 118-125 (1974).

[48] P. M. J. Marée, J. C. Barbour, J. F. van der Veen, K. L. Kavanagh, C. W. T. BulleLieuwma, and M. P. A. Viegers, *Generation of Misfit Dissociations in Semiconductors*, J. Appl Phys. **62** (11), 4413-4420 (1987).

[49] C. N. J. Wagner, in *Local Atomic Arrangements Studied by X-Ray Diffraction*, edited by J. B. Cohen and J. E. Hilliard, Gordon and Breach, New York, (1966) pp. 224-225.

[50] F. Ernst and P. Pirouz, *Formation of Planar Defects in the Epitaxial Growth of GaP on Si Substrate by Metal Organic Chemical-Vapor Deposition*, J. Appi. Phys. **64** (9), 4526-4530 (1988).

[51] F. Ernst and P. Pirouz, *The Formation Mechanism of Planar Defects in Compound Semiconductors Grown Epitaxially on {100} Silicon Substrates*, J. Mater. Res. **4** (4), 834-842 (1989).

[52] Z. Ikonić, G.P. Srivastava, and J.C. Inkson, *Electronic Structure of Twinning Superlattices*, Surf. Sci. **304-309**, 880-884 (1994).

[53] D. Cohen, D. L. Medlin, and C. Barry Carter, *Characterization of the Structure and Polarity of Twin Boundaries in GaP*, Mater. Res. Soc. Symp. Proc. **510**, 613-618 (1998).

[54] D. Cohen, S. McKernan, and C. Barry Carter, *Characterization of the Absolute Crystal Polarity across Twin Boundaries in Gallium Phosphide Using Convergent-Beam Electron Diffraction*, Microsc. Microanal. **5**, 173–186 (1999).

[55] J. Hornstra, *Models of Grain Boundaries in the Diamond Lattice: I. Tilt About <110>*, Physica **25**, 409-422 (1959).

[56] N.-H. Cho. B. C. De Cooman, C. B. Carter, R. Fletcher, and D. K. Wagner, *Antiphase Boundaries in GaAs*, Appl. Phys. Lett. **47** (8), 879-881 (1985).

[57] O. Ueda, T. Soga, T. Jimbo, and M. Umeno, *Direct Evidence for Self-annihilation of Antiphase Domains in GaAs/Si Heterostructure*, Appl. Phys. Lett. **55** (5), 445-447 (1989).

[58] D. Cohen and C. B. Carter, *Structure of the (110) Antiphase Boundary in Gallium Phosphide*, J. Microsc. **208** (2), 84–99 (2002).

[59] D. B. Holt, *Antiphase Boundaries in Semiconducting Compounds*, J. Phys. Chem. Solids **30**, 1297-l 308 (1969).

[60] P. M. Petroff, *Nucleation and Growth of GaAs on Ge and the Structure of Antiphase Boundaries*, J. Vac. Sci. Technol. B **4** (4), 874-877 (1986).

[61] D. Vanderbilt and C. Lee, *Energetics of Antiphase Boundaries in GaAs*, Phys. Rev. B **45** (19), 11192-11201 (1992).

[62] O. Rubel, and S. D. Baranovskii, *Formation Energies of Antiphase Boundaries in GaAs and GaP: An ab Initio Study*, Int. J. Mol. Sci. **10**, 5104-5114 (2009).

[63] W. R. Lambrecht, C. Amador, and B. Segall, *Wrong Bond Interations at Inversion Domain Boundaries in GaAs*, Phys. Rev. Lett. **68** (9), 1363-1366 (1992).

[64] S. N. G. Chu, S. Nakahara, S. J. Pearton, T. Boone, and S. M. Vernon, *Antiphase Domains in GaAs Grown by Metalorganic Chemical Vapor Deposition on Siucon-on-Insulator*, J. Appl. Phys **64** (6), 2981-2989 (1988).

[65] I. Ne´meth, B. Kunert, W. Stolza, and K. Volz, *Heteroepitaxy of GaP on Si: Correlation of Morphology, Anti-phase-domain Structure and MOVPE Growth Conditions*, J. Cryst. Growth **310**, 1595–1601 (2008).

[66] K. Volz, A. Beyer, W. Witte, J. Ohlmann, I. Ne´meth, B. Kunert , and W. Stolz, *GaP-Nucleation on Exact Si (0 0 1) Substrates for III/V Device Integration*, J. Cryst. Growth **315**, 37–47 (2011).

[67] S. Koh, T. Kondo, T. Ishiwada, H. Sawada, H. Ichinose, I. Shoji, and R. Ito, *Characterization of Sublattice-reversed GaAs by Refection High Energy Electron Diffraction and Transmission Electron Microscopy*, Physica E **7**, 876-880 (2000).

[68] A. Georgakilas, J. Stoemenos, K. Tsagaraki, P. Komninou, N. Flevaris, P. Panayotatos, and A. Christou, *Generation and Annihilation of Antiphase Domain Boundaries in GaAs on Si Grown by Molecular Beam Epitaxy*, J. Mater. Res. **8** (8), 1908-1921 (1993).

[69] S. I. Molina, G. Aragon, R. Garcia, Y. Gonzalez, L. Gonzalez, and F. Briones, *A Study of the Evolution Process of Antiphase Boundaries in GaAs on Si*, J. Electron. Mater. **22** (5), 567-572 (1993).

[70] H. Kawanami, A. Hatayama, and Y. Hayashi, *Antiphae Boundary of GaAs Films Grown on Si(001) Substrates by Molecular Beam Epitaxy*, J. Electron. Mater. **17** (5) 341-349 (1988).

[71] Y. Li, L. Lazzarini, L.J. Giling, and G. Salviati, *On the sublattice Location of GaAs Grown on Ge*, J. Appl. Phys. **76** (10), 5748-5753 (1994).

[72] Y. Li, G. Salviati, M.M.G. Bongers, L. Lazzarini, and L. Nasi, *On the Formation of Antiphase Domains in the System of GaAs on Ge*, J. Cryst. Growth **163**, 195-202 (1996).

[73] S. M. Ting and E. A. Fitzgerald, *Metal-organic Chemical Vapor Deposition of Single Domain GaAs on Ge/Ge_xSi_{1-x} /Si and Ge substrates*, J. Appl. Phys. **87**, 2618-2628 (2000).

[74] M. Kawabe, T. Ueda, and H. Takasugi, *Initial Stage and Domain of GaAs Grown on Si(100) by Molecular Beam Epitaxy*, Jpn. J. Appl. Phys. **26** (6), L944-L946 (1987).

[75] L. Lazzarini, L. Nasi, G. Salviati, C.Z. Fregonara, Y. Li, L.J. Giling, C. Hardingham, and D.B. Holt, *Antiphase Disorder in GaAs/Ge Heterostructures for Solar Cells*, Micron **31**, 217–222 (2000).

[76] M. K. Hudait, and S. B. Krupanidhi, *Transmission Electron Microscopic Study of GaAs/Ge Heterostructures Grown by Low-pressure Metal Organic Vapor Phase Epitaxy*, J. Appl. Phys. **89** (11), 5972-5079 (2001).

[77] T. Soga, H. Nishikawa, T. Jimbo, and M. Umeno, *Characterization of Antiphase Domain in GaP on Misoriented (001) Si Substrate by Metalorganic Chemical Vapor Deposition*, Jpn. J. Appl. Phys. **32**, 4912-4915 (1993).

[78] H. Kroemer, *Sublattice Allocation and Antiphase Domain Suppression in Polar-on-Nonpolar Nucleation*, J. Vac. Sci. Technol. B **5** (4), 1150-1154 (1987).

[79] B. Kunert, I. Németh , S. Reinhard, K. Volz, and W. Stolz, *Si (001) Surface Preparation for the Antiphase Domain Free Heteroepitaxial Growth of GaP on Si substrate*, Thin Solid Films **517**, 140–143 (2008).

[80] H. Noge, H. Kano, M. Hashimoto, and L Igarashi, *Antiphase Domains in GaAs Grown on a (001)-Oriented Si Substrate by Molecular-beam Epitaxy*, J. Appl. Phys. **64** (4), 2246-2248 (1988).

[81] K. Nauka, G. A. Reid, and Z. Liliental-Weber, *Electron Beam Induced Current and Cathodoluminescence Imaging of the Anti-phase Domain Boundaries in GaAs Grown on Si*, Appl. Phys. Lett. **56** (4), 376-378 (1990).

[82] J. Taftø and J.C. H. Spence, *A Simple Method for the Determination of Structure-Factor Relationships Crystal Polarity Using Electron Diffraction*, J. Appl. Cryst. **15**, 60-64 (1982).

[83] P. Pirouz, C. M. Chorey, and J. A. Powell, *Antiphase Boundaries in Epitaxially Grown β-SiC*, Appl. Phys. Lett. **50** (4), 221-223 (1987).

[84] N. -H. Cho and C. B. Carter, *Formation, Faceting, and Interaction Behaviors of Antiphase Boundaries in GaAs Thin Films*, J. Mater. Sci. **36**, 4209 – 4222 (2001).

[85] T. S. Kuan and C.-A. Chang, *Electron Microscope Studies of a Ge-GaAs Superlattice Grown by Molecular Beam Epitaxy*, J. Appl. Phys. **54** (8), 4408-4413(1983).

[86] D. Cohen and C. B. Carter, *Characterization of APB's in GaP*, Mat. Res. Soc. Symp. Proc. **442**, 503-508 (1996).

[87] J. W. Edington, *Practical Electron Microscopy in Materials Science*, New York Van Nostrand Reinhold Co. (1976).

[88] K. Morizane, *Antiphase Domain Structures in GaP and GaAs Epitaxial Grown on Si and Ge*, J. Cryst. Growth **38**, 249-254 (1977).

[89] D. R. Rasmussen, N. H. Cho, D. W. Susnitzky, and C. B. Carter, *Determination of the Lattice Translation Across Antiphase Boundaries*, Ultramicroscopy **30** (1-2), 27-32 (1989).

[90] D. R. Rasmussen, S. McKernan, and C. B. Carter, *Rigid-body Translation and Bonding across {110} Antiphase Boundaries in GaAs*, Phys. Rev. Lett. **66**, 2629-2632 (1991).

[91] N.-H. Cho, S. McKernan, D.K. Wagner, and C.B. Carter, *Grain Boundaries and Antiphase Boundaries in GaAs*, J. Phys. **C5**, 10(49) 245-250 (1988).

[92] V. Narayanan, S. Mahajan , K.J. Bachmann, V. Woods, and N. Dietz, *Antiphase Boundaries in GaP Layers Grown on (001) Si by Chemical Beam Epitaxy*, Acta Mater. **50**, 1275–1287 (2002).

[93] F. Ernst and P. Pirouz, *The Formation Mechanism of Planar Defects in Compound Semiconductors Grown Epitaxially on {100} Silicon Substrates*, J. Mater. Res. **4** (4), 834-842 (1989).

[94] Z. Liliental-Weber, E.R. Weber, L. Parechanian-Allen, and J. Washburn, *On the use of Convergent-Beam Electron Diffraction for Identification of Antiphase Boundaries in GaAs Grown on Si*, Ultramicroscopy **26**, 59-64 (1988).

[95] R. J. Malik, J. P. van der Ziel, B. F. Levine, C. G. Bethea, and J. Walker, *Molecular Beam Epitaxy of GaSb/AlSb Optical Device Layers on Si(100)*, J. Appl. Phys. **59** (11), 3909-3911 (1986).

[96] C. –A. Chang, H. Takaoka, L. L. Chang, and L. Esaki, *Molecular Beam Epitaxy of AlSb*, Appl. Phys. Lett. **40**, 983-985 (1982).

[97] G. Griffiths, K. Mohammed, S. Subbana, H. Kroemer, and J. L. Merz, *GaSb/AlSb Multiquantum Well Structures: Molecular Beam Epitaxial Growth and Narrow-well Photoluminescence*, Appl. Phys. Lett. **43**, 1059-1061 (1983).

[98] H. Gotoh, K. Sasamoto, S. Kuroda, and M. Kimata, *Molecular Beam Epitaxy of Alsb on GaAs and GaSb on AlSb Films*, Physica Status Solidi (a) **72** (2), 641–645 (1983).

[99] S. H. Huang, G. Balakrishnan, A. Khoshakhlagh, A. Jallipalli, L. R. Dawson, and D. L. Huffaker, *Strain Relief by Periodic Misfit Arrays for Low Defect Density GaSb on GaAs*, App. Phys. Lett. **88**, 131911 (2006).

[100] K. Akahane, N. Yamamoto, S. Gozu, A. Ueta, and N. Ohtani, *Initial Growth Stage of GaSb on Si(001) Substrates with AlSb Initiation Layers*, J. Cryst. Growth **283**, 297–302 (2005).

[101] Y. H. Kim, J. Y. Lee, Y. G. Noh, M. D. Kim, S. M. Cho, Y. J. Kwon, and J. E. Oh, *Growth Mode and Structural Characterization of GaSb on Si (001) Substrate: A Transmission Electron Microscopy Study*, Appl. Phys. Lett. **88**, 241907 (2006).

[102] J. -E. Oh and M. D. Kim, *Molecular Beam Epitaxy of InAs/AlSb HFET's on Si and GaAs Substrates*, J. Semicond. Tech. Sci. **6** (3), 131-135 (2006).

[103] G. Balakrishnan, S. Huang, A. Khoshakhlagh, L. R. Dawson, Y.-C. Xin, P. Conlin, and D. L. Huffaker, *High Quality AlSb Bulk Material on Si Substrates Using a Monolithic Self-assembled Quantum Dot Nucleation Layer*, J. Vac. Sci. Technol. B **23** (3), 1010-1012 (2005).

[104] G. Balakrishnan, A. Jallipalli, P. Rotella, S. Huang, A. Khoshakhlagh, A. Amtout, S. Krishna, L. Ralph Dawson, and D. L. Huffaker, *Room-Temperature Optically Pumped (Al)GaSb Vertical-Cavity Surface-Emitting Laser Monolithically Grown on an Si(100) Substrate*, IEEE J Sel. Top. Quant. **12** (6), 1636-1641 (2006).

[105] J. M. Ripalda, A. M. Sanchez, A. G. Taboada, A. Rivera, B. Ale´n, Y. Gonza´lez, L. Gonza´lez, F. Briones, T. J. Rotter, and G. Balakrishnan,

Relaxation Dynamics and Residual Strain in Metamorphic AlSb on GaAs, Appl. Phys. Lett. **100**, 012103 (2012).

[106] G. Balakrishnan, S.H. Huang, A. Khoshakhlagh, P. Hill, A. Amtout, S. Krishna, G.P. Donati, L.R. Dawson, and D.L. Huffaker, *Room-temperature optically-pumped InGaSb quantum well lasers monolithically grown on Si(100) substrate*, Electron. Lett. **41** (9), (2005).

[107] G. Balakrishnan, S. Huang, L. R. Dawson, Y.-C. Xin, P. Conlin, and D. L. Huffaker, *Growth mechanisms of highly mismatched AlSb on a Si substrate*, Appl. Phys. Lett. **86**, 034105 (2005).

[108] Y. K. Noh, S. R. Park, M. D. Kim, Y. J. Kwon, J. E. Oh, Y. H. Kim, J.Y. Lee, S.G. Kim, K. S. Chung, and T.G. Kim, *Growth Mechanisms and Structural Properties of Self-Assembled AlSb Quantum Dots on a Si(1 0 0) Substrate*, J. Cryst. Growth **301–302**, 244–247 (2007).

[109] Y. K. Noh, M. D. Kim, J. E. Oh, W. C. Yang, and Y. H. Kim, *Growth of Low Defect AlGaSb Films on Si (1 0 0) Using AlSb and InSb Quantum Dots Intermediate Layers*, J. Cryst. Growth **323**, 405–408 (2011).

[110] J. P. van der Ziel, R. J. Malik, J. F. Walker, and R. M. Mikulyak, *Optically Pumped Laser Oscillation in the 1.6–1.8 μm Region from Al0.4Ga0.6Sb/Gasb/Al0.4Ga0.6Sb Double Heterostructures Grown by Molecular Beam Heteroepitaxy on Si*, Appl. Phys. Lett. **48**, 454-456 (1986).

[111] K. Akahane, N. Yamamoto, S. Gozu, and N. Ohtani, *Heteroepitaxial Growth of GaSb on Si(001) Substrates*, J. Cryst. Growth **264**, 21–25 (2004).

[112] K. Akahane, N. Yamamoto, S. Gozu, and N. Ohtani, *High-Quality GaSb/AlGaSb Quantum Well Grown on Si Substrate*, Jpn. J. Appl. Phys. **44** (1), L 15–L 17 (2005).

[113] H. Toyota, S. Fujie, M. Haneta, A. Mikami, T. Endoh, Y. Jinbo, and N. Uchitomi, *Growth and Characterization of GaSb/AlSb Multiple Quantum Well Structures on Si(111) and Si(001) Substrates*, Physics Procedia **3**, 1345–1350 (2010).

[114] M. Mori, K. Murata, N. Fujimoto, C. Tatsuyama, and T. Tambo, *Effect of AlSb Buffer Layer Thickness on Heteroepitaxial Growth of InSb Films on a Si(001) Substrate*, Thin Solid Films **515**, 7861–7865 (2007).

[115] M. Mori, N. Akae, K. Uotani, N. Fujimoto, T. Tambo, and C. Tatsuyama, *Heteroepitaxial Growth of Insb Films on a Si(0 0 1) Substrate via Alsb Buffer Layer*, Appl. Surf. Sci. 216 569–574 (2003).

[116] T. Toda, F. Nishino, A. Kato, T. Kambayashi, Y. Jinbo, and N. Uchitomi, *MBE Growth and Characterization of $GaAs_{1-X}Sb_x$ Epitaxial Layers on Si (0 0 1) Substrates*, Physica B **376–377**, 602–605 (2006).

[117] J. Tatebayashi, A. Jallipalli, M. N. Kutty, S. Huang, K. Nunna, G. Balakrishnan, L. R. Dawson, and D. L. Huffaker, *Monolithically Integrated III-Sb-Based Laser Diodes Grown on Miscut Si Substrates*, IEEE J. Sel. Top. Quant. **15** (3), 716-723 (2009).

[118] Y. K. Noh, Y. J. Hwang, M. D. Kim, Y. J. Kwon, J. E. Oh, Y. H. Kim, and J. Y. Lee, *Strucrural Properties of GaSb Layers Grown on InAs, AlSb, and GaSb Buffer Layers on GaAs (001) Substrates*, J. Korean Phys. Soc. **50** (6), 1929-1932 (2007).

[119] H. S. Kim, Y. K. Noh, M. D. Kim, Y. J. Kwon, J. E. Oh, Y. H. Kim, J.Y. Lee, S. G. Kim, and K. S. Chung, *Dependence of the AlSb Buffers on GaSb/GaAs(0 0 1) Heterostructures*, J. Cryst. Growth **301–302**, 230–234 (2007).

[120] F. M. Mohammedy and M. Jamal Deen, *Growth and Fabrication Issues of Gasb-Based Detectors*, J. Mater. Sci.: Mater. Electron **20**, 1039–1058 (2009).

[121] P.M. Voyles, J.L. Grazul, and D.A. Muller, *IMAGING INDIVIDUAL ATOMS INSIDE CRYSTALS WITH ADF-STEM*, Ultramicroscopy **96**, 251–273 (2003).

[122] H. Neergaard Waltenburg, and J. T. Yates, *Surface Chemistry of* Silicon, Chem. Rev. **95**(5), 1589-1673 (1995).

[123] E. Pehlke and J. Tersoff, *Phase Diagram of Vicinal Si (001)* Surfaces, Phys. Rev. Lett. **67**(10), 1290-1293 (1991).

[124] T. Sakamoto and G. Hashiguchi, *Si (001)-2×1 Single –Domain Structure Obtained by High Temperature Annealing*, J. Appl. Phys. **25**(1), L78-L80 (1986).

[125] E. Schroder-Bergen and W. Ranke, *Steps on Si (001) Vicinal Surfaces Tilted by Various Angles in the [1-10]-, [100]- and [2-10]-zones, Investigated by High Resolution LEED*, Surf. Sci. **259**, 323-338 (1991).

[126] Technoorg Linda, Accessed 12 Nov. 2012 <http://www.technoorg.hu/>.

[127] *Allied High Tech*: Grinding - *MultiPrep*™ System, Accessed 12 Nov. 2012, <http://www.alliedhightech.com/grinding/polishsystem/>.

[128] D. b. Williams and C. B. Carter, *Transmission Electron Microscopy A Textbook for Materials Science* (2nd Edition), Boston, MA: Springer US (2009).

[129] S. J. Pennycook and D. E. Jesson, *High Resolution Incoherent Imaging of Crystal*, Phys. Rev. Lett. 64, 938-942 (1990).

[130] D. E. Jesson and S. J. Pennycook , *Incoherent Imaging of Thin Specimens Using Coherently Scattered Electrons*, Proc. R. Soc. Lond. **A 441**, 261-281 (1993).

[131] D. A. Muller, *Structure and Bonding at the Atomic Scale by Scanning Transmission Electron Microscopy*, Nat. Mater. **8**, 263-270 (2009).

[132] C. R. Hall and P. B. Hirsch, *Effect of Thermal Diffuse Scattering on Propagation of High Energy Electrons Through Crystals*, Proc. R. Soc. Lond. A **286**, 158-177 (1965).

[133] V. Grillo, F.Rossi, *A New Insight on Crystalline Strain and Defect Features by STEM–ADF Imaging*, J. Cryst. Growth **318**, 1151-1156 (2011).

[134] P.J. Phillips, M. DeGraef, L. Kovarik, A. Agrawal, W. Windl, M. J. Mills, *Atomic-Resolution Defect Contrast in Low Angle Annular Dark-Field STEM*, Ultramicroscopy **116**, 47–55 (2012).

[135] R. Ishikawa, E. Okunishi, H. Sawada, Y. Kondo, F. Hosokawa, and E. Abe, *Direct Imaging of Hydrogen-Atom Columns in a Crystal by Annular Bright-Field Electron Microscopy*, Nat. Mater. **10**, 278-281 (2011).

[136] P. E. Batson, *Hydrogen Brightens up*, Nat. Mater. **10**, 270-271 (2011).

[137] S.D. Findlay, N. Shibata, H. Sawada, E. Okunishi, Y. Kondo, Y. Ikuhara, *Dynamics of Annular Bright Field Imaging in Scanning Transmission Electron Microscopy*, Ultramicroscopy **110**, 903–923, (2010).

[138] V. O. Scherzer, *Über Einige Fehler von Elektronenlinsen*, Zeitschrift für Physik **101**, (9-10), 593-603 (1936).

[139] S.J. Pennycook, M. Varela, C.J.D. Hetherington, and A.I. Kirkland, *Materials Advances through Aberration-Corrected Electron Microscopy*, MRS Bulletin **31**, 36-43 (2006).

[140] S. Uhlemann, M. Haider*, Residual Wave Aberrations in the First Spherical Aberration Corrected Transmission Electron Microscope*, Ultramicroscopy **72**, 109-119 (1998).

[141] O. Scherzer, *Sphärische und Chromatische Korrektur von Elektronenlinsen*, Optik **2**, 114–132 (1947).

[142] O. L. Krivanek, P.D. Nellist, N. Dellby, M.F. Murfitt, and Z. Szilagyi, *Towards sub-0.5Å electron beams*, Ultramicroscopy **96**, 229–237 (2003).

[143] M. Haider, P. Hartel, H. Muller, S. Uhelman, and J. Zach, *Current and Future Aberration Correctors for the Improvement of Resolution in Electron Microscopy*, Phil. Trans. R. Soc. A **367**, 3665–3682 (2009).

[144] A. Bleloch and A. Lupini, Imaging at Picoscale, Materials Today **7**(12), 42-48 (2004).

[145] C. Hetherington, *Aberration Correction for TEM*, Materials Today **7**(12), 50-55 (2004).

[146] J. M. Cowley and A. F. Moodie, *The Scattering of Electrons by Atoms and Crystals. I. A New Theoretical Approach*, Acta Crystallographica **10**, 609-619 (1957).

[147] E. J. Kirkland, R. F. Loane, and J.Silox, *Simulation of Annular Dark Field STEM Images Using a Modified Multislcie Method*, Ultramicroscopy 23, 77-96 (1987).

[148] E. J. Kirkland, *Advanced Computing in Electron Microscopy*, Plenum, New York, (1998).

[149] M. J. Hÿtch, E. Snoeck, and R. Kilaas, *Quantitative Measurement of Displacement and Strain Fields from HREM Micrographs*, Ultramicroscopy 74, 131-146 (1998).

[150] P. H. Jouneau, A. Tardot, G. Feuillet, H. Mariette, and J. Cibert, *Strain Mapping of Ultrathin Epitaxial ZnTe and MnTe Layers Embedded in CdTe*, J. Appl. Phys. 75, 7310-7316 (1994).

[151] M. J. Hÿtch, E. Snoeck, and R. Kilaas, *Quantitative Measurement of Displacement and Strain Fields from HREM Micrographs*, Ultramicroscopy 74, 131-146 (1998).

[152] P. H. Jouneau, A. Tardot, G. Feuillet, H. Mariette, and J. Cibert, *Strain Mapping of Ultrathin Epitaxial ZnTe and MnTe Layers Embedded in CdTe*, J. Appl. Phys. 75, 7310-7316 (1994).

[153] K. A. Mkhoyan, P. E. Batson, J. Cha, W. J. Schaff, and J. Silcox, *Direct Determination of Local Lattice Polarity in Crystals*, Science **312**, 1354 (2006).

[154] R. D. Bringans, D. K. Biegelsen, and L. E. Swartz, *Atomic-Step Rearrangement on Si(100) by Interaction with Arsenic and the Implication for GaAS-on-Si Epitaxy*, Phys. Rev. B, **44** (7), 3054-3063 (1991).

[155] S. Y. Woo, S. Hosseini Vajargah, S. Ghanad-Tavakoli, R. N. Kleiman, and G. A. Botton, *Direct Observation of Anti-phase Boundaries in Heteroepitaxy of Gasb thin Films Grown on Si(001) by Transmission Electron Microscopy*, J. Appl. Phys. **112**, 074306 (2012)

[156] G. A. Devenyi, S. Y. Woo, S. Ghanad-Tavakoli, R. A. Hughes, R. N. Kleiman, G. A. Botton, and J. S. Preston, *The Role of Vicinal Silicon Surfaces in the Formation of Epitaxial Twins During the Growth of III-V Thin Films*, J. Appl. Phys. **110**, 124316 (2011).

[157] W. A. Harrison, E. A. Kraut, J. R. Waldrop, and R. W. Grant, *Polar Heterojunction Interfaces*, Phys. Rev. B **18**(8), 4402–4410 (1978).

[158] S. L. Wright, M. Inada, and H. Kroemer, *Polar-on-nonpolar Epitaxy: Sublattice Ordering in the Nucleation and Growth of GaP on Si (211) Surfaces*, J. Vac. Sci Technol. **21**(2), 534–539 (1982).

[159] P. N. Uppal and H. Kroemer, *Molecular Beam Epitaxial Growth GaAs on Si(211)*, J. Appl. Phys. **58**(6), 2195–2203 (1985).

[160] S. L. Wright, H. Kroemer, and M. Inada, *Molecular Beam Epitaxial Growth of GaP on Si*, J. Appl. Phys. **55** (8), 2916–2927 (1984).

[161] H. Kroemer, *Heterostructure Devices: A Device Physicist Looks at Interfaces*, Surf. Sci. **132**, 543–576 (1983).

[162] T. J. de Lyon, D. Rajavel, S. M. Johnson, and C. A. Cockrum, *Molecular-beam Epitaxial Growth of CdTe(112) on Si(112) Substrates*, Appl. Phys. Lett. **66**(16), 2119–2121 (1995).

[163] N. K. Dhar, P. R. Boyd, M. Martinka, J. H. Dinan, L. A. Almeida, and N. Goldsman, *CdZnTe Heteroepitaxy on 3′′(112) Si: Interface, Surface, and Layer Characteristics*, J. Electron. Mater. **29**(6), 748–753 (2000).

[164] G. Brill, Y. Chen, N. K. Dhar, and R. Singh, *Nucleation of ZnTe/CdTe Epitaxy on High-Miller-Index Si Surfaces*, J. Electron. Mater. 32(7), 717–722 (2003).

[165] S. R. Rao, S. S. Shintri, and I. B. Bhat, J. Electron. Mater. 38(8), 1618–1623 (2009).

[166] X. J. Wang, Y. Chang, C. R. Becker, C. H. Grein, S. Sivananthan, and R. Kodma, *Metalorganic Vapor-Phase Epitaxial Growth of (211)B CdTe on (211) Si Using Ge Interfacial Layer*, J. Electron. Mater. **40**(8), 1860–1866 (2011).

[169] D. J. Smith, S.-C. Y. Tsen, D. Chandrasekhar, P. A. Crozier, S. Rujirawat, G. Brill, Y. P. Chen, R. Sporken, and S. Sivananthan, *Growth and Characterization of CdTe:Si Heterostructures — Effect of Substrate Orientation*, Mater. Sci. Eng. B **77**, 93–100 (2000).

[170] S. Y. Woo, G. A. Devenyi, S. Ghanad-Tavakoli, R. N. Kleiman, J. S. Preston, and G. A. Botton, *Tilted Epitaxy on (211)-Oriented Substrates*, (Submitted)

[171] M. V. Belousov, A. Yu. Chernyshov, E. Kozin, H. M. Gibbs, and G. Khitrova, *Interfaces Correlation Effect in 2D GaAs/AlAs Heterostructures*, 6th Int. Symp. "Nanostructures: Physics and Technology" St Petersburg, Russia, June 22-26 (1998).

[172] D. W. Pashley, *Epitaxy Growth Mechanism*, Mater. Sci. Tech. **15**, 1-7 (1999).

[173] X. Zhang, A. E. Staton-Bevan, D. W. Pashley, S. D. Parker, R. Droopad, R. L. Williams, and R. C. Newman, *A Transmission Electron Microscopy and Reflection High-Energy Electron Diffraction Study of the Initial Stages of the Heteroepitaxial Growth of InSb on GaAs (001) by Molecular Beam Epitaxy*, J. Appl. Phys. **67**, 800-806 (1990).